Final Report

for the Period

1 July 1994 - 30 June 2000

AASERT Award
for Research entitled

Coulomb Coupling Between Quantum Dots and Waveguides

Wolfgang Porod, Craig S. Lent, and Gary H. Bernstein

Department of Electrical Engineering
University of Notre Dame
Notre Dame, IN 46556

Submitted
to the

Office of Naval Research

800 North Quincy Street
Arlington, VA 22217

Grant No: N00014-94-1-0821
R&T Project: 3145035 --- 01

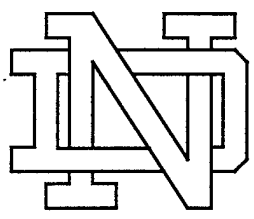

Nano
Devices
Group

UNIVERSITY OF
NOTRE DAME

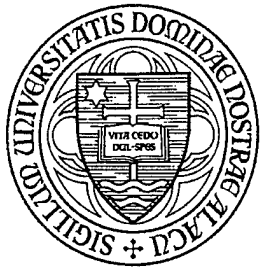

Final Report

for the Period

1 July 1994 - 30 June 2000

AASERT Award
for Research entitled

Coulomb Coupling Between Quantum Dots and Waveguides

Wolfgang Porod, Craig S. Lent, and Gary H. Bernstein

Department of Electrical Engineering
University of Notre Dame
Notre Dame, IN 46556

Submitted
to the

Office of Naval Research

800 North Quincy Street
Arlington, VA 22217

Grant No: N00014-94-1-0821
R&T Project: 3145035 --- 01

Research Summary

This AASERT award augmented and provided additional support for the parent grant entitled "Quantum Cellular Automata" (QCA), ONR grant no. N00014-93-1-1084. Initially, the main focus of this research was the study of Coulombic coupling effects in semiconductor nanostructures for applications in quantum cellular automata. We considered both III-V and Si-based semiconductor systems. In later years, the AASERT award supported work on QCA realizations in Coulomb-blockade metal-dot systems, which were successful in demonstrating the basic QCA switching operation. This latter work has contributed in large measure to the visibility and success of the QCA concept. Recently, AASERT-supported students have explored the applicability of QCA systems for quantum computing.

Due to the group nature of our research effort at Notre Dame, the continuity of the proposed student research training was assured well beyond the expiration date of the parent award in '96. In fact, this AASERT grant has seen several no-cost extensions since grant support, scholarships, and fellowships were also available for the AASERT-sponsored domestic students, which allowed us to provide research training for a large number of students over quite a few years.

AASERT-sponsored Graduate Students

- Douglas Tougaw
- Henry Harbury
- Brad Campbell
- Greg Bazan
- Minhan Chen
- John Timmler
- Islamshah Amlani
- Christopher Harris
- Alan Hall

Organization of the Report

Research Description

• **Modelling of quantum dots in the few-electron regime.** The purpose of our numerical modelling was to support the experimental effort by providing the design parameters for the experimental realization of semiconductor QCA quantum-dot cells. to this end, we have studied field-confined quantum dots in the few electron regime. We have explored the feasibility of several top-gate configurations and we have studied their capability of producing crisp confining potentials. The usual mode is to employ top gates with a negative bias, which repel the carriers in the two-dimensional electron gas underneath. Quantum wires and quantum dots are realized in the areas below metal-free regions on the surface, which expose the semiconductor to the ambient dielectric. Our modelling shows that for typical dimensions and structural parameters, it will be very difficult to use negative gate biases to tune quantum dots which are occupied by a small number of electrons. Even for extremely small separations of the 2DEG from the surface, say 40 nm or so, the confining electrostatic potential is still quite gradual. It will also be very difficult to realize top metal gates with openings which are on the order of only a few tens of nanometers. In addition, the geometrical features of the metal opening are several times larger than the induced dot underneath. This makes it very hard, if not impossible, to fabricate a QCA cell, which contains several closely-spaced dots, by utilizing negative top-gate biasing. An alternate approach is to use positive top-gate biasing. In this scheme, one starts out with a structure which does not possess a two-dimensional electron gas without biasing. A positive bias applied to the metal on the top surface may then induce electrons underneath. Our modelling of this accumulation mode shows that geometrical considerations allow the realization of closely-spaced dots. The most promising approach which we have been able to identify based on our modelling work is a combined depletion mode (negative top-gate bias) and accumulation mode (positive top-gate bias). We envision a top-gate geometry which consists of a rather large opening (negative bias) in which several metal dots (positive bias) are placed. The negative gate just barely depletes the 2DEG, and the carriers may be brought back with a rather small positive bias. Our modeling shows that QCA cell may be realized by this combined biasing approach. We have investigated both the III-V and the Si-SiO_2 material systems. Our modeling indicates that the silicon system is, in principle, particularly well suited for the realization of gate-confined quantum dots due to the extremely thin oxide layer, which yields very crisp confining potentials.

• **QCA realization in III-V materials**. We performed measurements on an AlGaAs/GaAs double quantum dot structure, where dots were separated by an opaque barrier and each dot conductance was measured independently and simultaneously. We measured the Coulomb blockade oscillations (CBOs) for each dot when the structure was configured for one and two dots. When configured as a single-dot device, we swept the backgate and observed different CBO periods for each dot measured independently, implying dots of different sizes. When the device was configured for two dots, we observed strongly modulated CBOs in the larger dot while CBOs in the smaller dot exhibit almost no influence due to the changing charge of the larger dot. From this experiment, we had realized a charge detection scheme where we observed strong coupling in the detector signal in addition to the detector exhibiting minimal effect on the dot being measured. For an implementation of quantum-dot cellular automata (QCA), (1) cells must couple capacitively and (2) one must be able to detect electron occupation of a quantum dot within a cell. With this investigation, we demonstrated these two key components required for QCA in AlGaAs/GaAs materials.

- **Novel technique for nanostructure fabrication in silicon.** We have also investigated a novel method for fabricating nanostructures based on the interaction of an electron beam with the metal-oxide-semiconductor material system. The electron beam produced a stable charge near the oxide-silicon interface which modulated the surface potential creating a quasi-one-dimensional potential valley. Electrical transport measurements conducted on the post-irradiated MOSFETs revealed structure in the conductance which was not present in an unexposed device, indicating that Q1D structures can be created directly in the gate of a Si MOSFET. We have not continued to pursue this technology, although nothing has indicated that it will not work for our applications.

- **Study of Coulomb coupling for QCA realizations in metallic systems.** We investigated of the application of metallic tunnel structures for the realization of QCA cells. Our initial work was aimed at an experimental investigation of the Coulomb interaction between normal metal (Au/Ti) and superconducting (AlO_x) 2D-films separated by an insulating (Al_2O_3) layer. We reported the first observation of supercurrent drag by injecting a drive current into a normal metal film and measuring the open circuit voltage due to drag in a superconducting film. The drag was observed at temperatures close to Tc, with the ratio of the drag current to the drive current as high as about $1x10^{-3}$. Our results were discussed in terms of a model of Coulomb mutual scattering between the normal electrons in the drive wire and the superelectrons in the drag wire. The significance of this work to QCA's lies in the fact that it required the fabrication of high-quality Al_2O_3 films grown in situ on Al wires. This technology was later refined to the point of insertion in high quality tunnel junctions used in numerous subsequent studies of QCA's in metallic dots.

- **Fabrication and characterization of Coulomb-blockade metal-dot structures.** The experimental work is based on aluminum islands and aluminum tunnel junctions, fabricated on an oxidized silicon wafer. The fabrication uses standard electron-beam lithography and dual shadow evaporation to form the metallic islands and tunnel junctions. The area of the tunnel junctions is an important quantity since this dominates island capacitance, which determines the charging energy of the island, and thus the operating temperature of the device. For our devices, the typical dimensions are 60 by 60 nm, giving a junction capacitance of 400 aF. The QCA device is mounted on the cold finger of a dilution refrigerator that has a base temperature of 10 mK. We measure the conductance through various parts of the circuit using standard ac lock-in techniques. A magnetic field of 1T is applied to suppress the superconductivity of the aluminum metal.

- **Demonstration of QCA behavior in Coulomb-blockade metal-dot structures.** Using the above technique for the fabrication and testing of Coulomb-coupled metal-dot QCA structures, we have investigated QCA-type behavior in a series of papers. In our initial studies, we demonstrated the basic QCA switching behavior, i.e. the controlled tunneling of one single electron which is induced by the switching of another close-by electron. We have also demonstrated the switching of a QCA line, which showed that the whole line switched and that the signal did not decay (as some critics had argued). In other studies, we demonstrated the functioning of a QCA majority gate, which provides the basic building block for QCA logic operation. With these studies, we have experimentally demonstrated the basic features of the QCA paradigm, albeit at cryogenic temperatures. In future work, we will investigate ways to realize QCA behavior at higher temperatures, with the main goal of room temperature QCA operation.

Publications

Minhan Chen, Wolfgang Porod, and David J. Kirkner, "A Coupled Finite Element/Boundary Element Method for Semiconductor Quantum Devices with Exposed Surfaces," *Journal of Applied Physics* **75**, 2545-2554 (1994).

Craig S. Lent and P. Douglas Tougaw, "Bistable saturation due to single electron charging in rings of tunnel junctions," *Journal of Applied Physics* **75**, 4077-4080 (1994).

P. Douglas Tougaw and Craig S. Lent, "Logical devices implemented using quantum cellular automata," *Journal of Applied Physics* 75, 1818-1825 (1994).

Minhan Chen and Wolfgang Porod, "Numerical Simulation of the Effect of Surface Charges on Electron Confinement in Quantum Dot Structures," *Proceedings of the Third International Workshop on Computational Electronics*, S. M. Goodnick, ed., pp. 215 - 218 (1994).

P. Douglas Tougaw and Craig S. Lent, "Dynamic Behavior of Coupled Quantum Dot Cells," *Proceedings of the Third International Workshop on Computational Electronics*, S. M. Goodnick, ed., pp. 227 - 230 (1994).

Craig S. Lent, P. Douglas Tougaw, and Wolfgang Porod, "Quantum Cellular Automata: Computing with Arrays of Quantum Dot Molecules," *Proceedings of the Workshop on Physics and Computation - PhysComp `94*, IEEE Computer Society Press, pp. 5 - 13 (1994).

Minhan Chen and Wolfgang Porod, "Design of Gate-Confined Quantum Dot Structures in the Few-Electron Regime," *Journal of Applied Physics* **78**, 1050 - 1057 (1995).

X. Huang, G. Bazán, G. H. Bernstein, "Observation of Supercurrent Drag Between Normal Metals and Superconducting Films," *Physical Review Letters* **74**(20), 4051-4054 (1995).

B. E. Campbell, X. Huang, and G. H. Bernstein, "A Novel Method for Producing Nanostructures in Silicon Inversion Layers," *Journal of Vacuum Science and Technology B* **13**(3), 1135-1138 (1995).

P. Douglas Tougaw and Craig S. Lent, "Effect of Stray Charge on Quantum Cellular Automata," *Japanese Journal of Applied Physics* **34**, 4373 - 4375 (1995).

Wolfgang Porod, "Modeling Quantum-Dot Cellular Automata Devices and Architectures," Proceedings of the *23rd International Conference on the Physics of Semiconductors*, ed. by M. Scheffler and R. Zimmermann, pp. 3251 - 3258 (World Scientific, 1996).

G. H. Bernstein, G. Bazán, M. Chen, C. S. Lent, J. L. Merz, A. O. Orlov, W. Porod, G. L. Snider, and P. D. Tougaw, "Practical Issues in the Realization of Quantum-Dot Cellular Automata," to appear in *Superlattices and Microstructures* **20**(4), (1996).

G. Bazan, A. O. Orlov, G. L. Snider, and G. H. Bernstein, "Charge Detector Realization for AlGaAs/GaAs Quantum-dot Cellular Automata," *Journal of Vacuum Science and Technology B*. 14(6), pp. 4046-4050 (1996).

A. O. Orlov, I. Amlani, G. H. Bernstein, C. S. Lent, and G. L. Snider, "Realization of a Functional Cell for Quantum-dot Cellular Automata," Science, 277, pp. 928-930 (1997).

I. Amlani, A. O. Orlov, G. L. Snider, C. S. Lent, and G. H. Bernstein, "External Charge State Detection of a Double-dot System," Appl. Phys. Lett., 71(12), pp. 1730-1732 (1997).

I. Amlani, A. O. Orlov, G. L. Snider, and G. H. Bernstein, "Differential Charge Detection for Quantum-dot Cellular Automata," J. Vac. Sci. Technol. B, 15(6), pp. 2832- 2835 (1997).

Minhan Chen and Wolfgang Porod, "Simulation of Quantum-Dot Structures in Si/SiO_2," *VLSI Design* **6**, 335-339 (1998).

I. Amlani, A. O. Orlov, G. L. Snider, C. S. Lent, and G. H. Bernstein, "Demonstration of Six-dot Quantum Cellular Automata System," Appl. Phys. Lett., 72(17), pp. 2179-2181 (1998).

G. L. Snider, A. O. Orlov, I. Amlani, G. H. Bernstein, C. S. Lent, J. L. Merz, and W. Porod, "A Functional Cell for Quantum-dot Cellular Automata," Solid State Electronics, 42(7-8), pp. 1355-1359 (1998).

A. O. Orlov, I. Amlani, G. Toth, C. S. Lent, and G. L. Snider, "Correlated Electron Transport in Coupled Metal Double Dots," Appl. Phys. Lett., 73(19), pp. 2787-2790 (1998).

Per Hyldgaard, Henry K. Harbury, and Wolfgang Porod, "Electrostatic Formation of Coupled Si/SiO_2 Quantum Dot Systems," *VLSI Design* **8**, 555 -558 (1998).

I. Amlani, A. O. Orlov, G. L. Snider, C. S. Lent, and G. H. Bernstein, "Demonstration of a Functional Quantum-dot Cellular Automata Cell," J. Vac. Sci. Technol. B, 16(6), pp. 3795-3799 (1998).

G. L. Snider, A. O. Orlov, I. Amlani, G. H. Bernstein, C. S. Lent, J. L. Merz, and W. Porod, "Experimental Demonstration of Quantum-dot Cellular Automata," Semiconductor Science and Technology, 13, pp. A130-A134 (1998).

W. Porod, C. S. Lent, G. H. Bernstein, A. O. Orlov, I. Amlani, G. L. Snider, and J. L. Merz, "Quantum-Dot Cellular Automata: Computing with Coupled Quantum Dots," Intl. J. of Electr., 86(5), pp. 549-590 (1999).

A. Orlov, I. Amlani, G. Toth, C. S. Lent, G. H. Bernstein, and G. L. Snider, "Experimental Demonstration of Binary Wire for Quantum-dot Cellular Automata," Appl. Phys. Lett., 74(19), pp. 2875-2877 (1999).

I. Amlani, A. O. Orlov, G. L. Snider, C. S. Lent, and G. H. Bernstein, "Experimental Observation of Electron Switching in a Quantum-dot Cellular Automata Cell," Superlatt. and Microstruct., 25(5), pp. 273-278 (1999).

G. L. Snider, A. O. Orlov, I. Amlani, X. Zuo, G. H. Bernstein, C. S. Lent, J. L. Merz, and W. Porod, "Quantum-dot Cellular Automata: Review and Recent Experiments," J. Appl. Phys., 85(8), pp. 4283-4285 (1999).

G. Toth, A. O. Orlov, I. Amlani, C. S. Lent, G. H. Bernstein, and G. L. Snider, "Conductance Suppression due to Correlated Electron Transport in Coupled Double-dots," Phys. Rev B, 60(24), pp. 16906-16912 (1999).

G. H. Bernstein, I. Amlani, A. O. Orlov, C. S. Lent and G. L. Snider, "Observation of Switching in a Quantum-dot Cellular Automata Cell," Nanotechnology, 10(1999), pp. 166-173 (1999).

I. Amlani, A. Orlov, G. Toth, G. H. Bernstein, C. S. Lent, G. L. Snider, "Digital Logic Gate Using Quantum-Dot Cellular Automata," Science, 284, pp. 289-291 (1999).

G. L. Snider, A. O. Orlov, I. Amlani, G. H. Bernstein, C. S. Lent, J. L. Merz, and W. Porod, "Quantum-Dot Cellular Automata: Line and Majority Logic Gate," Jap. J. Appl. Phys., 38, pp.

7227-7229 (1999).

A. O. Orlov, I. Amlani, R. K. Kummamuru, R. Ramasubramaniam, G. Toth, C. S. Lent, G. H. Bernstein, and G. L. Snider, "Experimental Demonstration of Clocked Single- Electron Switching in Quantum-dot Cellular Automata," Appl. Phys. Lett., 77(2), pp. 295-297 (2000).

I. Amlani, A. O. Orlov, R. K. Kummamuru, G. H. Bernstein, C. S. Lent, and G. L. Snider, "Experimental Demonstration of a Leadless Quantum-dot Cellular Automata Cell," Appl. Phys. Lett., 77(5), pp. 738-740 (2000).

APPENDIX: Selected Reprints

Contents:

Observation of Supercurrent Drag between Normal Metal and Superconducting Films

Xiaokang Huang, Greg Bazàn, and Gary H. Bernstein*
Department of Electrical Engineering, University of Notre Dame, Notre Dame, Indiana 46556
(Received 1 September 1994)

We experimentally investigate the Coulomb interaction between normal metal (Au/Ti) and superconducting (AlO_x) 2D films separated by an insulating (Al_2O_3) layer. We report here the observation of supercurrent drag predicted by Duan and Yip [Phys. Rev. Lett. **70**, 3647 (1993)]. The drag was observed at temperatures close to T_c, with the ratio of the drag current to the drive current as high as about 1×10^{-3}. Our results are discussed in terms of a model of Coulomb mutual scattering between the normal electrons in the drive wire and the superelectrons in the drag wire.

PACS numbers: 73.20.Dx, 73.50.–h, 73.61.–r, 74.90.+n

Coulomb mutual scattering (CMS) between two proximate electron gases was first discussed theoretically by Price [1]. It was predicted that electrons in the two closely separated electron gases could exchange their momentum and energy via their Coulomb interaction, resulting in current drag. Coulomb drag was later experimentally observed between a two-dimensional electron gas (2DEG) and a three-dimensional electron gas (3DEG) [2], and also between two 2DEG's [3,4]. The samples in those experiments were GaAs/AlGaAs heterostructures. Although the CMS model can be used to qualitatively explain their results, some subtle effects, such as Peltier heating [2,4,5] and virtual phonon exchange [3,6], were also involved as secondary coupling mechanisms. Current drag in a magnetic field [7] and from the van der Waals interaction [8] was also investigated theoretically. CMS has not been experimentally observed in normal metal systems because of screening and dissipation.

Recently, Duan and Yip [9] theoretically studied the Coulomb interaction between two spatially separated superconducting systems that can be either two-dimensional (2D) films or one-dimensional (1D) lines. They concluded that a relatively strong supercurrent drag could result from the Coulomb interaction, with an estimated current drag-to-drive ratio between two 1D loops separated by 100 nm as high as 10^{-3}. This could also be true with normal metal as the input and the superconductor as the sensor [9]. The first experimental study on current coupling in a superconductor–normal metal system was recently reported by Giordano and Monnier [10]. However, the weak coupling and the similarity of their results to the behavior of vortices in high-T_c superconductors [11] led them to consider a mechanism of coupling other than supercurrent drag.

In this Letter, we report experimental results of the observation of supercurrent drag between a normal metal (Au/Ti) film and a superconducting (AlO_x) film separated by an insulator. Although a structure similar to that of Ref. [10] was used in our experiments, our samples were more than a hundred times smaller. Very strong current coupling ($\sim 10^{-3}$) was observed when the drive current was injected into the normal metal film and the open circuit voltage was detected at the superconducting side. There was no detectable coupling measured at the normal metal wire when the drive current was injected into the superconducting wire. The current coupling ratio as a function of temperature was fitted by a model of Coulomb mutual scattering between the electrons in the drive (normal metal) wire and the superelectrons in the drag (superconducting) wire.

A schematic diagram of the trilayer samples used in our current drag experiments is shown in Fig. 1. The bottom layer is 12/3 nm thick Au/Ti. Ti was used for adhesion between the Au layer and the SiO_2/Si substrate. The top layer is 30 nm thick AlO_x formed by bleeding O_2 with a pressure of 5×10^{-6} torr [12] into the vacuum chamber during Al evaporation. We chose AlO_x over pure Al in order to achieve a wide transition temperature region. This helped us to more accurately investigate the change of the current drag over the transition from the normal state to the superconducting state. The sheet resistance of the Au/Ti film was 8 Ω at room temperature. The sheet resistance of the AlO_x film ranged from 10 Ω to 2 kΩ at room temperature, depending on the percentage of O_2 in the Al film. An Al_2O_3 insulating layer, deposited by the same method as the AlO_x layer except with higher O_2 pressure (5×10^{-4} torr), was formed between the Au/Ti and the AlO_x. The relative dielectric constant of the Al_2O_3 was 4.5–6 as obtained by capacitance measurement, the breakdown voltage was 10^7 V/cm, and the thickness was 35 nm, as measured with a sur-

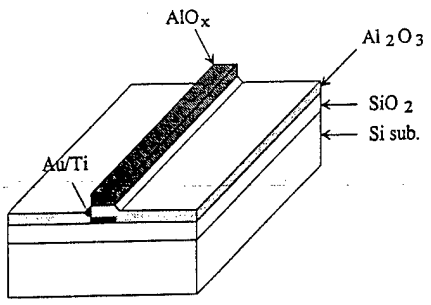

FIG. 1. Schematic of our device structure. The thickness of the Al_2O_3 separation was 35 nm and the overlapping area of the AlO_x and Au/Ti was 1×50 μm^2.

0031-9007/95/74(20)/4051(4)$06.00

face profiler. The thickness of our insulating layer prevented tunneling between the two conductive layers, resulting in a total leakage resistance between the two layers of $10^9-10^{12}\ \Omega$. Both the Au/Ti and AlO_x layers were 1 μm wide. Electron beam lithography was used to pattern the Au/Ti and the AlO_x in order to make the two layers totally overlap. The alignment error was $< \pm 0.05\ \mu$m [13] over an active area of $1 \times 50\ \mu m^2$. A 15 Hz ac current signal was sent into the primary (drive) side. The coupling signal at the secondary (drag) side was detected with a lock-in amplifier as an open circuit voltage.

It would be preferable to measure the short circuit drag current instead of the open circuit voltage from the secondary side. It is difficult to measure the current directly with a lock-in amplifier because the resistance of metal lines is very small at lower temperatures, and changes continuously over the transition region, becoming so small that it cannot drive the ammeter. This is because the low metal resistance, i.e., the source resistance of the drag wire as current source, short circuits the drag current from the ammeter. Therefore, we determined the supercurrent drag by measuring the open circuit voltage at the secondary side with a high impedance lock-in amplifier. As shown in Fig. 2(a), an input current I_1 is injected into the primary side. The electrons in the primary wire transfer their momentum to the electrons in the secondary wire via CMS [1], resulting in a drag current I_{drag} flowing in the same direction as I_1 and causing an accumulation of electrons at one end of the secondary wire, inducing an open circuit voltage V_{oc} at the secondary side. This induced voltage causes electrons to drift in the opposite direction within the wire, canceling the effects of drag ad resulting in net zero current. As shown in Fig. 2(a), the polarity of V_{oc} is opposite to that induced in the input loop by the input current I_1.

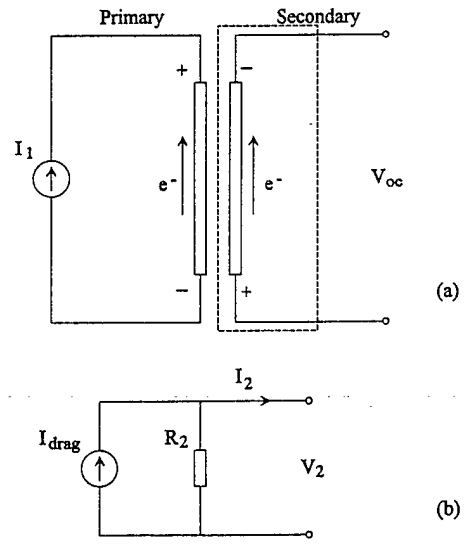

FIG. 2. (a) Circuit schematic of our test circuit. I_1 is the input current and V_{oc} is the measured open circuit voltage. (b) The equivalent circuit of the secondary wire. R_2 is the temperature dependent resistance of the secondary wire.

The equivalent circuit [14] of the secondary wire is shown in Fig. 2(b). The induced current I_{drag} is symbolized as a current source. R_2 is the resistance of the secondary wire. For short circuit conditions, $V_2 = 0$, which gives $I_2 = I_{sc} = I_{drag}$, while with the output loop open circuited, I_2 is zero. For open circuit conditions,

$$V_2 = V_{oc} = I_{drag}R_2 \quad \text{or} \quad I_{drag} = V_{oc}/R_2 . \qquad (1)$$

This simple relationship is very important since it shows that V_{oc} can give us a measure of I_{drag} provided that R_2 is known.

The resistance of the AlO_x film (sample 2a.1), R_2, was measured using a standard four-probe measurement with 5 nA input current. The change of the resistance as a function of temperature, ranging from 1.87 to 2.3 K, is shown in Fig. 3(a). It shows that the transition between the normal state and the superconducting state occurred in the temperature range from 1.93 to 2.05 K.

Figure 3(b) shows V_{oc} and V_{oc}/I_1 as a function of temperature. V_{oc} was measured at the AlO_x side when introducing the input current I_1 at the Au/Ti side. Several samples with the same size, but with different transition tem-

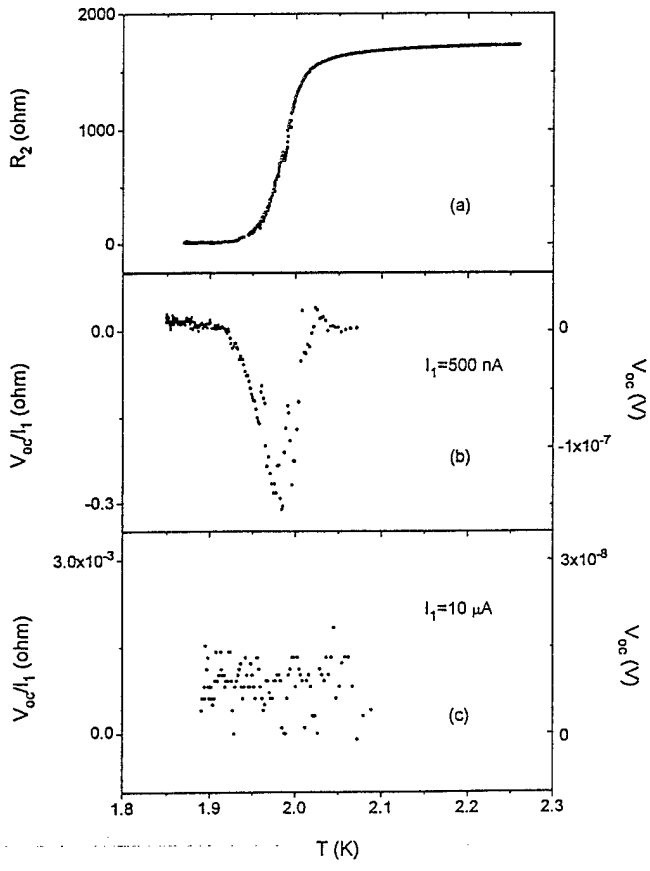

FIG. 3. (a) Temperature dependence of the resistance of the AlO_x. The transition temperature region was 1.93 to 2.05 K. (b) The ratio of the open circuit voltage, V_{oc}, to the input current I_1 as a function of temperature for I_1 injected into the Au/Ti wire and V_{oc} detected at the AlO_x. For convenience, data are also plotted as V_{oc}. (c) V_{oc}/I_1 as a function of temperature with I_1 injected into the AlO_x and V_{oc} measured at the Au/Ti.

peratures, were measured and the results were repeatable. Similar effects were also observed with a sample that consisted of 10 μm wide AlO_x and 20 μm wide Au/Ti layers separated by a 35 nm thick Al_2O_3 layer, although the coupling signal was more than 100 times weaker in this case.

As discussed above, V_{oc} (V_{oc}/I_1) is a function of both R_2 and I_{drag}, which are both temperature dependent. Comparing Figs. 3(a) and 3(b), we can see that when the temperature T is higher than the critical temperature of the AlO_x, there is no induced voltage detected. Since $V_{oc} = I_{drag}R_2$ and $R_2 \neq 0$, zero open circuit voltage means that there is no coupling current at this temperature range. The absence of coupling is due to the fact that the AlO_x is still in the normal state within this high-temperature region where the screening effect is strong and the normal electrons are dissipative. This also confirms that there is no detectable current coupling between two normal metal films for a barrier of 35 nm.

When the AlO_x starts to became superconducting at T below ~2.0 K, some electrons form Cooper pairs and some are still in the normal state. Since Cooper pairs move freely without dissipation and interact within a coherence length that is much larger than the screening length in the normal state, a supercurrent I_{drag} results from the Coulomb interaction between the normal electrons in the drive line and the superelectrons in the drag line. Therefore, an open circuit voltage across the AlO_x line appears because $I_{drag} \neq 0$ and $R_2 \neq 0$ on this region. The magnitude of the induced voltage increases as temperature decreases and more electrons pair. This means that with decreasing temperature, although the resistance of the AlO_x decreases, the increase in the coupling current from the Coulomb interaction is much faster than is the decrease of the resistance.

The negative sign of V_{oc} means that its polarity is in the opposite direction relative to I_1, as discussed above. This indicates that the coupling current is in the same direction as I_1, which was expected [2–5,9] for a Coulomb interaction with momentum transfer between the electrons in the Au/Ti and Cooper pairs in the AlO_x. As the temperature decreases, the magnitude of V_{oc} reaches a maximum value when the increase of I_{drag} balances the decrease of R_2. After this, the magnitude of V_{oc} starts to drop toward zero with the temperature far below T_c because R_2 approaches zero in Eq. (1). The negative sign of V_{oc} also tells us that the induced voltage was not from leakage or tunneling, since in both cases the voltage in the drag line would be in the same direction as that in the drive line. As a further check, we measured the leakage current with 0.5 V bias applied between the two films and found the leakage resistance to be greater than 10^9 Ω with very little variation over the temperature range of interest. V_{oc} could be due to neither classical capacitive nor inductive coupling since either coupling would correspond to a nonzero voltage $\pm 90°$ out of phase relative to the input signal. We therefore measured the quadrature component simultaneously and found it to be much smaller than the in-phase component, with almost no variation over the temperature range and for frequencies from 15 to 1500 Hz.

The open circuit voltage was also measured at the Au/Ti film when AlO_x wire was used as the input. V_{oc}/I_1 for this case is shown in Fig. 3(c). It is important to note that the vertical scale of Fig. 3(c) is 10^2 times smaller than that of Fig. 3(b). From this figure, it is clear that no current coupling could be detected. Therefore, the current coupling from the superconducting wire to the normal metal wire was at least 10^3 times smaller than that of the reverse case. This asymmetric behavior of the current coupling provides more evidence that the detected current coupling was neither from electromagnetic coupling nor from quantum tunneling between the two films. Our data are in good agreement with supercurrent drag theory [9], as will be discussed further below. Since there was no coupling when the normal metal acted as the secondary wire, the current coupling and the coupling ratio mentioned below refer only to the case in which the Al/Ti is the primary wire and the AlO_x is the secondary wire.

The equivalent resistance V_{oc}/I_1, as a function of the input current I_1, was also investigated. As I_1 changed from 0.5 to 10 μA, the peak magnitude of V_{oc}/I_1 only fluctuated within $\pm 10\%$ of the peak value. However, the peak position moved toward lower temperatures with $I_1 > 2.5$ μA. This is possibly due to self-heating of the sample for large input current.

The temperature dependence discussed above is qualitatively similar to that reported in Ref. [10], but with much greater measured output voltages. The differences in sign and magnitude between our results and those of Ref. [10] imply that different mechanisms are involved in the two current coupling processes. CMS was ruled out in Ref. [10], whereas below we justify our interpretation in terms of CMS.

From Eq. (1), I_{drag} was calculated from V_{oc} and R_2 measurements, and is shown in Fig. 4(a) as the current coupling ratio I_{drag}/I_1. As expected, there was no current coupling when the AlO_x was in the normal state. At temperatures below T_c, I_{drag}/I_1 increased rapidly to values as high as about 1×10^{-3}. It is not surprising that the error of I_{drag}/I_1 increased as temperature decreased, since $I_{drag} = V_{oc}/R_2$. The absolute error of the drag current, δI_{drag}, can be written as

$$\delta I_{drag} = \pm\sqrt{(\delta V_{oc}/R_2)^2 + (V_{oc}\delta R_2/R_2^2)^2}, \qquad (2)$$

where δV_{oc} and δR_2 are the absolute errors of V_{oc} and R_2, respectively. Thus, when R_2 approaches zero, δI_{drag} approaches infinity. Therefore, V_{oc}/R_2 was used for calculating I_{drag} in Fig. 4(a) only when R_2 and V_{oc} were not too small, i.e., for temperatures close to T_c.

With reference to the Drude transport model, the drag current in the secondary wire can be considered part of the current flowing in the first wire but with a different scattering time, so the relationship between the coupling current and the mutual scattering rate can be expressed as

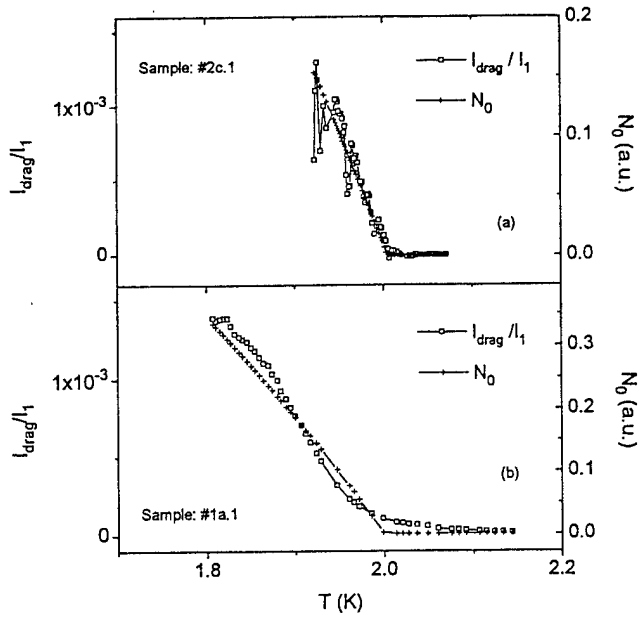

FIG. 4. The relationship between the current coupling ratio, $I_{drag}/I_1 = V_{oc}/R_2I_1$, and temperature for sample 2c.1 (a) and 1a.1 (b). The normalized Cooper pair density as a function of temperature is also shown in the figures for comparison with the supercurrent drag theory.

$$I_{drag} = (\tau_1/\tau_{12})I_1\,, \tag{3}$$

where τ_1 is the electron scattering time in the drive wire, and τ_{12} is the mutual scattering time between the two wires. The scattering rate $1/\tau_{12}$ is proportional to N_1N_2 [1], that is,

$$1/\tau_{12} = K_{12}N_1N_2\,, \tag{4}$$

where K_{12} is a temperature independent coefficient. N_1 and N_2 are the electron and Cooper pair concentrations in the drive (normal metal) wire and the drag (superconducting) wire, respectively. Since N_1 is constant in the temperature region concerned, $1/\tau_{12}$ has the same temperature dependence as that of N_2. From $N_2 = N[1 - (T/T_c)^4]/2$ [15], where N is the total electron concentration in the superconducting wire, we have

$$I_{drag}/I_1 \propto 1/\tau_{12} \propto N_2 \propto 1 - (T/T_c)^4. \tag{5}$$

In Fig. 4(a) we also plot the normalized electron concentration $N_0 = 2N_2/N = 1 - (T/T_c)^4$ for T_c chosen as 2.005 K. The similarity between the shapes of I_{drag}/I_1 and N_0 is strong evidence that the drag phenomenon is related to the pairing of electrons in the superconducting drag wire below the transition temperature.

Figure 4(b) shows I_{drag}/I_1 and N_0 as a function of temperature from sample 1a.1. Although this sample was with the same geometry as 2c.1, its transition region was much larger due to its large sheet resistance (2 kΩ) of AlO_x wire. At our lowest temperature (1.8 K), the resistance was still larger than 15% of the resistance at 4.2 K. However, the detected I_{drag}/I_1 had the same trend as N_0, as we saw in Fig. 4(a).

In conclusion, we believe that the observed current drag is due to phenomena predicted in Ref. [9], namely, supercurrent drag between normal electrons and Cooper pairs. First, this current coupling appeared only below T_c, and is therefore associated with Cooper pairs and not electrons in the normal state. Second, the induced open circuit voltage yielded the opposite polarity to the input current signal, consistent with the phenomenon of momentum transfer due to CMS [3,9]. Finally, the temperature dependence of the drag current, obtained indirectly from the resistance and open circuit voltage measurements, was consistent with the Coulomb interaction between the normal electrons in the drive wire and the Cooper pairs in the drive wire. However, further experiments are needed to understand why we saw much stronger coupling with our small samples (1 μm wide) than that of our large samples (10 μm wide) and that of Ref. [10] (150 μm wide).

The authors gratefully thank N. Giordano for stimulating discussions that guided us to this approach. The authors also thank W. Porod, C. Lent, S. Ruggiero, G. B. Arnold, J.-M. Duan, Z. Shao, G. Yang, and C. Zhong for very helpful discussions. This work was supported by the Office of Naval Research and the National Science Foundation.

*Electronic address: bernstei@nano2.ee.nd.edu

[1] P. J. Price, Physica (Amsterdam) **117B**, 750 (1983); in *The Physics of Submicron Semiconductor Devices,* edited by H. Grubin, D. K. Ferry, and C. Jacoboni (Plenum, New York, 1988), p. 445.

[2] P. M. Solomon, P. J. Price, D. J. Frank, and D. C. La Tulipe, Phys. Rev. Lett. **63**, 2508 (1989).

[3] T. J. Gramila, J. P. Eisenstein, A. H. MacDonald, L. N. Pfeiffer, and K. W. West, Phys. Rev. Lett. **66**, 1216 (1991); Surf. Sci. **263**, 446 (1992).

[4] P. M. Solomon and B. Laikhtman, Superlattices Microstruct. **10**, 89 (1991).

[5] B. Laikhtman and P. M. Solomon, Phys. Rev. B **41**, 9921 (1990).

[6] H. C. Tso, P. Vasilopoulos, and F. M. Peeters, Phys. Rev. Lett. **68**, 2516 (1992).

[7] H. C. Tso and P. Vasilopoulos, Phys. Rev. B **45**, 1333 (1992).

[8] A. G. Rojo and G. D. Mahan, Phys. Rev. Lett. **68**, 2074 (1992).

[9] J.-M. Duan and S. Yip, Phys. Rev. Lett. **70**, 3647 (1993).

[10] N. Giordano and J. D. Monnier, Phys. Rev. B **50**, 9363 (1994).

[11] Y. M. Wan, S. E. Hebboul, D. C. Harris, and J. C. Garland, Phys. Rev. Lett. **71**, 157 (1993).

[12] G. Deutscher, H. Fenichel, M. Gershenson, E. Grünbaum, and Z. Ovadyahu, J. Low Temp. Phys. **10**, 231 (1973).

[13] G. Bazàn and G. H. Bernstein, J. Vac. Sci. Technol. A **11**, 1745 (1993).

[14] R. E. Simpson, *Introductory Electronics for Sientists and Engineers* (Allyn and Bacon, Boston, 1987), p. 35.

[15] T. P. Orlando and K. A. Delin, *Foundations of Applied Superconductiviy* (Addison-Wesley, New York, 1991), p. 96.

Design of gate-confined quantum-dot structures in the few-electron regime

Minhan Chen and Wolfgang Porod[a)]
Department of Electrical Engineering, University of Notre Dame, Notre Dame, Indiana 46556

(Received 13 January 1995; accepted for publication 7 March 1995)

Numerical simulations for the design of gated delta-doped AlGaAs/GaAs quantum-dot structures in the few-electron regime are presented. The confining potential is obtained from the Poisson equation with a Thomas–Fermi charge model. The electronic states in the quantum dot are then obtained from solutions of the axisymmetric Schrödinger equation. Our model takes into account the effect of surface states by viewing the exposed surface as the interface between the semiconductor and air (or vacuum). Various gate configurations and biasing modes are explored. The simulations show that the number of electrons can be effectively controlled in the few-electron regime with combined enhancement and depletion gates. © *1995 American Institute of Physics.*

I. INTRODUCTION

In recent years, advanced fabrication techniques have made possible further confinement of a two-dimensional electron gas (2DEG) into wires or dots where quantum effects are significant.[1] Quantum dots have been the focus of numerous studies, and controllable loading of these dots with few electrons has been achieved,[2] allowing one to speak of quantum-dot hydrogen, quantum-dot helium, etc. Very recently, coupling between such close-by "quantum-dot atoms" has been demonstrated, thus realizing semiconductor "quantum-dot molecules."[3]

Based on the emerging technology of quantum-dot fabrication, an application of computing with coupled quantum-dot molecules has been proposed in a series of papers.[4,5] These so-called *quantum cellular automata* (QCA) are based on arrays of cells, each of which is composed of coupled quantum dots and occupied by few electrons. Figure 1(a) schematically shows a QCA cell consisting of five dots and occupied by two electrons. Due to the mutual Coulombic repulsion between the electrons, these cells exhibit bistable behavior which can be used to encode binary information.[4,5] The fabrication of such a cell is a challenging problem, yet appears to be within reach of current lithographic capability.[6] Figure 1(b) shows a possible physical realization which is based on electrostatic confinement provided by a top metallic electrode. The key implementation challenges are (i) to gain sufficient gate control in order to define quantum dots in the few-electron regime, and (ii) to place these dots sufficiently close to each other in order to make coupling possible.

In this paper, we numerically investigate the feasibility of realizing gate-controlled quantum dots in the few-electron regime for possible QCA applications. In order to achieve a crisp confining potential, we will focus on minimizing the effects of fringing fields by bringing the electrons as close as possible to the top surface. This design strategy of "trading mobility versus gate control" by utilizing near-surface 2DEGs has been pioneered by Snider *et al.*[7] However, the resultant proximity of the quantum dot to the surface raises the question of the effect of the exposed surface on the quantum confinement. In our modeling, we explicitly include the influence of surface states which are occupied, in a self-consistent fashion, according to the local electrostatic potential.[8] Our modeling will show that the simple geometry of a conventional negatively biased metal electrode as shown in Fig. 1(b) does not provide sufficient gate control for QCA applications, even for extremely shallow 2DEGs. We have therefore explored the use of dual gates which, as we will demonstrate, allows one to achieve much better control of the confining potential—a result which has also been found in recent related studies.[9,10]

There exists a large body of literature on the modeling of quantum dots; we refer to only a few representative papers.[11] Since the operation of such a device is primarily based on controlling the electron density by varying the confining potential, the modeling of the potential distribution and the electronic states in these structures is important. We obtain the confining potential from solutions of the axisymmetric Poisson equation with a Thomas–Fermi charge model. The electronic states in the quantum dot are subsequently determined from solutions of the axisymmetric Schrödinger equation using the previously calculated confining potential. Our simulation takes into account the effect of surface states by viewing the exposed surface as the interface between the semiconductor and the dielectric (air or vacuum). In our problem formulation, we view as the natural problem domain both the semiconductor and the dielectric.[8] The usual Dirichlet or von Neumann boundary conditions at the exposed semiconductor surface are replaced by more physical matching conditions at the interface between the semiconductor and the dielectric. The importance of the proper choice of boundary conditions on exposed surfaces has also been stressed in Ref. 12. Fermi-level pinning is a result of our modeling, and not an input. For the numerical treatment, we have developed a combined finite-element and boundary-element method (FBEM algorithm),[8] which is modified here for the cylindrically symmetric quantum-dot structures. We investigate the number of confined electrons and the physical size of quantum-dot structures as a function of gate geometries and biasing modes. All our modeling is performed for a temperature of 4 K.

Our modeling is aimed at exploring the parameter space for the design of quantum dots. In order to make the simulations feasible, we had to make certain simplifying assump-

a)Electronic mail: Wolfgang.Porod@ND.edu

 0021-8979/95/78(2)/1050/8/$6.00

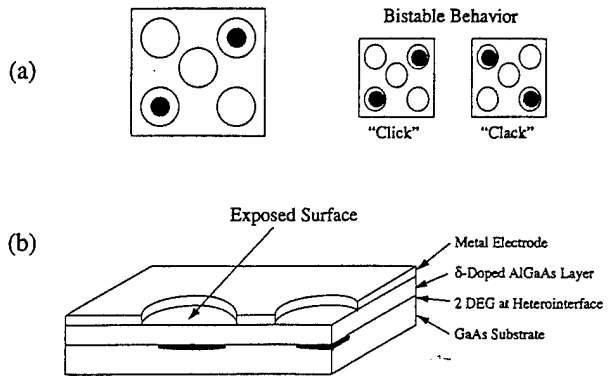

FIG. 1. (a) Schematic diagram of a bistable quantum-dot cell occupied by two electrons (see Refs. 4 and 5). (b) Physical realization by gate-controlled quantum dots.

tions. One of these assumptions is our focus on individual axially symmetric quantum dots, even though we have geometries in mind which lack this symmetry. Also, for reasons of numerical feasibility, we have chosen a Thomas–Fermi charge model in the semiconductor. Fully quantum-mechanical simulations involving the self-consistent solution of Poisson's and Schrödinger's equations tend to be computationally prohibitive. Also, the Thomas–Fermi charge model is known to be a reasonable approximation to a fully quantum-mechanical model.[13] Because of the Thomas–Fermi charge model used in our calculations, the threshold voltages we predict are too low, by approximately 20 mV, due to the spacing between the bottom of the conduction band and the lowest energy level. Another issue is the treatment of the impurities which may or may not be in thermal equilibrium with the semiconductor, depending upon the experimental conditions.[14] In our modeling we have assumed that conditions are such that the impurities are in equilibrium with the semiconductor at the given temperature.

The remainder of this paper is organized as follows. In Sec. II, we present the problem formulation including the treatment of the exposed surface. This section outlines the generalization of our previously developed FBEM solution algorithm for Poisson's and Schrödinger's equations[8] to cylindrical coordinates for the axially symmetric dot geometries. In Sec. III, we utilize the numerical calculations to discuss three different gate structures and biasing modes for the design of quantum dots in the few-electron regime. Concluding remarks are given in Sec. IV.

II. PROBLEM FORMULATION

A. Problem statement and numerical treatment

An example of a gate-confined quantum-dot structure with axial symmetry is shown in Fig. 2. In the semiconductor domain, the quantum dot is realized at the AlGaAs/GaAs heterojunction and is defined by applying an appropriate (negative) voltage V_G to the gate on the top surface. Note the opening in the gate metal which exposes the semiconductor to the dielectric (air or vacuum), as schematically shown in Fig. 2(a).

For axial symmetry, Poisson's equation can be written in cylindrical coordinates (r,θ,z),

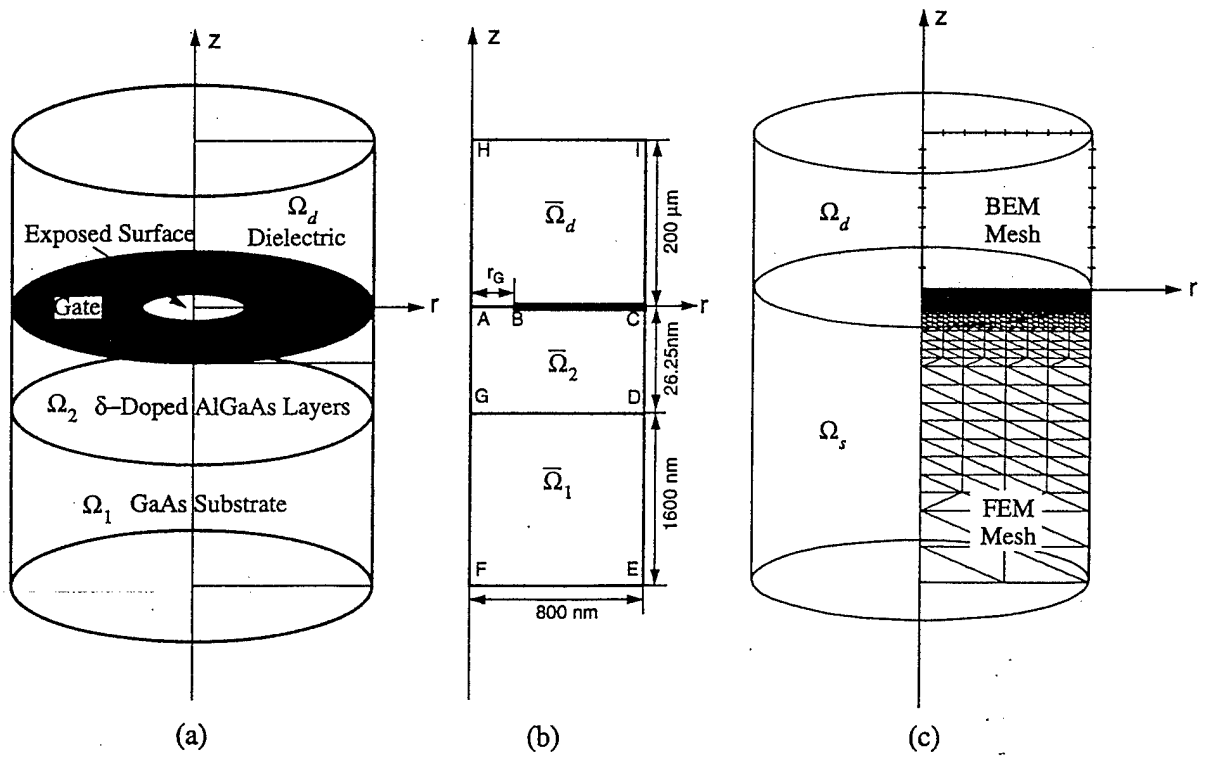

FIG. 2. Model quantum-dot structure with axial symmetry. (a) Full problem domain which consists of both the semiconductor (Ω_1 and Ω_2) and the dielectric (Ω_d) regions. (b) Two-dimensional generating areas and boundaries with typical dimensions. (c) FBEM mesh which is dense inside the semiconductor region and only consists of the discretized boundary surrounding the dielectric region.

$$\frac{1}{r}\frac{\partial}{\partial r}\left[r\epsilon\frac{\partial u(r,z)}{\partial r}\right]+\frac{\partial}{\partial z}\left[\epsilon\frac{\partial u(r,z)}{\partial z}\right]=-f[u(r,z)], \quad (1)$$

where the electrostatic potential ϕ is contained in the reduced variable $u=(E_C(\phi)-E_F)/kT$ which measures the separation between the conduction-band edge and the Fermi energy in units of the thermal energy kT, and ϵ is the dielectric constant. The right-hand-side term represents the charge density in the semiconductor, with $f=e^2(p-n+N_D^+-N_A^-)/kT$ and all symbols have their conventional meaning. A semiclassical Thomas–Fermi charge model is assumed for the equilibrium electron and hole densities which are given by a Fermi–Dirac integral of order 1/2.[8,15]

In order to solve Eq. (1), we utilize our previously developed FBEM algorithm,[8] which is a combined finite element method (FEM)[16] for the semiconductor domain and a boundary element method[17] for the dielectric region. The generating domains and boundaries are shown in Fig. 2(b), and the FBEM mesh is shown in Fig. 2(c). In its original form, the FBEM algorithm was developed for Cartesian coordinates, and we generalize it here for cylindrical coordinates. We will briefly describe the FBEM algorithm below and refer the reader to Ref. 8 for further details.

For the semiconductor domain Ω_s, with $\Omega_s=\Omega_1\cup\Omega_2$, the standard FEM discretization of Eq. (1) results in the following nonlinear system of equations:

$$\begin{aligned}&\mathbf{K}_{11}\mathbf{u}_0^s+\mathbf{K}_{12}\mathbf{u}_{BA}^s=\mathbf{P}_f^s,\\&\mathbf{K}_{12}^T\mathbf{u}_0^s+\mathbf{K}_{22}\mathbf{u}_{BA}^s=\mathbf{P}_{BA}^s,\end{aligned} \quad (2)$$

where $\mathbf{u}_{BA}^s$ and $\mathbf{P}_{BA}^s$ contain the potentials and nodal forces at the nodes on the interface $\partial\Omega_{BA}$ between the semiconductor and the dielectric, whereas $\mathbf{u}_0^s$ and $\mathbf{P}_f^s$ contain the potential and nodal forces at all other nodes inside the semiconductor domain, and $\mathbf{K}$ is the stiffness matrix.

The dielectric domain Ω_d is a charge-free region. The governing equation is Laplace's equation. Since the fundamental solution of Laplace's equation is known, a boundary integral equation technique can be employed. With the known three-dimensional fundamental solution of Laplace's equation in cylindrical coordinates and its associated dielectric flux density, the boundary contour $\partial\bar{\Omega}_d$ can be calculated explicitly in terms of complete elliptic integrals of the first and second kind, $K(m)$ and $E(m)$, respectively.[17,18] The resultant system of equations can be expressed as

$$\begin{aligned}&\mathbf{S}_{11}\mathbf{u}_0^d+\mathbf{S}_{12}\mathbf{u}_{BA}^d=\mathbf{P}_0^d,\\&\mathbf{S}_{21}\mathbf{u}_0^d+\mathbf{S}_{22}\mathbf{u}_{BA}^d=\mathbf{P}_{BA}^d,\end{aligned} \quad (3)$$

where $\mathbf{S}$ is the equivalent stiffness matrix and $\mathbf{P}^d$ is the equivalent nodal force vector.

The matching conditions at the exposed surface are given in discretized form by[8]

$$\mathbf{u}_{BA}^s=\mathbf{u}_{BA}^d=\mathbf{u}_{BA}, \quad (4)$$

$$\mathbf{P}_{BA}^s+\mathbf{P}_{BA}^d=\frac{e}{kT}\mathbf{Q}_{\text{int}}, \quad (5)$$

where $\mathbf{Q}_{\text{int}}=\mathbf{Q}_{\text{int}}(\mathbf{u}_{BA})$ is the nodal charge density on the exposed semiconductor surface.

A global system of equations is formed by coupling the semiconductor, Eq. (2), to the dielectric, Eq. (3), while enforcing the matching conditions, Eqs. (4) and (5),

$$\begin{pmatrix}\mathbf{S}_{11}&\mathbf{S}_{12}&\mathbf{0}&\mathbf{0}\\\mathbf{S}_{21}&\mathbf{S}_{22}&\mathbf{0}&\mathbf{I}\\\mathbf{0}&\mathbf{K}_{12}&\mathbf{K}_{11}&\mathbf{0}\\\mathbf{0}&\mathbf{K}_{22}&\mathbf{K}_{12}^T&-\mathbf{I}\end{pmatrix}\begin{pmatrix}\mathbf{u}_0^d\\\mathbf{u}_{BA}\\\mathbf{u}_0^s\\\mathbf{P}_{BA}^s\end{pmatrix}=\begin{pmatrix}\mathbf{P}_0^d\\\mathbf{Q}_{\text{int}}\\\mathbf{P}_f^s\\\mathbf{0}\end{pmatrix}. \quad (6)$$

Solution of this set yields the potential distribution in the semiconductor and dielectric domains, including the interface $\partial\Omega_{BA}$, and the nodal flux on $\partial\Omega_{BA}$.

The confined electronic quantum-dot states at the AlGaAs/GaAs interface are obtained by solving the axisymmetric Schrödinger equation for a computed axially symmetric potential profile $V(r,z)$,

$$\psi_l=g_l(r,z)e^{il\theta}, \quad (7)$$

$$-\frac{\hbar^2}{2m^*}\left[\frac{1}{r}\frac{\partial}{\partial r}\left(r\frac{\partial}{\partial r}\right)+\frac{\partial^2}{\partial z^2}\right]g_l(r,z)+\left[V(r,z)+\frac{\hbar^2}{2m^*}\frac{l^2}{r^2}\right]g_l(r,z)=E_l g_l(r,z). \quad (8)$$

ψ_l is the electronic wave function which may be factored due to the axial symmetry; $\exp(il\theta)$ is the angular momentum part and g_l is a function of only (r,z). $V(r,z)=kTu(r,z)$ is the axisymmetric confining potential and m^* denotes the effective mass.

The asymptotic decay of the wave function far from the dot region provides zero-valued Dirichlet and/or Neumann boundary conditions. Standard FEM discretization of Eq. (8) results in the following linear eigenvalue problem:

$$\mathbf{A}\mathbf{g}_l=E_l\mathbf{B}\mathbf{g}_l, \quad (9)$$

where $\mathbf{g}_l$ is the vector of nodal values for the axisymmetric wave functions on the (r,z) plane, and E_l is the eigenenergy. Since we are interested in only the lowest few eigenstates, Eq. (9) is solved by a subspace iteration method.[15,16] The electronic wave functions ψ_l, can then be obtained directly from Eq. (7).

B. Interface charge density on the exposed semiconductor surface

In order to solve the above problem, the interface charge density Q_{int} must be given in order to specify the matching condition (5) on the exposed semiconductor surface. It is well known that energy states lying within the band gap play a dominant role for the interface charge Q_{int} on semiconductor surfaces.[19–22]

In this paper, the surface states are assumed to possess acceptor- and donorlike characteristics,[21] with densities D_A^s and D_D^s, respectively. The semiconductor surface charge density as a function of the surface potential u_{BA} is given by Fermi–Dirac statistics with an appropriate quasi-Fermi level E_F^s for cases of applied bias[20]

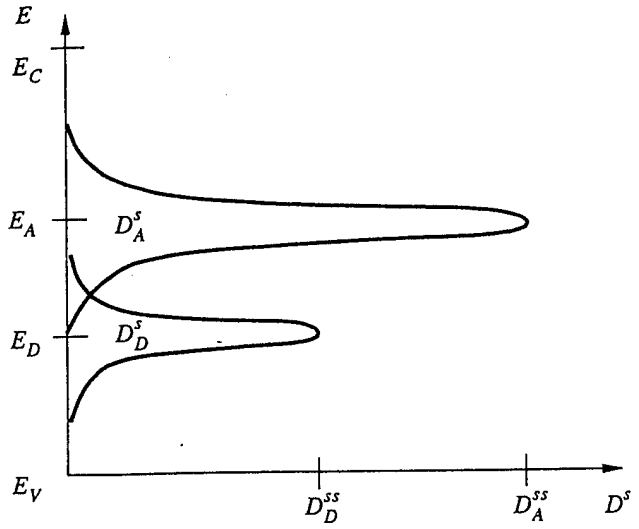

FIG. 3. Typical Gaussian energy distribution of interface states in the semiconductor band gap.

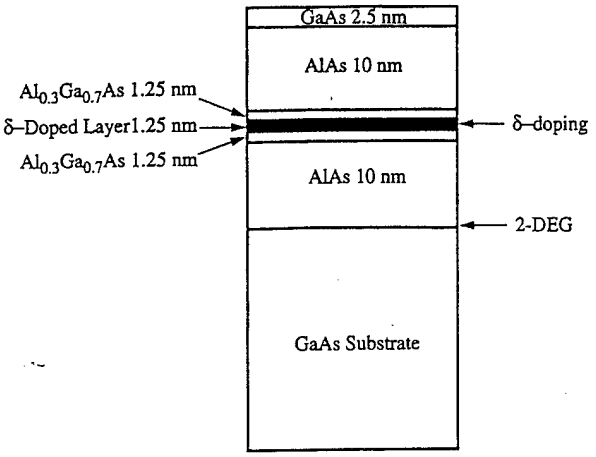

FIG. 4. Schematic diagram of the delta-doped shallow 2DEG structure utilized here (after Ref. 26).

$$Q_{\text{int}}(u_{BA}) = -e\int_{E_V}^{E_C} \frac{D_A^s}{1+\exp[(E-E_F^s)/kT]}\,dE + e\int_{E_V}^{E_C} \frac{D_D^s \exp[(E-E_F^s)/kT]}{1+\exp[(E-E_F^s)/kT]}\,dE. \quad (10)$$

As schematically shown in Fig. 3, typical Gaussian energy distributions are assumed for the surface states

$$D_A^s = D_A^{ss}\exp\left(-\frac{(E-E_A)^2}{2\Delta E_A^2}\right), \quad (11)$$

$$D_D^s = D_D^{ss}\exp\left(-\frac{(E-E_D)^2}{2\Delta E_D^2}\right). \quad (12)$$

The acceptor- (donor-) like surface-state densities are characterized by their height D_A^{ss} (D_D^{ss}), centroid E_A (E_D), and width ΔE_A (ΔE_D).

In our surface charge model, following Ref. 21, the acceptor- and donorlike states are assumed to be centered around energies $E_A = 0.75$ eV and $E_D = 0.5$ eV, respectively, measured from the valence-band edge. In the available literature, there are no unique agreed-upon values for the heights and the widths of the distributions, but there is general agreement on the range of the parameters. Here, we assume equal values for the acceptor- and donorlike surface-state density peaks $D_A^{ss} = D_D^{ss} = 6 \times 10^{14}$ cm^{-2}eV^{-1} and widths $\Delta E_D = \Delta E_A = 0.1$ eV. With this choice of parameter values, we are able to reproduce the observed Fermi-level pinning behavior.[19–22] In the above choice of the parameter values, the location of the charge centroids is critical. Less critical are the peak heights and widths, which may be varied over the range of values reported in the literature,[19–22] while still yielding Fermi-level pinning behavior. These issues pertaining to the choice of the surface-state charge model will be discussed in greater detail elsewhere.[23]

The strong nonlinearity of the interface charge as a function of the band bending at the surface may cause numerical convergence problems, particularly for low temperatures. We implemented a modified Bank–Rose damping scheme to stabilize the convergence by adaptive underrelaxation and to accelerate the convergence speed of Newton's method.[24,25] The combination of our coupled axisymmetric finite-

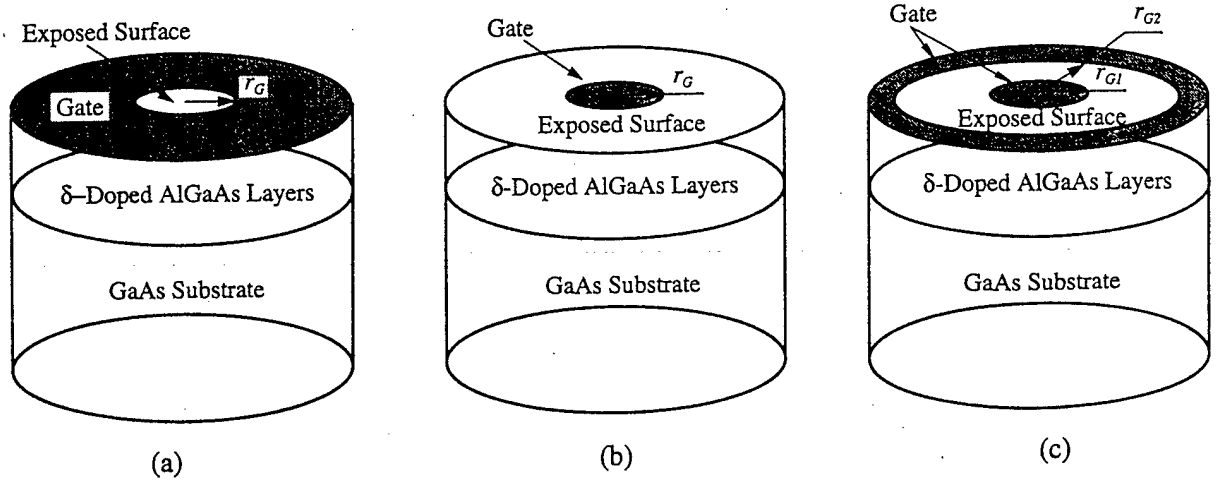

FIG. 5. Three types of top gate structures with axial symmetry: (a) depletion gate, (b) enhancement gate, and (c) combined enhancement/depletion gates.

element/boundary-element algorithm and the adaptive damping scheme was found to perform quite satisfactorily.

III. QUANTUM-DOT DESIGN

The results shown in this section concentrate on the design of quantum dots in the few-electron regime for possible applications in QCA.[4,5] Our simulations are based on the delta-doped AlGaAs/GaAs structure reported in Ref. 26, where it was shown that sheet carrier concentrations of 3.4×10^{11} cm^{-2} and Hall mobilities of 1.2×10^{6} cm^{2} V^{-1} s^{-1} at 4 K may be achieved with a shallow 2DEG 25 nm below the semiconductor/vacuum interface. Figure 4 shows the layer structure utilized in our modeling below.

We will explore three types of axially symmetric top gate geometries, which are schematically shown in Fig. 5. The conventional biasing mode is one where a negative bias is applied to the gate, thus depleting the 2DEG underneath the metal electrode; we will refer to this mode as "depletion mode" biasing. As shown in Fig. 5(a), a quantum dot may be realized below the circular hole in the negatively biased gate. One may also utilize structures with an initially depleted 2DEG, e.g., by surface depletion due to Fermi-level pinning. An electron density may then be induced underneath a positively biased gate. This so-called "enhancement mode" biasing is schematically shown in Fig. 5(b). By combining the above two mechanisms, we designed a third type of quantum-dot structure with combined center enhancement and surrounding depletion gates, as shown in Fig. 5(c). We will demonstrate that the dot occupation in this combined enhancement/depletion mode can be accurately controlled by adjusting the positive and/or negative bias on the gates.

A. Depletion gates

The n-type sheet doping concentration for the delta-doped AlGaAs layer is assumed to be 5.0×10^{12} cm^{-2} which leads to the formation of a 2DEG along the AlAs/GaAs heterointerface without gate bias. By applying a sufficiently negative bias to the top gate shown in Fig. 5(a), a quantum dot may be realized. For typical parameter values, the resulting potential variations inside the semiconductor are plotted in Fig. 6, (a) perpendicular and (b) parallel to the surface. Figure 6(a) shows a plot of the conduction-band profile perpendicular to the semiconductor surface at the center of the circular gate opening. Electrons accumulate at the GaAs–substrate/AlAs interface, where the conduction-band edge dips below the Fermi level which is taken as the zero of the energy scale. Care has to be taken that no parallel conducting layer forms in the dopant plane. Figure 6(b) is a plot of the conduction-band edge parallel to the heterointerface (on the GaAs side), which shows the quantum-dot confining potential. Again, electron accumulation occurs in the region where the conduction band dips below the semiclassical Fermi level indicated by an arrow. The physical size of the quantum dot can be measured as the radius of the circular cross section of the conduction band at the Fermi level, which we will call the "physical dot radius" r_{dot}. Device applications of such a structure are based on the ability to utilize the gate bias and the gate size to modulate both the number of the confined electrons and the physical size of the quantum dots.

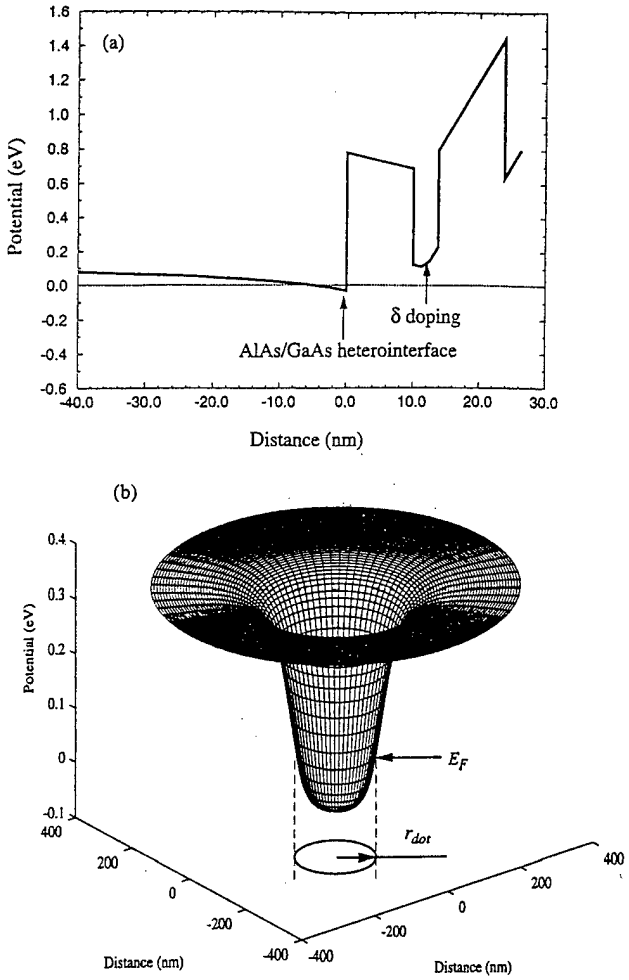

FIG. 6. Typical quantum-dot potential profile where the Fermi level E_F and the physical dot radius r_{dot} are indicated: (a) perpendicular to the semiconductor surface at the center of the dot, (b) parallel to the substrate GaAs/AlAs heterointerface (on the GaAs side).

Figure 7 shows the size and occupation of quantum dots for depletion mode biasing. The radius of quantum dots, r_{dot}, induced by three different sizes of metal–electrode openings, r_G, is plotted in Fig. 7(a) as a function of the (negative) gate bias voltage. As expected, the dot radius decreases with increasing gate bias. Eventually, the dot is completely depleted at a certain threshold voltage, which depends upon the gate geometry. Figure 7(b) shows the corresponding number of electrons in each dot, which is obtained by integrating the electron density over the dot region. We see that the occupation number sensitively depends upon the gate bias, and that the few-electron regime may be realized for reasonable values of gate dimensions and bias voltages. As an example, for a 50-nm-radius metal-gate opening, the few-electron regime is reached for a (negative) bias greater than 0.5 V; however, for a bias greater than a threshold of 0.53 V, the dot is totally depleted.

Note that the confining potential is rather gradual (perhaps surprisingly so). In order to achieve a dot radius of, say, 10 nm, the radius of the gate opening has to be at least 30 nm. Even though we are utilizing here a 2DEG which is extremely close to the surface, the features in the plane of the

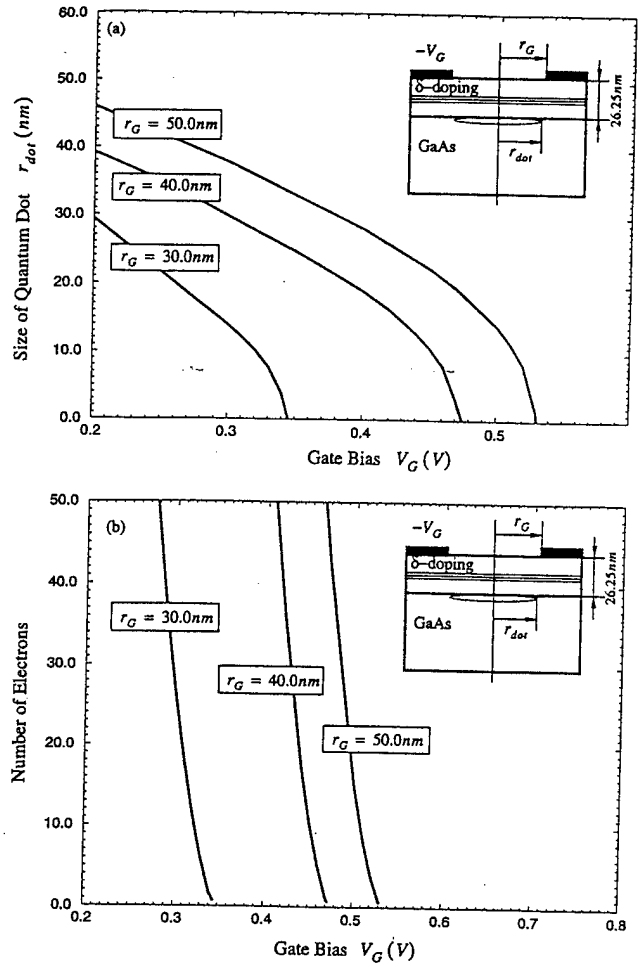

FIG. 7. Size and occupation of quantum dots for depletion mode biasing. (a) Radius of quantum dots, r_{dot}, induced for three different sizes of metal–electrode openings, r_G, as a function of the (negative) gate bias voltage; (b) corresponding number of electrons in each dot.

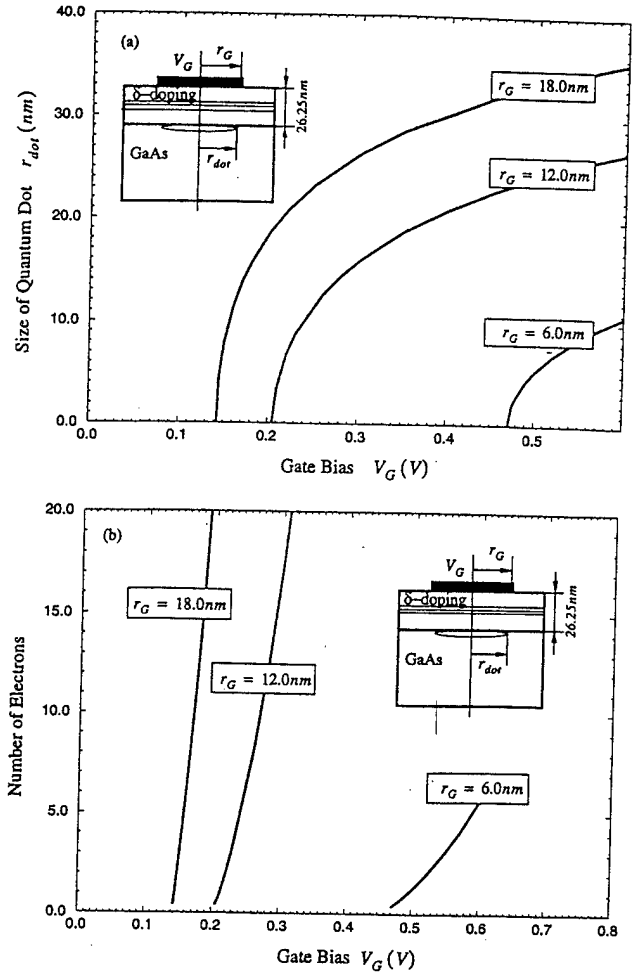

FIG. 8. Size and occupation of quantum dots for enhancement mode biasing. (a) Radius of quantum dots, r_{dot}, induced for three different sizes of metal electrodes, r_G, as a function of the (positive) gate bias voltage; (b) corresponding number of electrons in each dot.

electrons are a factor of 3 (or more) smaller than the features of the surface gates. As a consequence, it is not possible to place dots (in the 2DEG plane) close to each other (since they cannot be closer than the corresponding openings in the metal electrode). We conclude that depletion mode biasing is not a promising candidate for QCA applications.

B. Enhancement gates

The n-type sheet doping concentration for the delta-doped AlGaAs layer is now assumed to be 3.0×10^{12} cm^{-2} which leads to a normally depleted 2DEG. Without an applied gate bias, the conduction-band edge along the GaAs/AlAs heterointerface is close *and* above the Fermi level due to the effect of the pinned GaAs surface potential. By applying a small positive bias on the center circular gate, shown in Fig. 5(b), quasi-zero-dimensional electronic states may be induced underneath the top electrode.

Figure 8 shows the size and occupation of quantum dots for enhancement mode biasing. The radius of quantum dots, r_{dot}, induced by three different sizes of metal electrodes, r_G, is plotted in Fig. 8(a) as a function of the (positive) gate bias voltage. Again, Fig. 8(b) shows the corresponding number of electrons in each dot. For larger gate biases, both the radius and the occupation of each dot increases. For example, for a circular enhancement gate with 12 nm radius, the threshold voltage is about 0.2 V and, in the few-electron regime, an additional electron is added for every 10 mV increment in the gate bias.

The control of the threshold voltage in this mode is critical. The gate bias cannot be too large since the structure becomes leaky due to tunneling between the 2DEG and the metal electrode. Another problem at positive biasing is that parasitic electron accumulation occurs in the delta-doped layers, as may be seen from Fig. 6(a).

We see that in this mode, the induced quantum dot (in the plane of the electrons) may be similar in size to the top metal electrode. QCA applications appear to be feasible, since it is possible to realize arrangements of quantum dots which are *both* close together *and* occupied by few electrons.

C. Combined enhancement/depletion gates

We will now demonstrate that a combination of enhancement and depletion gates, schematically shown in Fig. 5(c), provides effective control of the threshold voltage. The main

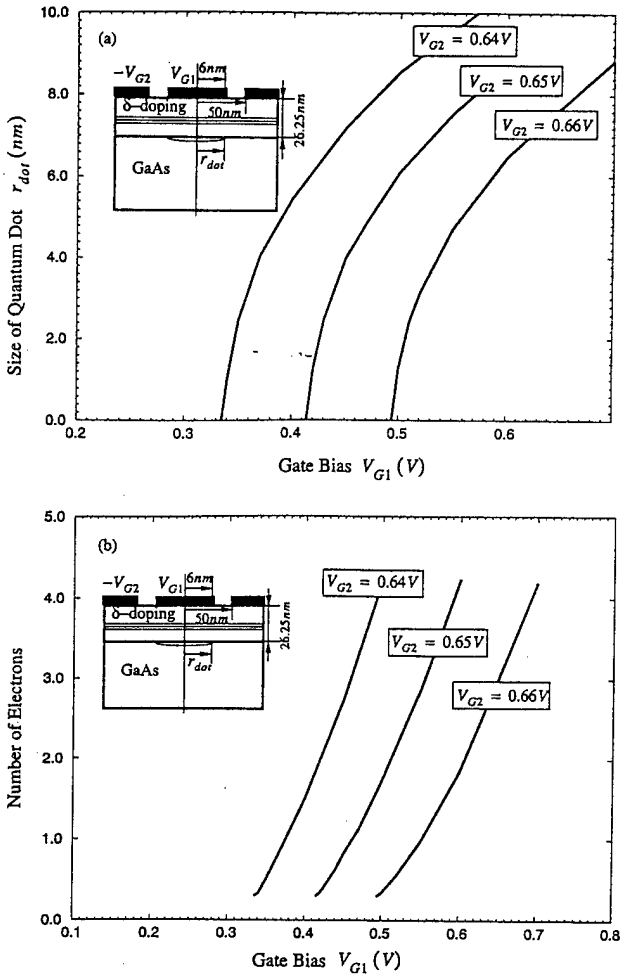

FIG. 9. Size and occupation of quantum dots for combined enhancement/depletion mode biasing. The gate dimensions are indicated in the insets. (a) Radius of quantum dots, r_{dot}, induced by three different voltages on the depletion gate V_{G2} as a function of the enhancement gate bias voltage V_{G1}. (b) Corresponding number of electrons in each dot.

idea is to negatively bias the outer gates (gate 2) such that the electron density is depleted or near depletion; a positive bias on the inner gate (gate 1) is then utilized to induce the dot and to control its occupation.

Figure 9 shows an example of the size and occupation of quantum dots for combined enhancement/depletion mode biasing. The n-type sheet doping concentration for the delta-doped AlGaAs layer is assumed to be 3.0×10^{12} cm^{-2}, which is the same as for the above enhancement gate structure. In this example, we have chosen a radius of $r_{G1}=6$ nm for the center enhancement gate, and a radius of $r_{G2}=50$ nm for the surrounding depletion gate. The radius of quantum dots, r_{dot}, induced by three different voltages on the depletion gate V_{G2} is plotted in Fig. 9(a) as a function of the enhancement gate bias voltage V_{G1}. Figure 9(b) shows the corresponding number of electrons in each dot. We see that variations of the depletion gate bias of 10 mV will result in threshold-voltage variations of as much as 80 mV. This biasing mode appears to be an effective way of controlling the quantum-dot threshold voltage in the few-electron regime.

Note that the curves in Fig. 9(b) are much less steep than the corresponding ones in Figs. 8(b) and 7(b). This means

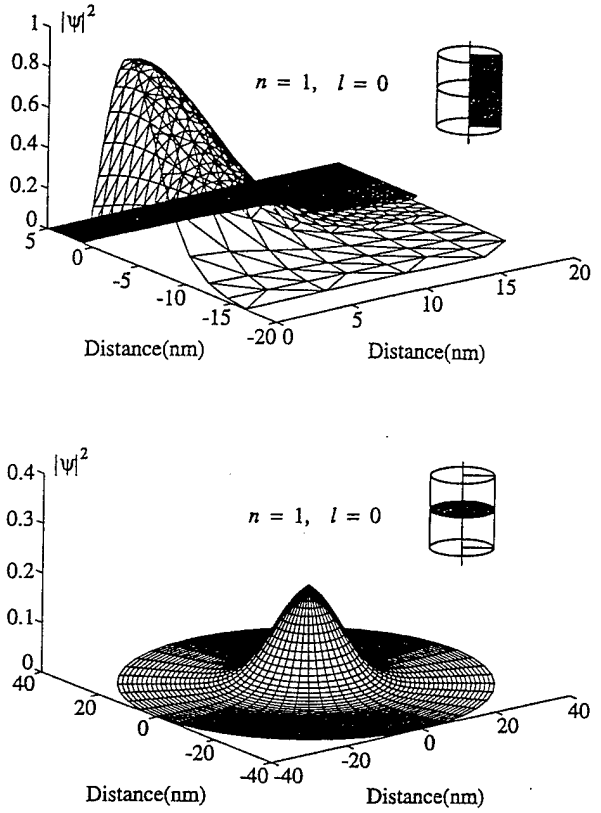

FIG. 10. Typical lowest energy wave function. As schematically shown in the insets, the upper panel is a plot in the (r,z) plane, and the lower panel in the (r,θ) plane at the GaAs/AlAs heterointerface.

that the combined enhancement/depletion mode allows more effective gate control of the quantum-dot occupation than either the enhancement or depletion modes alone.

Several enhancement gates may be placed inside the same depletion gate opening. In particular, one depletion gate may define a single QCA cell and each dot is realized by separate enhancement gates. Work on utilizing this design strategy to realized QCA is in progress.

D. Quantized electronic states

The quantum-dot structures support three-dimensionally confined electronic states. The separation of the quantized energy levels is also of interest for applications. To this end, we have solved the axisymmetric Schrödinger equation, Eqs. (7) and (8), for a given confining potential.

Figures 10 and 11 show a typical example of the wave functions for the first and second electronic states, respectively. The wave function of the lowest energy state is plotted in the upper panel of Fig. 10 in the (r,z) plane and in the lower panel in the (r,θ) plane, as schematically indicated in the insets. The corresponding plots of the wave function of the second-lowest energy state are shown in Fig. 11. The energy separation in this example (enhancement gate structure with a 20 nm radius) is $E_2-E_1=13$ meV.

IV. CONCLUSION

We have presented our numerical simulations for the design of gated delta-doped AlGaAs/GaAs quantum-dot struc-

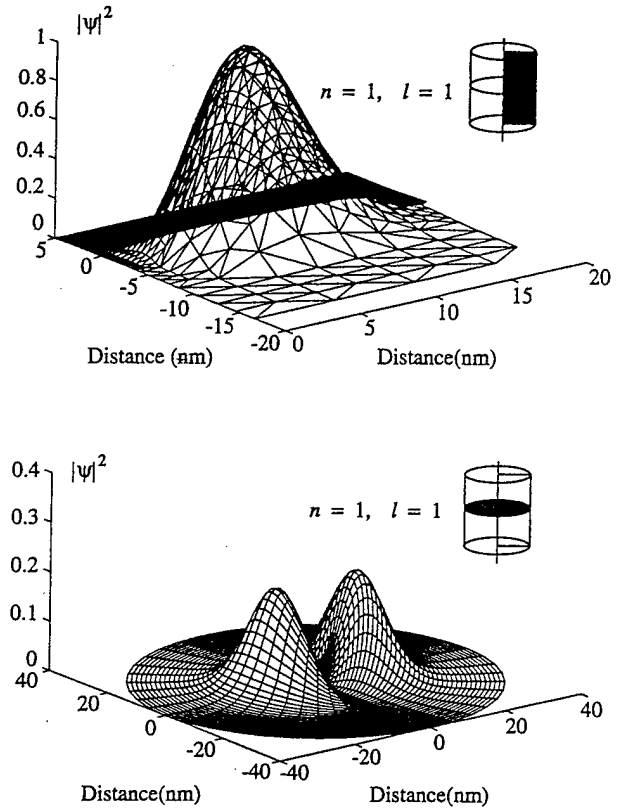

FIG. 11. Typical second-lowest energy wave function. As schematically shown in the insets, the upper panel is a plot in the (r,z) plane, and the lower panel in the (r,θ) plane at the GaAs/AlAs heterointerface.

tures in the few-electron regime. The confining potential is obtained from the axisymmetric Poisson equation with a semiclassical Thomas–Fermi charge model. The electronic states in the quantum dot are subsequently determined from solutions of the axisymmetric Schrödinger equation using the previously calculated confining potential. Our simulation takes into account the effect of surface states by viewing the exposed surface as the interface between the semiconductor and the dielectric (air or vacuum). For the numerical treatment, we have developed a combined finite-element and boundary-element method (FBEM algorithm).

Utilizing a realistic material system with a shallow 2DEG, we have demonstrated that it is possible to realize quantum-dot structures in the few-electron regime. Our results indicate that the most promising design strategy is to utilize combined enhancement/depletion gates, which allow effective control of the threshold voltage. These structures appear to be promising candidates for future QCA applications.

ACKNOWLEDGMENTS

The authors wish to thank Greg Bazán, Dr. Gary H. Bernstein, Dr. Henry K. Harbury, Dr. David J. Kirkner, Dr. Craig S. Lent, Xinhui Niu, Dr. Zhian Shao, Dr. R. Kent Smith, and Dr. Gregory L. Snider for numerous helpful discussions and suggestions. This work was supported in part by AFOSR and ARPA/ONR.

[1] *Nanostructures and Mesoscopic Systems*, edited by W. P. Kirk and M. A. Reed (Academic, Boston, 1992).
[2] Ch. Sikorski and U. Merkt, Phys. Rev. Lett. **62**, 2164 (1989); J. Alsmeier, E. Batke, and J. P. Kotthaus, Phys. Rev. B **41**, 1699 (1990); B. Meurer, D. Heitman, and K. Ploog, Phys. Rev. Lett. **68**, 1371 (1992); R. C. Ashoori, H. L. Störmer, J. S. Weiner, L. N. Pfeiffer, K. W. Baldwin, and K. W. West, *ibid.* **71**, 613 (1993); H. Drexler, D. Leonard, W. Hansen, J. P. Kotthaus, and P. M. Petroff, *ibid.* **73**, 2252 (1994).
[3] M. Kemerink and L. W. Molenkamp, Appl. Phys. Lett. **65**, 1012 (1994); S. W. Hwang, B. D. Yu, T. Sakamoto, and K. Nakamura, Superlatt. Microstruct. (in press); F. Hofmann, T. Heinzel, D. A. Wharam, J. P. Kotthaus, G. Böhm, W. Klein, G. Tränkle, and G. Weimann (preprint, 1995).
[4] C. S. Lent, P. D. Tougaw, W. Porod, and G. H. Bernstein, Nanotechnology **4**, 49 (1993).
[5] C. S. Lent, P. D. Tougaw, and W. Porod, Appl. Phys. Lett. **62**, 714 (1993); P. D. Tougaw, C. S. Lent, and W. Porod, J. Appl. Phys. **74**, 3558 (1993).
[6] X. Huang, G. Bazán, and G. H. Bernstein, J. Vac. Sci. Technol. B **11**, 2565 (1993).
[7] G. L. Snider, M. S. Miller, M. J. Rooks, and E. L. Hu, Appl. Phys. Lett. **59**, 2727 (1991); G. L. Snider, I.-H. Tan, and E. L. Hu, J. Appl. Phys. **68**, 5922 (1990).
[8] M. Chen, W. Porod, and D. J. Kirkner, J. Appl. Phys. **75**, 2545 (1994).
[9] Y. Wang and S. Y. Chou, Appl. Phys. Lett. **63**, 2257 (1993); **64**, 309 (1994); **65**, 2072 (1994).
[10] J. P. Lu, X. Ying, and M. Shayegan, Appl. Phys. Lett. **65**, 2320 (1994).
[11] A. Kumar, S. E. Laux, and F. Stern, Phys. Rev. B **42**, 5166 (1990); D. Pfannkuche and R. R. Gerhardts, Phys. Rev. B **44**, 13132 (1991); M. Macucci, K. Hess, and G. J. Iafrate, *ibid.* **48**, 17354 (1993); M. Stopa, *ibid.* **48**, 18340 (1993).
[12] J. H. Davies and I. A. Larkin, Phys. Rev. B **49**, 4800 (1994).
[13] J. H. Luscombe, Nanotechnology **4**, 1 (1993).
[14] A. Kumar, S. E. Laux, F. Stern, A. Zaslavsky, J. M. Hong, and T. P. Smith, III, Phys. Rev. B **48**, 4899 (1993).
[15] W. Porod, H. K. Harbury, and S. M. Goodnick, Appl. Phys. Lett. **61**, 1823 (1992); H. K. Harbury, W. Porod, and S. M. Goodnick, J. Appl. Phys. **73**, 1509 (1993).
[16] K. J. Bathe, *Finite Element Procedures in Engineering Analysis* (Prentice-Hall, Englewood Cliffs, NJ, 1982).
[17] C. A. Brebbia, J. C. F. Telles, and L. C. Wrobel, *Boundary Element Techniques* (Springer, Berlin, 1984).
[18] *Handbook of Mathematical Functions with Formulas, Graphs, and Mathematical Tables*, edited by M. Abramowitz and I: A. Stegun (Dover, New York, 1965).
[19] E. H. Rhoderick and R. H. Williams, *Metal–Semiconductor Contacts* (Oxford University, New York, 1988).
[20] A. M. Cowley and S. M. Sze, J. Appl. Phys. **36**, 3212 (1965).
[21] W. E. Spicer, I. Lindau, P. Skeath, and C. Y. Su, J. Vac. Sci. Technol. **17**, 1019 (1980).
[22] W. Mönch, Surf. Sci. **132**, 92 (1983).
[23] M. Chen and W. Porod (unpublished).
[24] R. E. Bank and D. J. Rose, SIAM J. Numer. Anal. **17**, 806 (1980).
[25] D. Kincaid and W. Cheney, *Numerical Analysis* (Brooks/Cole, Belmont, 1991).
[26] J. E. F. Frost, D. A. Ritchie, and G. A. C. Jones, J. Cryst. Growth **111**, 305 (1991).

Superlattices and Microstructures, Vol. 20, No. 4, 1996

Practical issues in the realization of quantum-dot cellular automata

GARY H. BERNSTEIN, GREG BAZAN, MINHAN CHEN, CRAIG S. LENT,
JAMES L. MERZ, ALEXEI O. ORLOV, WOLFGANG POROD,
GREG L. SNIDER, P. DOUGLAS TOUGAW
Dept. of Electrical Engineering, University of Notre Dame, Notre Dame, IN 46556, U.S.A.

(Received 20 May 1996)

Several practical issues in the development and operation of quantum-dot cellular automata (QCA) cells and systems are discussed. The need for adiabatic clocking of QCA systems and modeling of electrostatic confinement of quantum dots are presented. Experimental data on dot coupling and applications to QCA detectors in a 2-dimensional electron gas (2DEG) are presented. We report a charge detection scheme where we observe strong modulation in the detector signal, in addition to the detector exhibiting minimal effect on the dot being measured. With this investigation, we demonstrate these two key components required for QCA in AlGaAs/GaAs materials, namely dot coupling and charge-state detection.

1. Introduction

Quantum cellular automata (QCA) has been proposed [1, 2] as a new technique for performing computation through the use of quantum dots. The basic principle is shown schematically in Fig. 1A. A QCA cell consists of quantum dots arranged such that, e.g. four sites may be occupied by two electrons with semitransparent barriers connecting the dots in some configuration so that, through tunneling, electrons may arrange themselves in their energetically lowest positions. As shown in the figure, the lowest energy state of the electrons places them at corners of the cells aligned along either diagonal, the polarization of which can correspond to either a logic '1' or '0'.

Two cells may be placed adjacent to each other such that they interact only Coulombically, with no tunneling between cells allowed, as shown in the inset of Fig. 1B. The polarization of a cell due to that of its neighbors is very high, such that slight polarization of one cell strongly forces the polarization of its neighbors. Systems designed by Lent *et al.* [3] and Fountain [4] demonstrate that extremely complex digital logic systems can be built up from basic building blocks consisting of 'wires' (chains of cells), invertors, AND gates, OR gates, and majority logic cells. For example, a full adder circuit with a dot size of 10 nm would fit inside an area of about 1 square micron [3]. It is important to note that the design of 'crossover' configurations allows the entire system to exist in a plane, with no out-of-plane interconnects required.

2. Switching behavior of QCA systems

QCA arrays may be switched abruptly, in which case the system is placed in an excited state by the rapid

0749–6036/96/080447 + 13 $25.00/0

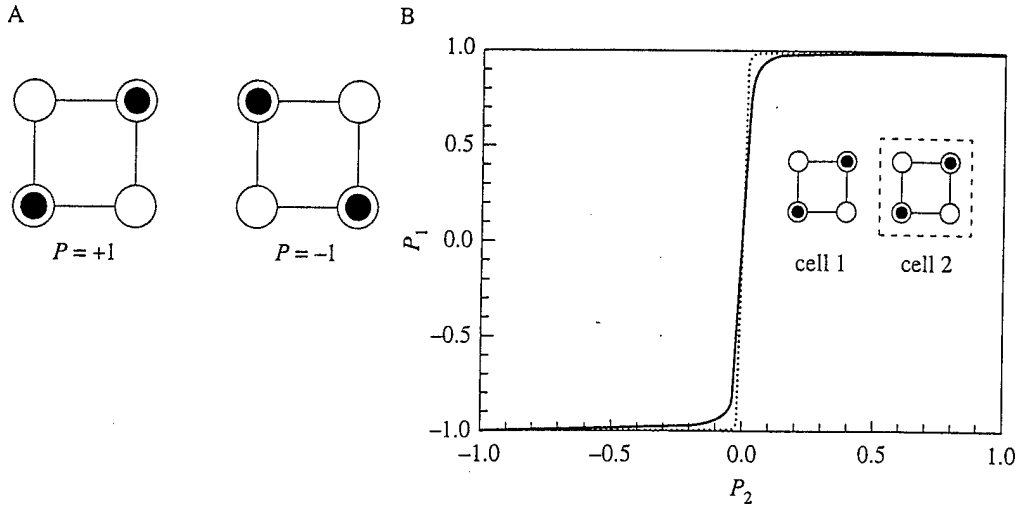

Fig. 1. Quantum-dot cellular automata. A, Schematic of the basic four-site cell. Coulombic repulsion causes the electrons to occupy antipodal sites within the cell. Each configuration can be assigned a digital logic value. B, The cell–cell response. The polarization of cell 2 is fixed and its Coulombic effect on that of cell 1 is measured. The nonlinearity and bistable saturation of this response serves the same role as gain in a conventional digital circuit.

change of a driver cell, and decays through inelastic processes to its ground state. The resulting configuration of the cells is the outcome of a single calculation. It is also possible to switch QCA devices in such a way that the array remains in its instantaneous ground state at all times. The adiabatic theorem guarantees that this is possible if the switching time is slow compared to the time associated with transitions to the first excited state of the array. As shown in Fig. 2, the first step in adiabatic switching is to lower the intra-dot barriers within each cell, reducing the electron localization imposed by high barriers. Barriers between cells remain high. The driver cell polarization is then switched adiabatically, followed by adiabatically re-asserting the barriers, which returns the localization of the electrons and the polarization of the cell.

A study of the allowable speed of such switching has shown that the non-adiabatic error, which is due to switching the devices too quickly to be strictly adiabatic, decreases exponentially with the time during which the devices are switched. This exponential decrease is shown in Fig. 3 for a simple one-cell majority logic gate and a larger five-cell extended majority logic gate. In spite of the fact that the five-cell device requires more time than the single-cell device to switch with the same level of accuracy, both errors decrease exponentially with switching time. Preliminary results on the scaling of switching time with the number of cells in an array have shown switching time increases, at worst, in an approximately linear relationship with the number of cells in an array. Adiabatic switching has the significant advantage that it provides a means of maintaining clocked control over the calculation and eliminates dependence on inelastic processes in accomplishing device switching.

3. Basic elements of QCA systems

The notion that controlled use of single electrons has progressed beyond basic physics is evident from proposals of, for example, circuits and systems based on single electron tunneling [5–7]. Interest in these systems is focusing less on the study of basic physical phenomena, and increasingly on how to assemble building blocks in the design of more complex systems for the attainment of truly revolutionary applications. It is relevant, then, to discuss what are the important building blocks for the creation of QCAs.

The basic elements of QCA require (1) that the appropriate number of (extra) electrons be induced in each

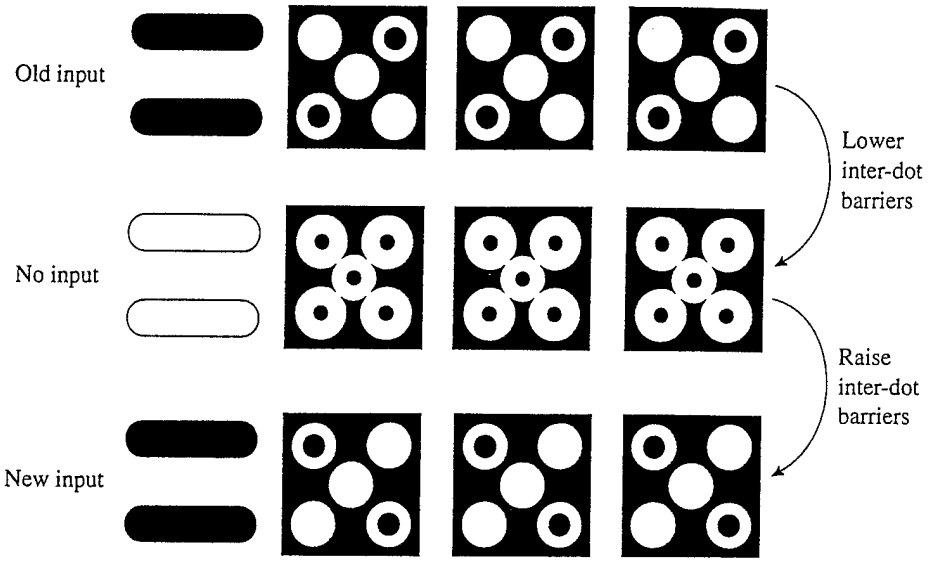

Fig. 2. A schematic representation of the adiabatic switching of an array of QCA cells. The intra-dot barriers are adiabatically lowered, decreasing the localization of the electrons within each cell. The old input is removed, and a new input is applied, followed by a re-application of the intra-dot barriers. This causes the cells to exhibit the ground state corresponding to the new input.

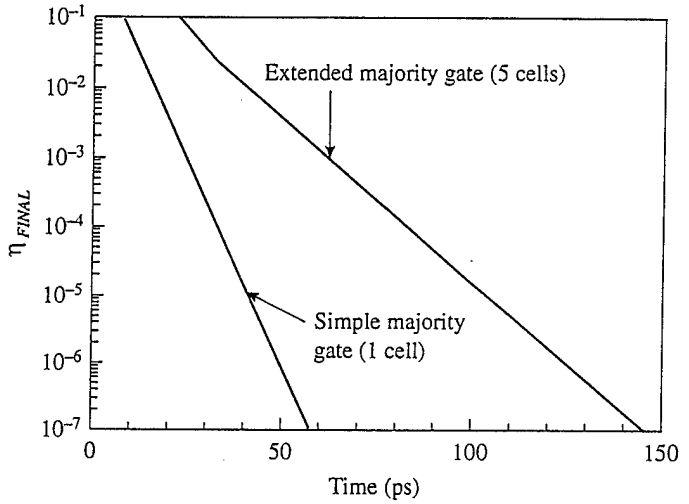

Fig. 3. The non-adiabatic error introduced by switching a QCA array can be measured by the total projection of the cell state on all non-ground state basis vectors after switching is complete. This non-adiabatic error decreases exponentially with the amount of time allowed for switching the device. This figure shows the exponential decrease for two systems—a simple one-cell majority logic gate and a more complicated five-cell extended majority logic gate.

cell, (2) that dots be sufficiently close to allow inter-dot tunneling, (3) that adjacent cells be close enough to permit Coulomb coupling, and (4) that the cell polarization state be detected. Although one can envisage QCA behavior in such varied systems as metal tunnel junctions [8, 9], Si inversion layers, self-assembled quantum dots [10], nanomagnet arrays, vertical quantum dots, or even arrays of individual molecules, we have chosen to do our initial studies in the well-characterized AlGaAs/GaAs system, which currently offers

a large array of useful building blocks. Demonstrations of Coulomb blockade and single electron tunneling through quantum dots for charge entrapment, single electron transistors for control of dot occupancy, and single-electron electrometers [11–13] for charge detection are all available to the design engineers of future single-electronic applications.

4. Modeling for QCAs

For the calculations discussed so far, modeling behavior of arrays of quantum-dot cells, it is appropriate to use an extended Hubbard-type Hamiltonian and describe the individual dots simply as sites. We now turn to the issue of designing the optimal gate patterns to realize these cells in semiconductor systems. For that, one must employ realistic models of the detailed semiconductor-gate geometry.

In order to design optimal cells, it is important that potential profiles and electron density be calculated through the accurate solution of Poisson's equation. To this end, we have performed numerical simulations for the design of quantum dot structures in the few-electron regime, both in the GaAs/AlGaAs and Si/SiO_2 material systems. The confining potential is obtained from the Poisson equation within a Thomas–Fermi charge model. The electronic states in the quantum dot are then obtained from solutions of the axisymmetric Schrödinger equation. Our model takes into account the effect of surface states by viewing the exposed surface as the interface between the semiconductor and air (or vacuum). This is particularly important for modeling the III-V material system, where surface states have to be taken into account. We explore various gate configurations and biasing modes. Our simulations show that the number of electrons can be effectively controlled in the few-electron regime with combined enhancement and depletion gates.

The goal of this modeling is to numerically investigate the feasibility of realizing gate-controlled quantum dots in the few-electron regime for QCA applications. In order to achieve a crisp confining potential, minimization of the effects of fringing fields will be focused on, by bringing the electrons as close as possible to the top surface. This design strategy of 'trading mobility versus gate control' by utilizing near-surface 2DEGs has been pioneered by Snider, Hu and co-workers [14, 15]. However, the resultant proximity of the quantum dot to the surface raises the question of the effect of the exposed surface on the quantum confinement. In our modeling, we explicitly include the influence of surface states which are occupied, in a self-consistent fashion, according to the local electrostatic potential [16]. Our modeling has shown that the simple geometry of a conventional metal electrode used for electrostatic confinement does not provide sufficient gate control for QCA applications, even for extremely shallow 2DEGs. We have therefore explored the use of dual gates which allows one to achieve superior control of the confining potential [17].

We will now demonstrate that a combination of enhancement and depletion gates, as shown in the inset of Fig. 4A, provides effective control of the threshold voltage. The main idea is to negatively bias the outer gates (gate 2) such that the electron density is depleted or near depletion; a positive bias on the inner gate (gate 1) is then utilized to induce the dot and to control its occupation.

Figure 4A shows an example of the size and occupation of quantum dots for combined enhancement/depletion mode biasing on an AlGaAs/GaAs 2DEG. The n-type sheet doping concentration for the delta-doped AlGaAs layer is assumed to be 3×10^{12} cm^{-2}. In this example, we have chosen a radius of $r = 6$ nm for the center enhancement gate, and a radius of $r_{G2} = 50$ nm for the surrounding depletion gate. The radius of quantum dots, r_{dot}, induced by three different voltages on the depletion gate, V_{G2}, is plotted as a function of the enhancement gate bias voltage, V_{G1}. Figure 4B shows the corresponding number of electrons in each dot (note that fractional dot occupancies are possible because of the semi-classical model used).

We see that variations of the depletion-gate bias of 10 mV will result in threshold-voltage variations of as much as 80 mV. This biasing mode appears to be an effective way of controlling the quantum-dot threshold voltage in the few-electron regime.

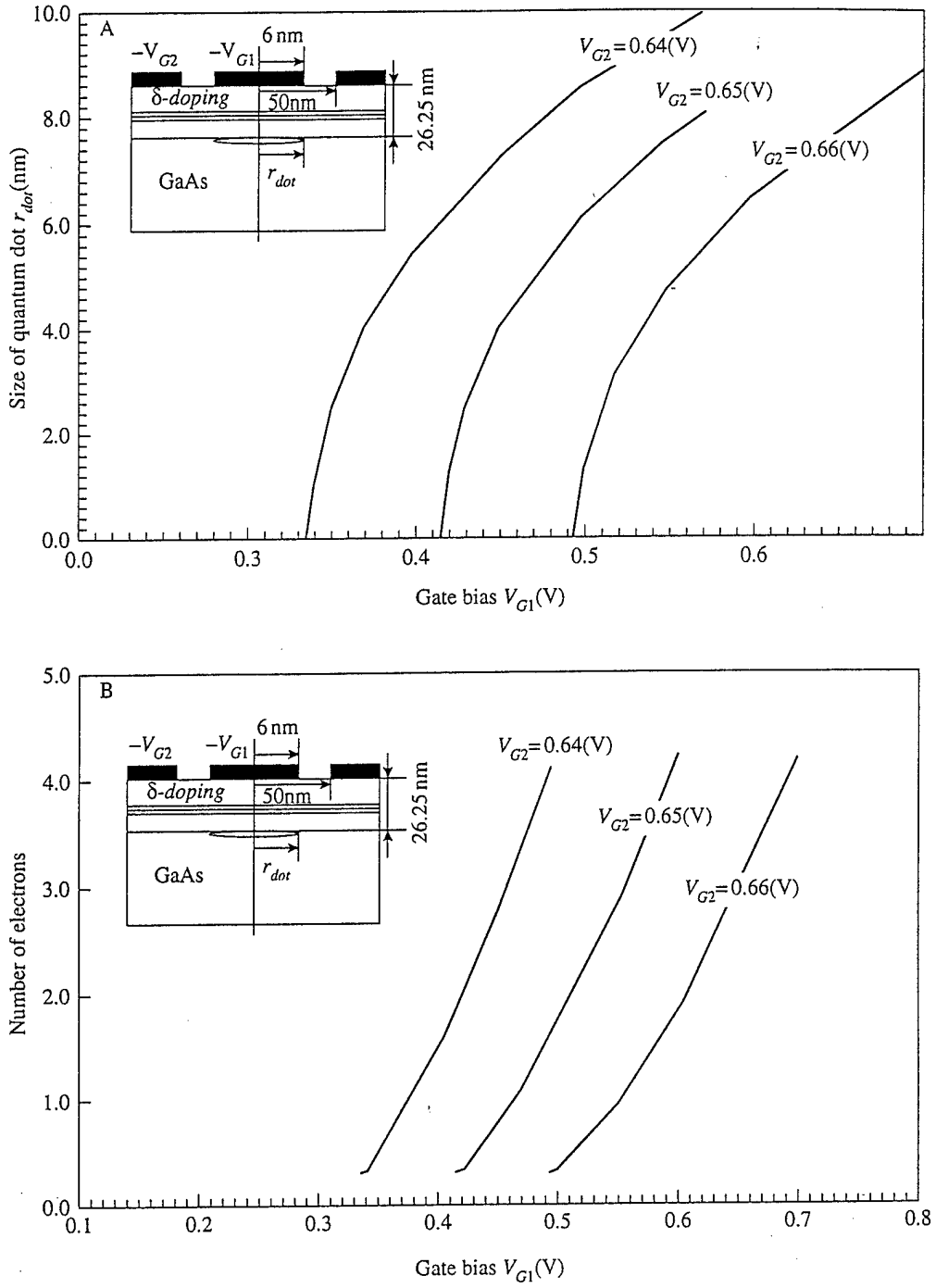

Fig. 4. Size and occupation of quantum dots for combined enhancement/depletion mode biasing. The gate dimensions are indicated in the insets. A, Radius of quantum dots, r_{dot}, induced by three different voltages on the depletion gate, V_{G2}, as a function of the enhancement gate bias voltage, V_{G1}. B, Corresponding number of electrons in each dot.

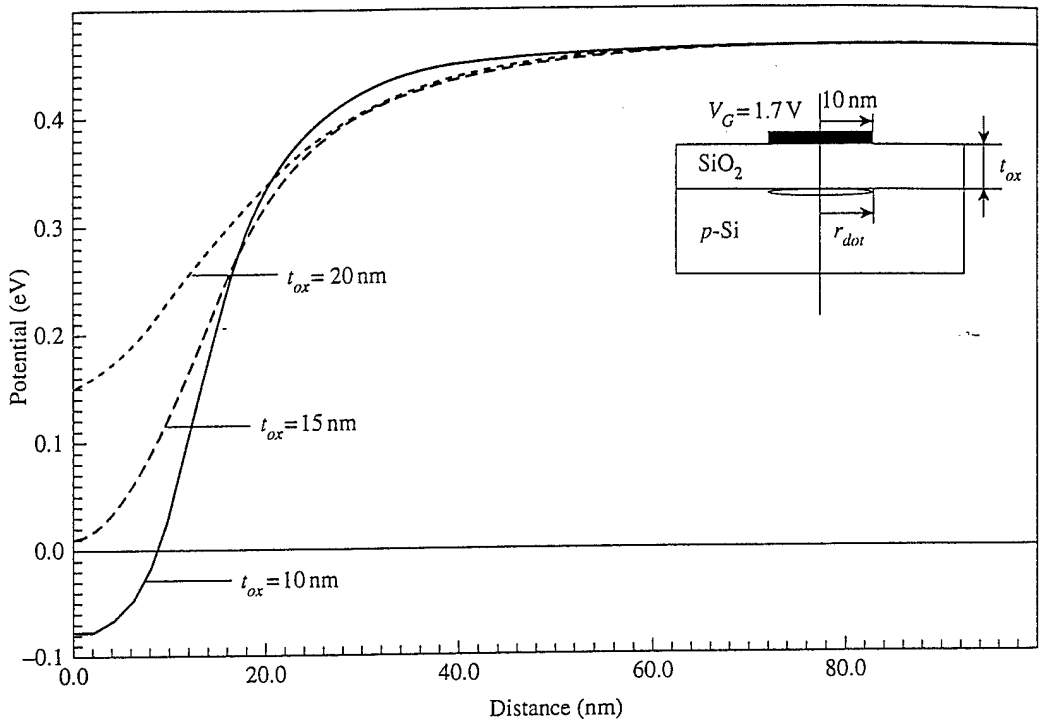

Fig. 5. Quantum dot potential profile along the Si/SiO_2 interface for various oxide thicknesses.

We have also performed numerical simulations for the design of gated few-electron quantum dot structures in the Si/SiO_2 material system. The motivation for this work is to investigate the feasibility of transferring the emerging technology of quantum dot fabrication from the III-V material system, where it was pioneered over the past few years, to the technologically more important Si/SiO_2 structures. Silicon appears to be a promising candidate due to the excellent insulating behavior of thin Si/SiO_2 films which yields the required crisp gate-control of the potential in the plane of the 2DEG at the Si/SiO_2 interface. Another advantage of silicon for quantum dot applications appears to be the higher effective mass, as compared to the III-V materials, which reduces the sensitivity of the energy levels to size fluctuations.

Quantum dots may be realized by applying a positive bias to a metallic gate on the surface, as schematically shown in the inset to Fig. 5. The positive voltage induces an inversion layer underneath the biased gate, which may lead to the formation of an 'electron droplet' at the silicon/oxide interface, i.e. a quantum dot. Figure 5 shows, for an applied gate bias of 1.7 V, the corresponding potential variations along the Si/SiO_2 interface; the Fermi energy is taken as the zero of energy and indicated by the thin horizontal line. An electronic system is induced when the silicon conduction band edge at the oxide interface, indicated by the solid line, dips below the Fermi level. We see that the formation of a quantum dot critically depends upon the thickness of the oxide layer. Our modeling shows that for a 10 nm gate radius, an oxide thickness around (or below) 10 nm is required.

Figure 6A shows, for various oxide thicknesses, the radius of a bias-induced quantum dot, as schematically shown in the inset. The positive bias is applied to a circular gate with 10 nm radius. Figure 6B presents the corresponding number of electrons in the quantum dot, which is obtained by integrating the electron density over the inversion region. The data shows that it should be feasible to create electronic systems with

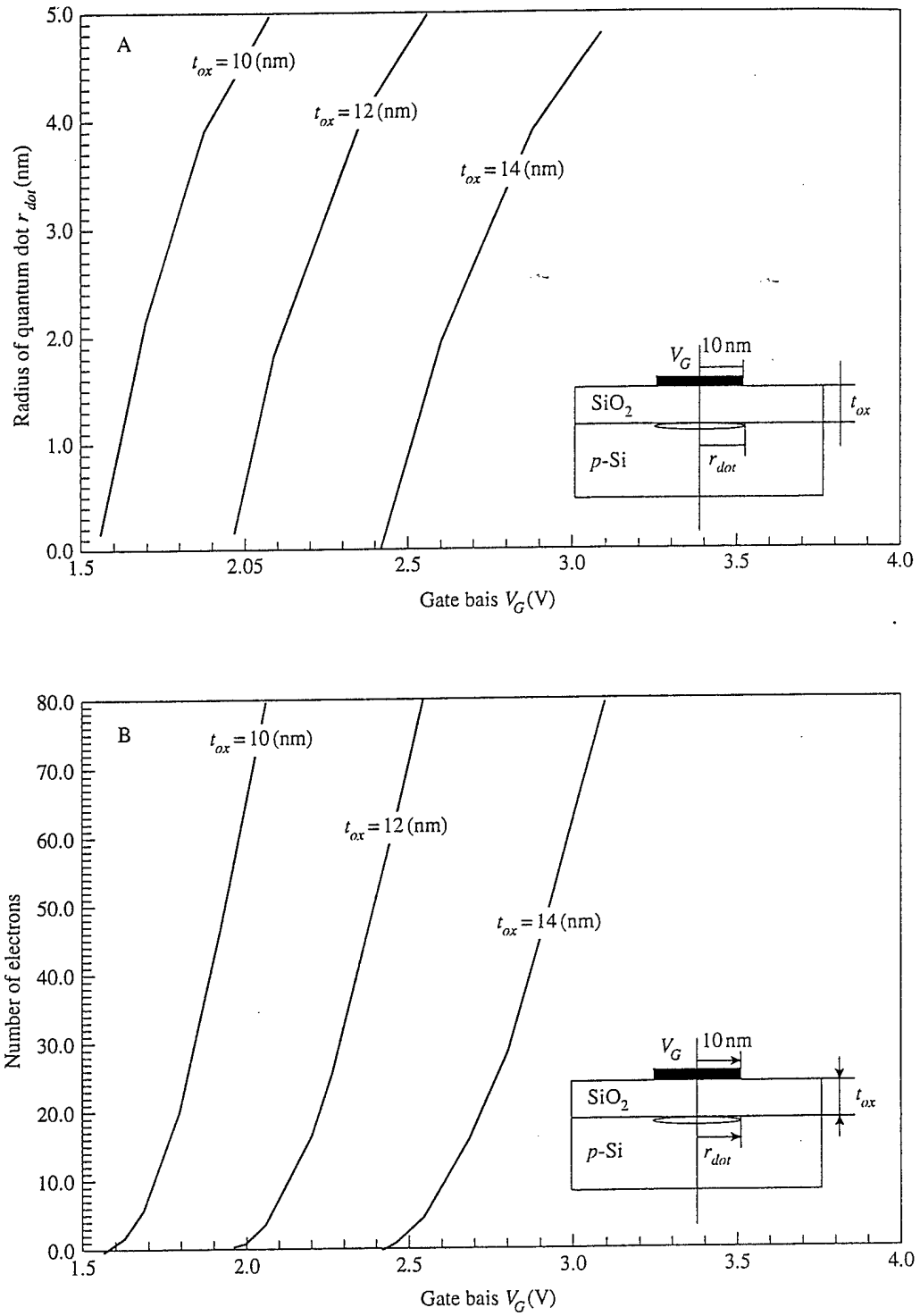

Fig. 6. Gate-induced quantum dot for various oxide thicknesses; shown are, as a function of gate bias, (A) the dot radius, and (B) the number of electrons occupying the dot.

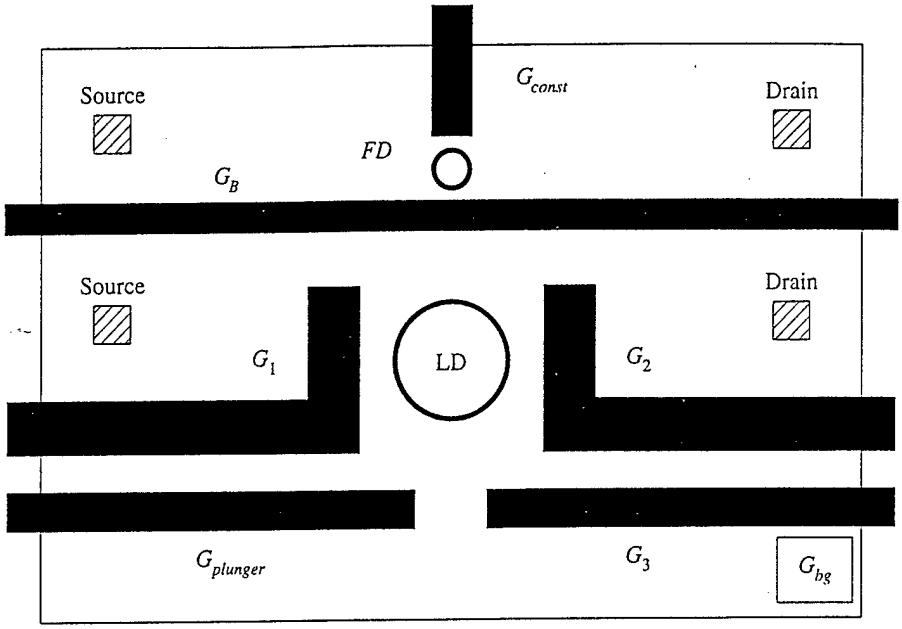

Fig. 7. Schematic diagram of gates and dots used in charge coupling and electrometer experiments.

dimensions on the order of 10 nanometers, and that it should be possible to control the electron occupancy in the few-electron regime.

5. Coupled dot experiments

Dot coupling is the most critical phenomenon required of QCAs, affecting intracellular and intercellular responses to inputs, and providing for an efficient method of charge detection, as we will demonstrate below. Our coupled dot experiments were performed on 2DEG material consisting of a 15 nm undoped AlGaAs spacer layer, a 30 nm n^+-AlGaAs Si-doped donor layer, and a 20 nm n^+-GaAs cap layer, resulting in 2DEG depth of 65 nm. The 2DEG carrier concentration and mobility at 4.2 K were 3×10^{11} cm^{-2} and 4.5×10^5 cm^2 V^{-1} s^{-1}, respectively. Ohmic contacts were formed from AuGeNi, and gates were defined by electron beam lithography (EBL). The cap layer was etched to minimize leakage current. The AuPd gate pattern was produced by EBL, thermal evaporation, and lift-off.

The gate pattern shown in Fig. 7 forms a 1D constriction adjacent to a lithographically defined dot. The lithographic dot (LD) has a total area of 490 $\times$ 360 nm^2 when negative gate voltages are applied to corresponding gates G_B, G_1, G_2, G_3, $G_{plunger}$. The constrictions between G_b–G_1 and G_b–G_2 form tunneling barriers through which the dot is weakly coupled to the source and drain. A back-gate contact was fabricated for further control of carrier concentration. All experiments were performed in a ^{3}He system with base temperature of 300 mK. Conductance was measured using standard lock-in techniques with a 10 μV excitation voltage at 10–20 Hz. The constriction and dot circuits were measured with separate lock-in amplifiers at different frequencies.

The population of the lithographic dot can be changed by varying any of the top or back gate potentials. At low temperatures (< 0.6 K) Coulomb blockade oscillations (CBO) with a distinct frequency were observed as a function of the plunger gate voltage, $V_{plunger}$ (Fig. 8A).

For certain settings of $V_{constriction}$, we also observed conductance resonances as a function of $V_{plunger}$ in

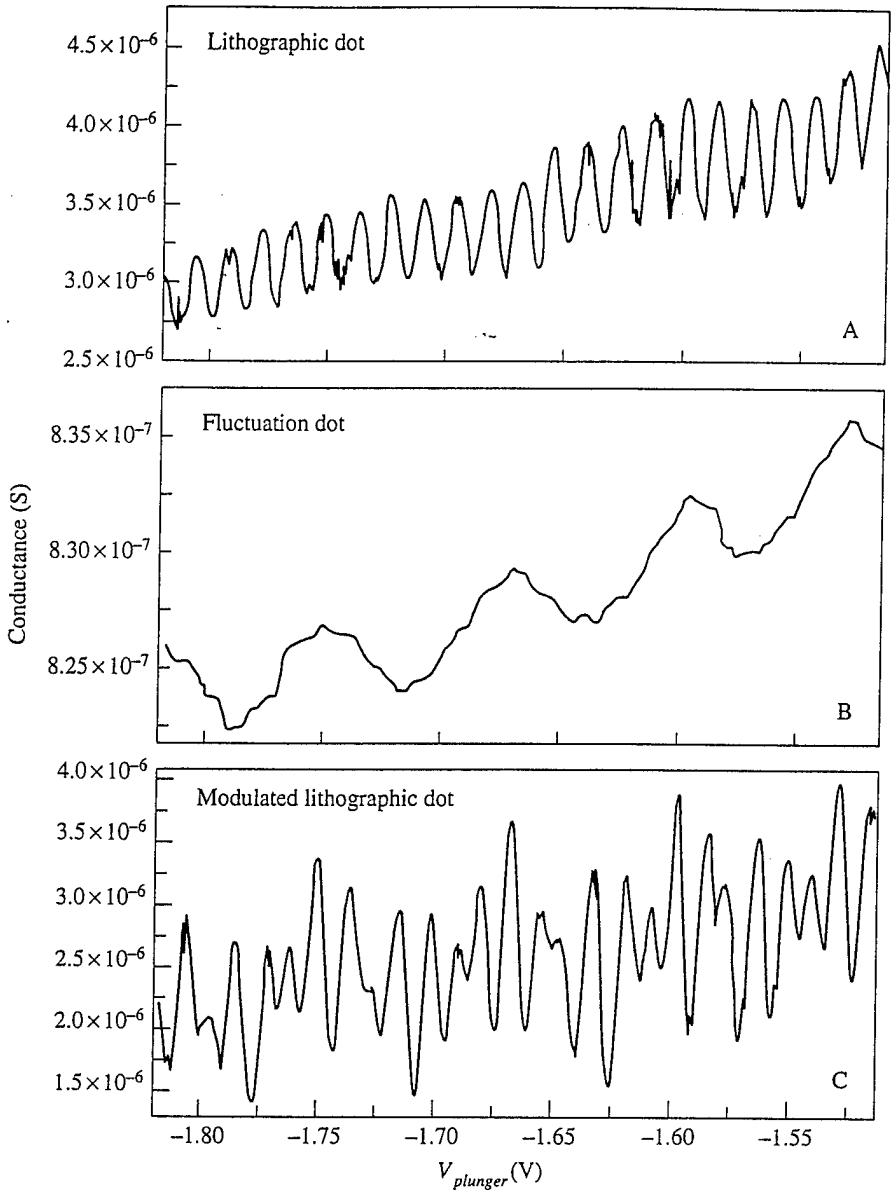

Fig. 8. Single electron tunneling conductance oscillations as a function of plunger gate voltage for (A) lithographic dot in the absence of fluctuation dot charging, (B) fluctuation dot, and (C) lithographic dot in the presence of fluctuation dot charging.

the narrow constriction adjacent to LD, shown in Fig. 8B. We believe these conductance oscillations were due to the depopulation of charge trapped by a random fluctuation potential in the narrow constriction. Such 'fluctuation dots' (FD) have been studied previously in several different systems [18–21], and conductance oscillations were interpreted in terms of Coulomb blockade transport through a quantum dot formed by fluctuation potentials. A post-measurement examination by field emission scanning electron microscopy revealed small ($\sim$ 20 nm) islands of n^+ GaAs on the surface, which may be the source of the fluctuation potential seen by electrons at the AlGaAs/GaAs interface.

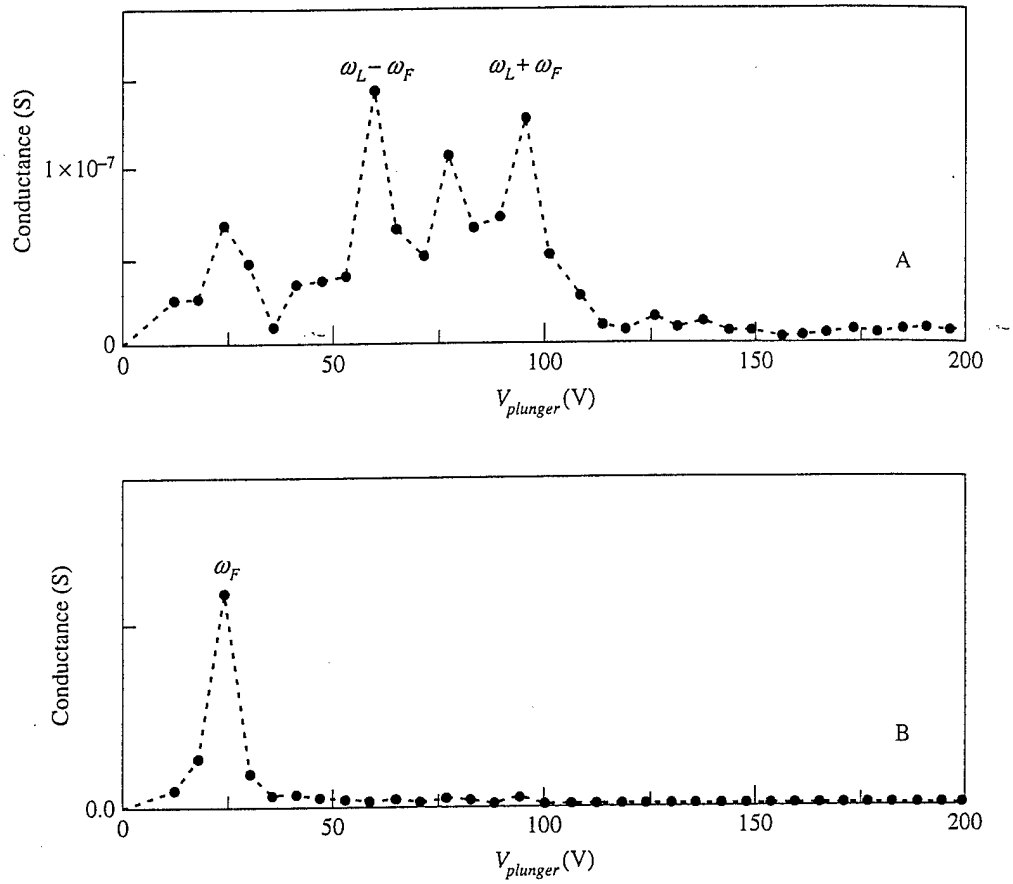

Fig. 9. Fourier transform spectra of conductance oscillations for (A) lithographic dot in the presence of fluctuation dot charging and (B) fluctuation dot charging.

The resistance of the barrier between the 1D constriction and the dot was determined to be greater than 100 GΩ, guaranteeing that the dot in the 1D constriction and the lithographic dot were not directly coupled. With proper bias settings, LD CBOs changed dramatically when FD CBOs were measured, as shown in Fig. 8C, with the Fourier transform (FFT) spectrum shown in Fig. 9A. The presence of $\omega_L + \omega_F$ and $\omega_L - \omega_F$ components are clearly seen. Almost no trace of the LD signal is seen in the FD FFT spectrum (Fig. 9B). In addition, sweeping the back-gate contact resulted in similar behavior of the two dots. The current through LD exhibited periodic oscillations as a function of external charge when no other charge was present. The periodicity of the LD oscillations was modified by the charging of the FD.

Our system is comparable to the metal tunnel junction system discussed by Lafarge *et al.* [22], with an equivalent circuit shown in Fig. 10. The plunger affects the population of both LD and FD. As the population of FD changes, it in turn modulates the population of LD. Assuming FD is smaller than LD, as expected from lithographic constraints, the behavior can be explained in terms of the relative charging energies of the dots. Since FD possesses less total capacitance, its charging energy is larger than that of LD, and its conductance oscillations occur with a larger period in $V_{plunger}$. Although the coupling capacitor C_c connects the dots, a change in the occupancy of FD by one electron results in a larger potential shift than for a similar change in occupancy of LD. Therefore, feedback of LD, acting now as an electrometer sensing the charge of FD, is

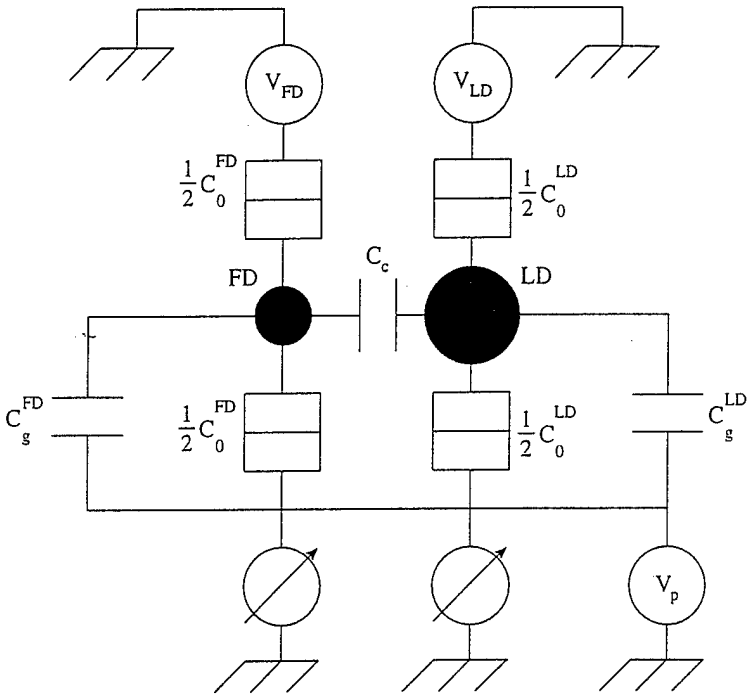

Fig. 10. Equivalent circuit of the lithographic and fluctuation dot configuration.

minimized since FD requires a larger contribution to its potential by LD in order to change its charge state. However, because LD is relatively large, its charging energy is small and changes in the potential of FD create a noticeable effect on its charge state.

Figure 11 shows the results of our model using the equivalent circuit of Fig. 10, and our experimentally-derived capacitance values. Parts (A) and (B) show LD junction charge and dot population as functions of $V_{plunger}$, with and without the presence of FD. Figure 11(C) and (D) show the same information for FD. It is clear that the additional potential from FD causes the positions of the population transitions of LD to shift relative to their positions without FD. Since the conductance peaks occur at population transitions, these shifts produce a clear modulation in the period of the conductance oscillations.

6. Summary and conclusions

We have discussed several practical issues in the study of theoretical and experimental QCA behavior. We have shown that adiabatic switching of QCAs is preferable to abrupt switching, and that double-gated structures are preferable to single-gated ones, resulting in very good control of dot size and occupancy. We have also demonstrated charge coupling between two quantum dots, and their behavior as a sensitive electrometer for the detection of single electron charging. The data was easily interpreted in terms of an equivalent circuit with a coupling capacitor between the two dots. These data indicate that a useful way of detecting the charge state of a QCA cell will be through the use of larger quantum dots as detectors of smaller dots. We have demonstrated repeatable lithographic dots of various sizes, and designed and fabricated six-dot cells guided by the results discussed here. The six-dot design incorporates four dots connected by tunnel junctions, forming the QCA cell, and two adjacent dots to be used as detectors, according to the results described in this paper. When an electron shifts between dots it is expected that the behavior of the non-invasive probe dots will be

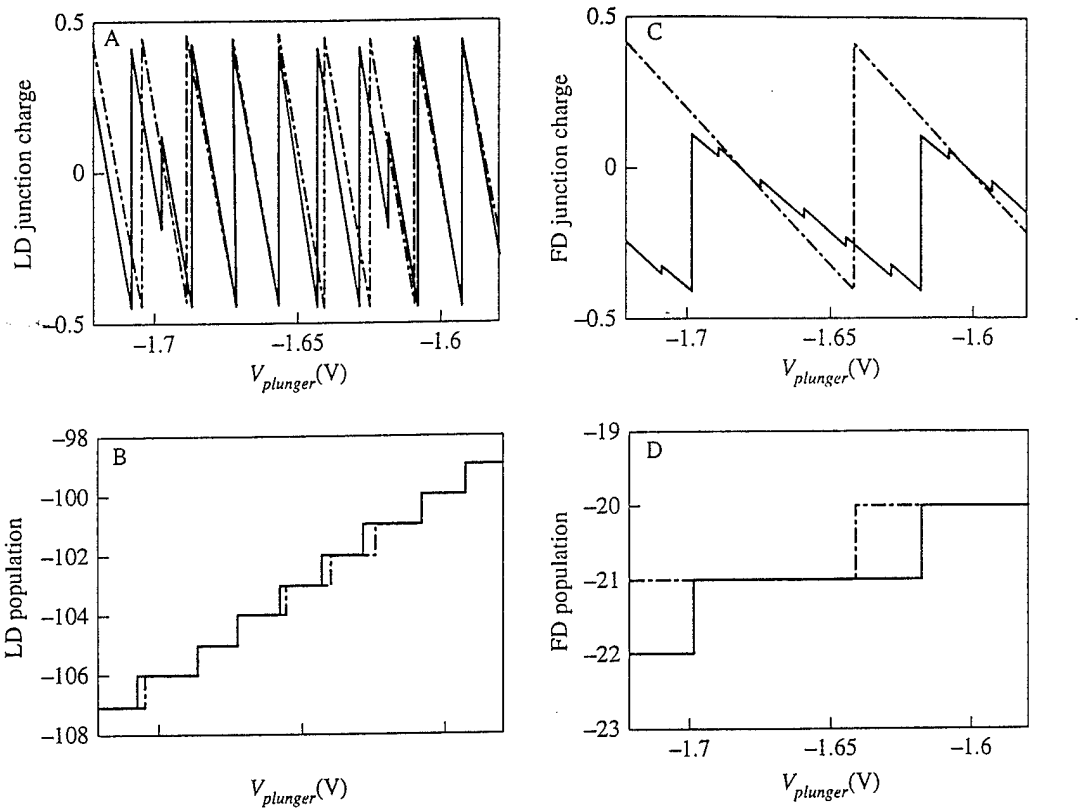

Fig. 11. Numerical simulation of the $V_{plunger}$ dependence, with dot coupling (——) and without dot coupling (— · —), of (A) LD junction charge, (B) LD electron population, (C) FD junction charge, and (D) FD electron population.

noticeably affected, thus providing us with information about the internal operation of the cell. The behavior of these cells is currently under investigation.

Acknowledgements—This work was supported by ARPA, NASA, and NSF.

References

[1] C. S. Lent, P. D. Tougaw, W. Porod and G. H. Bernstein, Nanotechnology **4**, 49 (1993).
[2] C. S. Lent, P. D. Tougaw and W. Porod, J. Appl. Phys. **74**, 3558 (1993).
[3] P. D. Tougaw and C. S. Lent, J. Appl. Phys. **75**, 1818 (1994).
[4] T. Fountain, unpublished.
[5] D. V. Averin and K. K. Likharev, in *Mesoscopic Phenomena in Solids* Edited by B. L. Altshuler, P. A. Lee and R. A. Webb, Elsevier, Amsterdam: p. 173 (1991).
[6] M. G. Ancona, J. Appl. Phys. **79**, 526 (1996).
[7] K. Nomoto, R. Ugajin, T. Suzuki and I. Hase, J. Appl. Phys. **79**, 291 (1996).
[8] T. A. Fulton and G. J. Dolan, Phys. Rev. Lett. **59**, 109 (1987).
[9] C. S. Lent and P. D. Tougaw, J. Appl. Phys. **75**, 4077 (1994).
[10] D. Leonard, M. Krishnamurthy, C. M. Reaves, S. P. Denbaars and P. M. Petroff, Appl. Phys. Lett. **63**, 3203 (1993).

[11] M. Field, C. G. Smith, M. Pepper, D. A. Ritchie, J. E. F. Frost, G. Z. C. Jones and D. G. Hasko, Phys. Rev. Lett. **70**, 1311 (1993).
[12] L. W. Molenkamp, K. Flensberg and M. Kemerink, Phys. Rev. Lett. **75**, 4282 (1995).
[13] F. Hofmann, T. Heinzel, D. A. Wharam, J. P. Kotthaus, G. Bohm, W. Klein, G. Trankle and G. Weimann, Phys. Rev. **B 51**, 13872 (1995).
[14] G. L. Snider, M. S. Miller, M. J. Rooks and E. L. Hu, Appl. Phys. Lett. **59**, 2727 (1991).
[15] G. L. Snider, I.-H. Tan and E. L. Hu, J. Appl. Phys. **68**, 5922 (1990).
[16] M. Chen, W. Porod and D. J. Kirkner, J. Appl. Phys. **75**, 2545 (1994).
[17] M. Chen and W. Porod, J. Appl. Phys. **78**, 1050 (1995).
[18] J. H. F. Scott-Thomas, S. B. Field, M. A. Kastner, H. I. Smith and D. A. Antoniadis, Phys. Rev. Lett. **62**, 583 (1990).
[19] A. A. M. Staring, H. van Houten, C. W. J. Beenakker and C. T. Foxon, Phys. Rev. **B 45**, 9222 (1992).
[20] J. Weis, R. J. Haug, K. v. Klitzing and K. Ploog, Phys. Rev. **B 46**, 12837 (1992).
[21] V. Chandrasekhar, Z. Ovadyahu and R. A. Webb, Phys. Rev. Lett. **67**, 2862 (1991).
[22] P. Lafarge, H. Pothier, D. Esteve, C. Urbina and M. H. Devoret, Z. Phys. **B 85**, 327 (1991).

External charge state detection of a double-dot system

Islamshah Amlani,[a] Alexei O. Orlov, Gregory L. Snider, Craig S. Lent, and Gary H. Bernstein
Department of Electrical Engineering, University of Notre Dame, Notre Dame, Indiana 46556

(Received 30 May 1997; accepted for publication 25 July 1997)

We report direct measurements of the charging diagram of a nanoscale series double-dot system at low temperatures. Our device consists of two metal dots in series, with each dot capacitively coupled to another single dot serving as an electrometer. This configuration allows us to externally detect all possible charge transitions within a double-dot system. In particular, we show that transfer of an electron between two dots, representing a polarization switch of the double dot, can be most prominently detected by our differential sensing scheme. We also perform theoretical calculations of the device characteristics and find excellent agreement with experiment. We discuss possible applications as an output stage for quantum-dot cellular automata architecture. © *1997 American Institute of Physics.* [S0003-6951(97)00738-9]

Recently, there has been a growing interest in coupled mesoscopic structures utilizing the Coulomb blockade (CB) phenomenon for their possible applications as electronic devices.[1–6] Various investigators have pointed out that coupled dots in the CB regime can perform useful computing functions.[7–13] A revolutionary computational paradigm, known as quantum-dot cellular automata (QCA), depends on the ability to control and detect the position of single electrons in an array of coupled dots to perform digital computation.[8–11] The basic building block of QCA is a four dot cell shown in Fig. 1. A QCA cell can be constructed of two series-connected dots separated by tunneling barriers and capacitively coupled to a second, identical double dot. If the capacitances are sufficiently small, charge is quantized on the dots.[1]

If the cell is biased such that there are two excess electrons within the four dots (one excess electron per double dot), these electrons will be forced to opposite "corners" of the four-dot system by Coulomb repulsion. The two possible electron configurations, i.e., the polarization states of the system, represent logic "0" and "1," as depicted in Fig. 1. Properly arranged, arrays of these basic cells can perform Boolean logic functions.

Critical to the implementation of QCA is a means of detecting the positions of individual electrons in the output cells. It has been shown[14,15] that a metal dot can be used to detect charge variation in another nearby dot. In previous double-dot experiments, the Coulomb interaction of electrons within two-dot systems is inferred exclusively from their charging diagrams.[4–6] A detection scheme that can probe the polarization state of the double dot externally, and with high sensitivity, has not heretofore been reported.

We present direct measurement of the internal charge state of a double-dot system. Specifically, we show that our charge detection technique is sensitive not only to the charge variation of individual dots but also to the more subtle exchange of one electron between the two dots. Our experimental results exhibit excellent agreement with theory. By showing that switching of an electron within a double dot can be externally detected, we demonstrate that our detection scheme is suitable for sensing the polarization state of a QCA cell.

Figure 2 shows a schematic diagram of our experiment. The device under study consists of four Al islands referred to as dots D_1, D_2, D_3, and D_4, respectively. Dots D_1 and D_2 are connected by a tunnel junction and are capacitively coupled to dots D_3 and D_4 which serve as electrometers. Dots D_1 and D_2 are also capacitively coupled to control gates A and B, respectively, to change the electron populations of their respective dots. In the experiment, we use control gates to shift an electron from D_1 to D_2 or vice versa, mimicking a QCA transition, and measure the conductances of D_3 and D_4 simultaneously as a function of bias on the control gates.

Fabrication of $Al/AlO_x/Al$ tunnel junctions is accomplished using standard electron beam lithography procedure and double angle shadow evaporation of Al.[16] The bottom electrode metal, 25 nm thick, is oxidized *in situ*, followed by 50 nm of Al to form the top electrode. The two islands, labeled D_1 and D_2 in Fig. 1, between the three (60×60 nm^2) tunnel junctions are 1.4 μm long, and the lengths of islands D_3 and D_4 are 1.1 μm each.

The sample is mounted on the cold finger of a dilution refrigerator with a base temperature of 25 mK. Conductances of the double dot and each electrometer are measured simultaneously using standard ac lock-in techniques with an excitation voltage of 4 μV at 16–40 Hz. A magnetic field of 1 T is applied to suppress the superconductivity of Al. The typical tunnel resistance of a junction, based on I–V measurements of the electrometers at 1 K, is approximately 200 kΩ. The total capacitance of the electrometer dots, C_Σ, extracted from the charging energy ($E_C \sim 80$ μeV), is approximately 1 fF. Various lithographic and parasitic capacitances between different gates and islands are determined from the period of

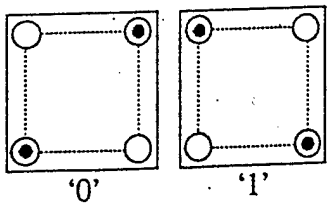

FIG. 1. QCA cell showing the two possible polarizations.

[a]Electronic mail: Islamshah.amlani.1@nd.edu

 0003-6951/97/71(12)/1730/3/$10.00

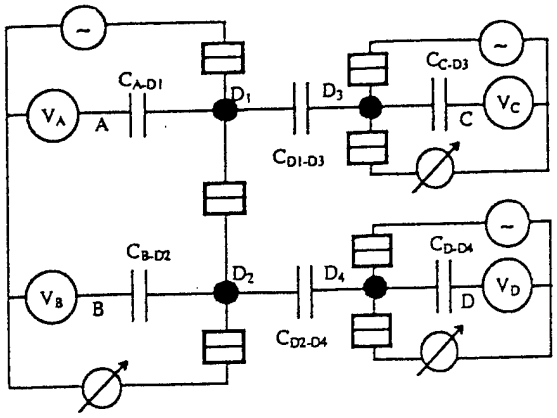

FIG. 2. Schematic diagram of the device structure. The circuit used to compensate for parasitic capacitance between the driver gates A/B and the electrometer islands D_3/D_4 is not shown.

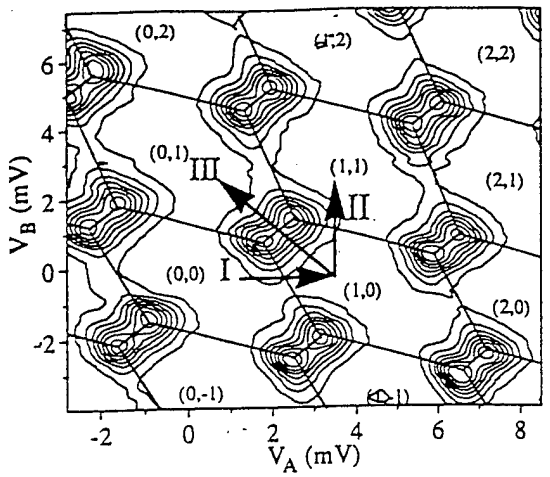

FIG. 3. Charging diagram of the double dot as a function of the gate voltages V_A and V_B. Charge configurations (n_1 and n_2), which represent the number of extra electrons on D_1 and D_2, respectively, are arbitrarily chosen. Lines labeled I, II, and III show a few directions in which charge can shift between different configurations of the double dot.

the Coulomb blockade oscillations (CBO).[1] The double dot structure is used as a gate electrode to measure the capacitance of the coupling capacitors $C_{D_1-D_3}$ and $C_{D_2-D_4}$.

In our experiments, the charge on the double-dot structure is varied by sweeping gates A and B. Conductances through the double dot and both electrometers are measured simultaneously as a function of the control gate voltages. To prevent these voltages from affecting the electrometers due to parasitic capacitance, we apply cancellation voltages, with polarities opposite to V_A and V_B, to gates C and D. Using this charge compensation technique, we can observe up to 100 periods in the electrometer conductances due to discrete variations of the coupled island charges, without inducing extra charge on the electrometers due to the control gates. The operating points of the electrometers are set to be equal to each other on a rising edge of their current versus island charge characteristics to ensure an identical response from each one. We have designed coupling capacitors $C_{D_1-D_3}$ and $C_{D_2-D_4}$ to be relatively large in order to make the electrometers sensitive to small charge variations on the double dot, yet our measurement process is noninvasive since the coupling capacitors constitute only 10% of C_Σ.[15]

The motion of electrons within the double dot can best be understood from its charging diagram. A contour plot of conductance through the double-dot, $G_{\text{double dot}}(V_A, V_B)$, is shown in Fig. 3. The peaks in conductance at triple points, depicted by a convergence of contour lines, form a hexagonal "honeycomb" observed by Pothier *et al.*[5] Each hexagonal cell is delineated by solid lines surrounding regions where a particular configuration (n_1, n_2) is the ground state, with n_1 and n_2 representing the number of excess electrons on dots D_1 and D_2, respectively. In the interior of the cell, there is no charge transport through the double dot due to the Coulomb blockade of electrons. Under the influence of control gates, the charge configuration of the double dot can be varied by crossing honeycomb borders along any of the three directions shown in Fig. 2. This does not result in significant current flow through the double dot if the path chosen avoids triple points. Along directions I and II, charge is added to only one of the dots in units of single electrons, while the population of the other dot stays constant. Charge redistribution in the double dot takes place along direction III when electrons transfer from one dot to the other while maintaining the total charge on the double-dot constant.

Figure 4(a) shows a small section of the double-dot charging diagram, along with plots of the conductance through the electrometers D_3, G_{D_3}, and D_4, G_{D_4}, shown in Figs. 4(b) and 4(c), respectively. Lighter areas in these gray scale contour plots represent higher conductance. To demonstrate that a replica of the double-dot charging diagram can be traced in the electrometer signals, we superimpose the honeycomb boundaries from Fig. 4(a) onto Figs. 4(b) and 4(c). The change in the conductance of each electrometer reflects the variation of the electrostatic potential in the dot capacitively coupled to it. A sharp change in the conductance

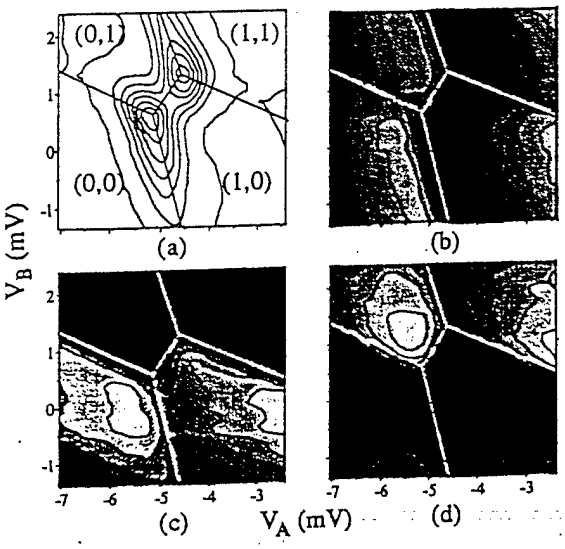

FIG. 4. (a) Smaller section of the double dot charging diagram as a function of gate voltages V_A and V_B. (b) and (c) Conductances of the electrometers D_3 and D_4, respectively, with the honeycomb boundaries of Fig. 4(a) superimposed. Sharp transitions in the horizontal direction in (b) indicate a change in the population of D_1. Sharp transitions in the vertical direction in (c) reflect a change in the population of D_2. (d) Differential signal obtained from the conductances of the individual electrometers.

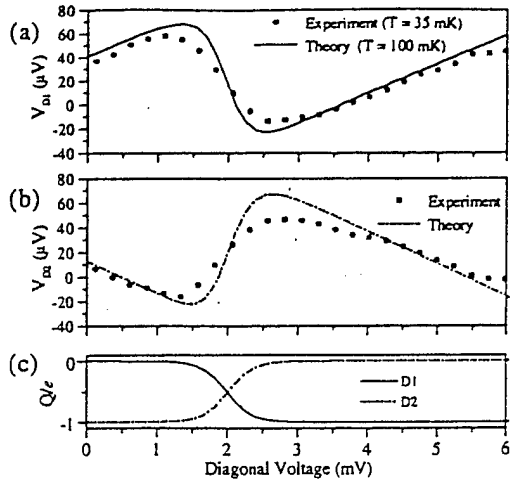

FIG. 5. (a) and (b) Experimental and theoretical curves showing potential changes in dots D_1 and D_2, respectively, during charge redistribution in the double dot. The solid line represents the simulation result at 100 mK, and the dotted line shows the experimental values calculated from the conductances of D_3 and D_4. (c) Theoretical calculations of the charges on dots D_1 and D_2 during charge redistribution.

of D_3 (from light to dark) in the horizontal direction [Fig. 4(b)] represents addition of an electron to D_1. Similarly, sharp variation in conductance of D_4 in the vertical direction [Fig. 4(c)] indicates discrete variation of charge on D_2. Hence, the sharpest variations in the conductances of each electrometer reveal the charging of their capacitively coupled dots.

Sensing the state of a QCA cell requires detection of the polarization change in the double dot shown by direction III in the charging diagram of Fig. 2. In Figs. 4(b) and 4(c), we see that the transitions along this direction are detected less strongly in the electrometer signals. This is due to the cross capacitance between dots $D_1(D_2)$ and $D_4(D_3)$ which makes each electrometer sensitive to both dots. According to our measurements, the sensitivity of the electrometers to the remote dots is about 30% of that to the nearby dots. During charge redistribution in the double dot, the signals from the two electrometers are out of phase by 180° and each reflects the superposition of the two signals. As a result, the detected signal is about 30% weaker than that along direction I (II) in the conductance of $D_3(D_4)$. To show the polarization change of the double dot more prominently, we use the differential signal from the two electrometers, $G_{D_3}-G_{D_4}$, as shown in Fig. 4(d). The most conspicuous transition, represented by a higher density of contour lines, occurs at the boundary between the (0,1) and (1,0) states, indicating an electron shift from one dot to the other. As mentioned above, this is due to the phase difference (180°) in the signals of the individual electrometers, yielding a differential signal which is approximately twice as strong as the one detected by a single electrometer.

We compare the measured potential changes on dots D_1 and D_2 during the charge redistribution in the double dot (direction III in Fig. 3) with theoretical results, which include the experimentally determined capacitance parameters. Figures 5(a) and 5(b) show the experimental and theoretical plots of the potentials on dots D_1 and D_2, respectively, as a function of the "diagonal voltage," where $\Delta V_A=-\Delta V_B$. As expected, the potentials on the two dots change linearly, maintaining a phase difference of 180° with an abrupt shift when the electron populations of the dot change. To confirm that the observed potential change of the two dots is caused by a polarization switch in the double dot, we also show calculated charges on the dots in Fig. 5(c). The theoretical results are obtained by minimizing the classical electrostatic energy for the array of islands and voltage leads. The full capacitance matrix is included, and the minimum energy charge configuration is calculated subject to the condition that island charge be an integer multiple of electronic charge. Finite temperature effects are obtained by performing the thermodynamic averaging over all nearby charge configurations. The experiment matches theory very well with only the substrate background charge and temperature as fitting parameters. The background charge adds an uncontrolled offset to the position of the peaks, but does not change the magnitude or period of the dot potentials. The best fit to experiment is obtained for a temperature of 100 mK. The discrepancy between this and the temperature of the experiment (35 mK) is most likely due to heating of the electron subsystem by the applied 4 μV excitation and insufficient filtering of the leads.

In summary, we have presented direct measurement of the internal state of a coupled dot system by externally detecting all possible charge transitions of a single electron. A polarization change of the double dot is most prominently seen in the differential signal that utilizes the signals from both electrometers. As proposed by Lent *et al.*,[10] a complete implementation of quantum-dot cellular automata requires the detection of single electron motion between dots. With this investigation, we demonstrate that our differential detector can be used to confirm the operation of a QCA cell.

This research was supported in part by DARPA, ONR (Grant No. N0014-95-1-1166) and NSF. The authors wish to thank W. Porod and J. Merz for helpful discussions.

[1] D. V. Averin and K. K. Likharev, in *Mesoscopic Phenomena in Solids*, edited B. L. Altshuler, P. A. Lee, and R. A. Webb (North Holland, Amsterdam, 1991), Chap. 6.
[2] *Single Charge Tunneling*, edited by H. Grabert and M. H. Devoret (Plenum, New York, 1992).
[3] W. P. Kirk and M. A. Reed, *Nanostructures and Mesoscopic Systems* (Academic, Boston, 1992).
[4] F. R. Waugh, M. J. Berry, D. J. Mar, and R. M. Westervelt, Phys. Rev. Lett. 75, 705 (1995).
[5] H. Pothier, P. Lafarge, C. Urbina, D. Esteve, and M. H. Devoret, Europhys. Lett. 17, 249 (1992).
[6] T. Sakamoto, S. Hwang, F. Nihey, Y. Nakamura, and K. Nakamura, Jpn. J. Appl. Phys. 33, 4876 (1994).
[7] J. R. Tucker, J. Appl. Phys. 72, 4399 (1992).
[8] C. S. Lent, P. D. Tougaw, and W. Porod, Appl. Phys. Lett. 62, 714 (1993).
[9] P. D. Tougaw, C. S. Lent, and W. Porod, J. Appl. Phys. 74, 3558 (1993).
[10] C. S. Lent, P. D. Tougaw, W. Porod, and G. H. Bernstein, Nanotechnology 4, 49 (1993).
[11] C. S. Lent and P. D. Tougaw, J. Appl. Phys. 75, 4077 (1994).
[12] J. M. Martinis, M. Nahum, and H. D. Jensen, Phys. Rev. Lett. 72, 904 (1994).
[13] P. D. Dresselhaus, L. Ji, S. Han, J. E. Lukens, and K. K. Likharev, Phys. Rev. Lett. 72, 3226 (1994).
[14] P. Lafarge, H. Pothier, E. R. Williams, D. Esteve, C. Urbina, and M. H. Devoret, Z. Phys. B 85, 327 (1991).
[15] G. Bazan, A. O. Orlov, G. L. Snider, and G. H. Bernstein, J. Vac. Sci. Technol. B 14, 40 (1996).
[16] T. A. Fulton and G. H. Dolan, Phys. Rev. Lett. 58, 109 (1987).

Realization of a Functional Cell for Quantum-Dot Cellular Automata

A. O. Orlov, I. Amlani, G. H. Bernstein, C. S. Lent, G. L. Snider

This paper presents an experimental demonstration of a basic cell of the quantum-dot cellular automata, a transistorless approach to computation that addresses the issues of device density, interconnection, and power dissipation. The device under study was composed of four metal dots, connected with tunnel junctions and capacitors, and operated at <50 mK. Operation was evidenced by switching of a single electron between output dots controlled by a single electron switching in input dots, demonstrating a nonlinear, bistable response.

Achievement of ever higher levels of integration in microelectronics eventually will require a shift from the field-effect transistor (FET)–based paradigm. Scaling of FETs will be limited by unacceptable power dissipation and short-channel effects, which lead to performance degradation. One alternative architecture, quantum-dot cellular automata (QCA) (*1*), is a transistorless approach with quantum dots that addresses the issues of device density, interconnection, and power dissipation. Conventional digital architectures use transistors as current switches to charge and discharge capacitors to the required logic voltage levels. In QCA, logic states are encoded no longer as voltages but rather by the positions of individual electrons. QCA architecture is scalable to molecular levels, and performance actually improves as the size of the device is decreased. The cell presented here operates at cryogenic temperatures, but a molecular-sized QCA cell would function at room temperature.

On the basis of existing technology, a possible realization of a basic QCA cell would be composed of two series-connected metal dots separated by tunneling barriers and capacitively coupled to a second, identical double dot. The dots and associated capacitances are sufficiently small that the system is in the Coulomb blockade regime (*2*) at the temperature of the experiment. If the cell is biased so that there are two excess electrons within the four dots (one excess electron per double dot), those electrons are forced to opposite corners of the four-dot system by Coulomb repulsion. The two possible polarization states of the system represent logic 0 and 1, as indicated in Fig. 1A. Properly arranged, arrays of these basic cells can implement Boolean logic functions (*3*).

We report the experimental demonstration of a functioning QCA cell. Direct measurements of the charging diagram of output dots under the influence of electron switching in input dots, combined with electrometer measurements of output dots, show a controlled polarization change of a QCA cell. Our experimental results show excellent agreement with theory.

The device consists of four Al islands, with input dots D1 and D2 and output dots D3 and D4 (Fig. 1B). The Al-AlO_x-Al tunnel junctions were fabricated on an oxidized Si substrate by a standard electron beam–lithography and shadow evaporation technique (*4*). The area of the junctions is about 60 by 60 nm. The sample was mounted on the cold finger of a dilution refrigerator with a base temperature of 15 mK. Conductances of the double dot and each input dot were measured simultaneously by standard ac lock-in techniques with an excitation voltage of 4 μV at 16 to 40 Hz. A magnetic field of 1 T was applied to suppress the superconductivity of the metal. Typical resistance of a single junction at 1 K was 200 kilohm. Capacitances between gates and islands were determined from the period of the Coulomb blockade oscillations, and values of junction capacitances were extracted from current-voltage measurements (*2*).

A polarization change of the QCA cell requires an electron transfer between dots within each double dot. Gate electrodes force an electron to switch from one dot to the other within the input set of dots, which in turn induces a switch of the other electron in the output dots. This process can best be understood by considering the motion of electrons within one double dot. By measuring the conductance through the double dot as a function of the gate voltages V_C and V_D (Fig. 1C), we can determine the electron charge configuration within the double dot. Current can flow through a double dot only at certain settings of the gate voltages, where the Coulomb blockade is lifted for both dots simultaneously. A contour plot of the measured conductance through a double dot as a function of gate voltages V_C and V_D (Fig. 1D) shows peaks in conductance at triple points, T, which form a hexagonal "honeycomb" (*5*). Each hexagonal cell is delineated by dashed lines in Fig. 1D,

Department of Electrical Engineering, University of Notre Dame, Notre Dame, IN 46556, USA.

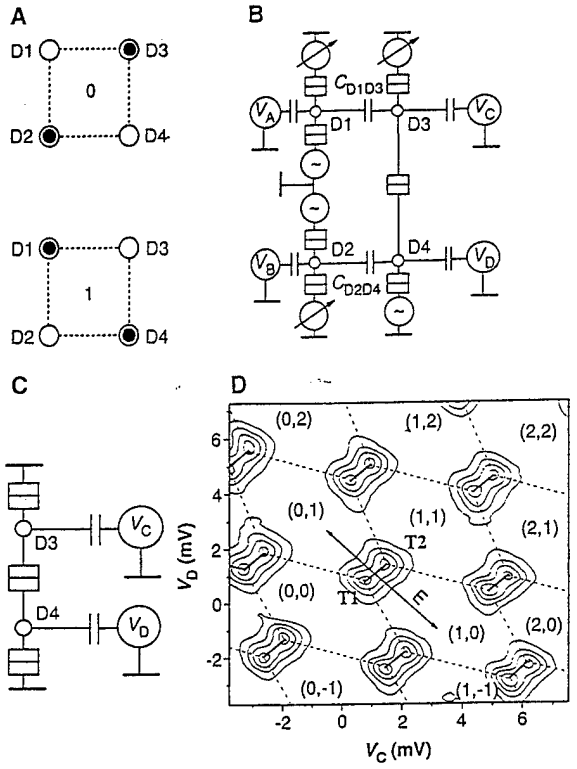

Fig. 1. (**A**) QCA cell showing two possible polarizations. (**B**) Schematic diagram of the experiment. (**C**) Double-dot system with two metal islands connected by a tunnel junction. V_C and V_D are gate voltages controlling the charge on dots D3 and D4. (**D**) Contour plot of measured conductance through the double dot as a function of gate voltages V_C and V_D, where (n_3, n_4) is the number of excess electrons on dots D3 and D4.

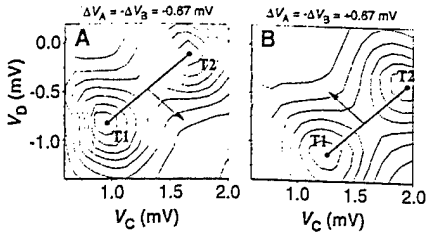

Fig. 2. Charging diagram of output double dot with $\Delta V_A = -\Delta V_B = -0.67$ mV (**A**) and $\Delta V_A = -\Delta V_B = +0.67$ mV (**B**). These values correspond to the maximum shift of the honeycomb (Fig. 1D) induced by an electron transfer in input dots. Arrows show the direction of honeycomb motion.

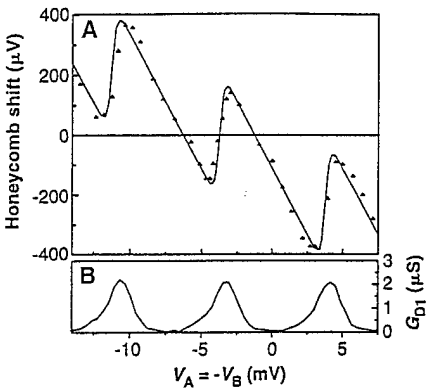

Fig. 3. (**A**) Experimental (▲) and theoretical (—) honeycomb shift as a function of driver voltages $V_A = -V_B$. Electron exchange occurs when the border crosses zero. Theory uses a temperature of 50 mK. (**B**) Conductance through input dot D1 as a function of driver voltage.

marking a region where a particular configuration (n_3, n_4) is the ground state, with n_3 and n_4 representing the number of excess electrons on islands D3 and D4, respectively. A switch of an electron between the two dots occurs along direction E, whereas total charge on the double dot remains constant along that direction.

To accomplish a polarization switch of a QCA cell, an electron transfer between the input dots must produce an opposite transfer of an electron between the output dots. The gate biases for the double dot set the working point V_C^0, V_D^0 to the center of the transition border (T1–T2) in the absence of an input signal. The cell is then in its most symmetrical state, and in the absence of an input signal the two polarizations are equally probable. An input "push-pull" signal ($+\Delta V_A = -\Delta V_B$) added to the driver gates polarizes the input dots, which in turn polarizes the output double dot. A polarization change in the output double dot corresponds to a movement of the entire honeycomb pattern along direction E relative to a fixed working point V_C^0, V_D^0. Electron switching in the output double dot takes place each time the border (T1–T2) crosses the working point. The ability to produce and detect a polarization switch of the output dots, induced by a single electron transfer in the input dots, demonstrates a functioning QCA cell.

In this experiment, we determined the charge state of the output double dot by measuring its conductance, which required a sweep of V_C and V_D. To prevent these voltages from affecting the input dots as a result of parasitic capacitance, we applied cancelation voltages, with polarities opposite to V_C and V_D, to gates A and B.

Although the input dots were not connected by a tunneling junction (Fig. 1B), by carefully controlling the charge on dots D1 and D2 we duplicated the behavior of the input double dot of a full four-dot QCA cell. We could not actually switch an electron between the input dots, but, by applying biases with opposite polarities to gates A and B, each time an electron was removed from one input dot, an electron was added to the other, mimicking an electron transfer in an input double dot. The advantages of having two separate dots as an input stage of a QCA cell are that each dot can be individually measured and the charge of each dot can be individually controlled. In this way, addition and removal of electrons in the input dots were easily synchronized during scan of the drivers.

As mentioned above, transfer of an electron between input dots produces a shift of the entire charging diagram of the output double dot along direction E. To observe this shift, "snapshots" of the conductance $G_{\text{double dot}}(V_C, V_D)$ were taken for different push-pull ($+\Delta V_A = -\Delta V_B$) settings on the drivers. The potential on a metal dot in the Coulomb blockade regime changes linearly as a function of gate voltage, with an abrupt shift when the electron population of the dot changes (6). Thus, the potentials on the input dots oscillate in a sawtooth pattern with driver voltage, resulting in sawtooth-like shifts of the honeycomb. We observed a slow shift of the border corresponding to a gradual increase of the potential on the input dots followed by an abrupt "reset." Two snapshots were taken at the extremes of the shift with an amplitude of ~370 μV (Fig. 2).

We measured the shift of the honeycomb border while sweeping gates A and B over a voltage that was sufficient for several electrons to transfer between the input dots. The measured border shift with respect to a fixed working point V_C^0, V_D^0 as a function of the driver voltage ($+V_A$ and $-V_B$) is shown in Fig. 3A. A periodic abrupt shift in the border position occurred each time an electron switched in the input dots [indicated by peaks in conductance through the input dots (Fig. 3B)], confirming that the shift was due to a single electron transfer. A parasitic cou-

pling from gates A and B to the output dots added a monotonic term to the border shift, but its magnitude was smaller than that of the periodic shift over the voltage range of one electron switch in the input dots.

We compared the observed border shift with theoretical results (Fig. 3A), which include cancelation voltages and all experimentally determined capacitances. The theoretical results were obtained by minimizing the classical electrostatic energy for the array of islands and voltage leads. The full-capacitance matrix was included, and the minimum energy charge configuration was calculated subject to the condition that island charge be an integer multiple of electronic charge. Finite temperature effects were obtained by thermodynamic averaging over all nearby charge configurations. Experiment and theory match very well with only the substrate background charge and temperature as fitting parameters. The background charge adds a random offset to the position of the border but does not change the magnitude or period of the observed shift. The best fit to experiment is obtained for a temperature of 50 mK. The discrepancy between this and the base temperature of the dilution refrigerator (15 mK) most likely occurs because of heating of the electron subsystem by electromagnetic and thermal noise sources (7) and the applied 4-μV excitation. This effect is common in transport experiments at temperatures below 100 mK (6, 7).

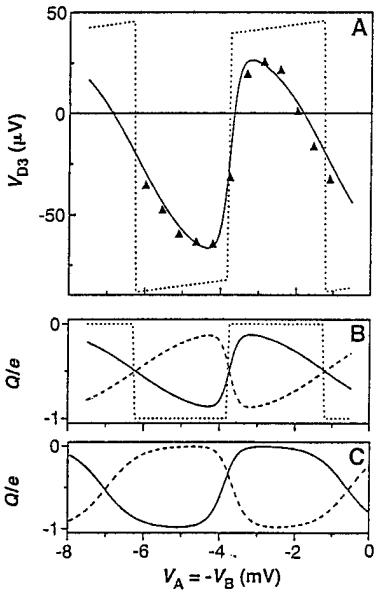

Fig. 4. (**A**) Voltage on dot D3 of output double dot as a function of driver voltage $V_A = -V_B$. Triangles are experimental data, and solid line represents theoretical values at 50 mK. For reference, theoretical data at 0 K (dotted line) are shown. (**B**) Calculated charge on dots D3 and D4 as a function of driver voltage for $C_{D1D2} = C_{D2D4} = 0.65$ e/mV (experimental value). Solid line represents charge on dot D3 at 50 mK, dashed line is charge on dot D4 at 50 mK, and dotted line is charge on D3 at 0 K. (**C**) Calculated charge on dots D3 and D4 as a function of driver voltage for $C_{D1D2} = C_{D2D4} = C_{junction} = 2.1$ e/mV. Solid line is charge on dot D3 at 50 mK, and dashed line is charge on dot D4 at 50 mK.

To show that the observed border shift represents a polarization switch of the cell at finite temperature, we combined the results of the border-shift measurements (Fig. 3) with measurements of the electrostatic potentials of the double dot. The electrostatic potential of each dot in the double dot was measured with the same device but with D1 and D2 as electrometers (8). The result is shown in Fig. 4A, where we plot electrostatic potential on dot D3 as measured by electrometer D1, together with theoretical calculations of the same potential at 0 and 50 mK, as a function of driver voltage V_A. The calculated excess charge on islands D3 and D4 of the double dot at 50 mK and, for reference, the charge on D3 at 0 K are indicated in Fig. 4B. Charge switching occurs at $V_A \sim -3.8$ mV, corresponding to an electron switch in the input dots. An input voltage swing $\Delta V_A = -\Delta V_B$ of 1.3 mV is sufficient for nearly complete transfer of an electron from one output dot to the other. An increase in coupling capacitance $C_{D1D3} = C_{D2D4}$ would lead to a more complete electron transfer, as shown in the theoretical plot (Fig. 4C), where we set the coupling capacitance to be equal to a junction capacitance. The data of Fig. 4 confirm that the experimentally observed honeycomb shift represents the polarization change of a functioning QCA cell.

The QCA architecture is a break from the FET-based paradigm of digital logic. Logic levels are encoded no longer as voltages on capacitors, which must be charged and discharged by current switches, but rather as the positions of electrons within a cell. The scalability of QCA offers the future possibility of functional devices that, at the molecular level, can operate at room temperature.

REFERENCES AND NOTES

1. C. S. Lent, P. D. Tougaw, W. Porod, G. H. Bernstein, *Nanotechnology* 4, 49 (1993); C. S. Lent and P. D. Tougaw, *Proc. IEEE*, 85, 541 (1997).
2. K. K. Likharev, *IBM J. Res. Dev.* (January 1988), p. 114.
3. P. D. Tougaw and C. S. Lent, *J. Appl. Phys.* 75, 1818 (1994).
4. T. A. Fulton and G. H. Dolan, *Phys. Rev. Lett.* 58, 109 (1987).
5. H. Pothier *et al.*, *Physica B* 169, 573 (1991).
6. P. Lafarge *et al.*, *Z. Phys. B* 85, 327 (1991).
7. D. Vion *et al.*, *J. Appl. Phys.* 77, 2519 (1995).
8. I. Amlani, A. O. Orlov, G. L. Snider, G. H. Bernstein, unpublished results.

9. Supported in part by Defense Advanced Research Project Agency, Office of Naval Research (grant N00014-95-1-1166), and NSF. We thank W. Porod and J. Merz for useful discussions.

15 May 1997; accepted 23 June 1997

VLSI DESIGN
1998, Vol. 8, Nos. (1–4), pp. 555–558
Reprints available directly from the publisher
Photocopying permitted by license only

Electrostatic Formation of Coupled Si/SiO_2 Quantum Dot Systems

PER HYLDGAARD*, HENRY K. HARBURY and WOLFGANG POROD

Department of Electrical Engineering, University of Notre Dame, Notre Dame, IN 46556

We present three-dimensional numerical modeling results for gated Si/SiO_2 quantum dot systems in the few-electron regime. In our simulations, the electrostatic confining potential results from the Poisson equation assuming a self-consistent Thomas-Fermi charge model. We find that a very thin SiO_2 top insulating layer allows an effective control with single-electron confinement in quantum dots with radius less than 10 nm and investigate the detailed potential and resulting charge densities. Our three-dimensional finite-element modeling tool allows future investigations of the charge coupling in gated few-electron quantum-dot cellular automata.

Keywords: 3D simulation and modeling, finite element method, silicon/silicon-dioxide quantum dots, quantum-dot cellular automata

We present numerical simulations for electrostatically confined few-electron quantum dot systems in the technologically important Si/SiO_2 material system. Our emphasis is modeling a possible so-called *Quantum-dot cellular automata* (QCA) structure [1] in which a bi-stable occupation by two excess electrons in a small and strongly charge-coupled quantum-dot system defines logic 0/1.

The *bottom panel* of Figure 1 shows a schematic of the Si/SiO_2 material system: a thin silicon-dioxide layer serves as excellent insulation of the bottom silicon slab from the set of top gates. Applying finite biases at these gates allows the formation of electrostatically confined quantum dots just below the heterostructure interface (at $z = z_0$). Mesoscopic transport investigations in gate-induced quantum-dot arrays [2] documents the feasibility of fabricating few-electron quantum-dot systems in the Si/SiO_2 material system. This development has in turn resulted in a proposal for room-temperature single-electron Si/SiO_2 memory cells [3].

Previous (two-dimensional) modeling results [4, 5] of few-electron Si/SiO_2 quantum dot systems exploited an axial symmetry to investigate the electrostatic confinement within an individual dot. Encouraged by recent three-dimensional modeling of larger quantum-dot systems [6] we investigate

*Corresponding author.

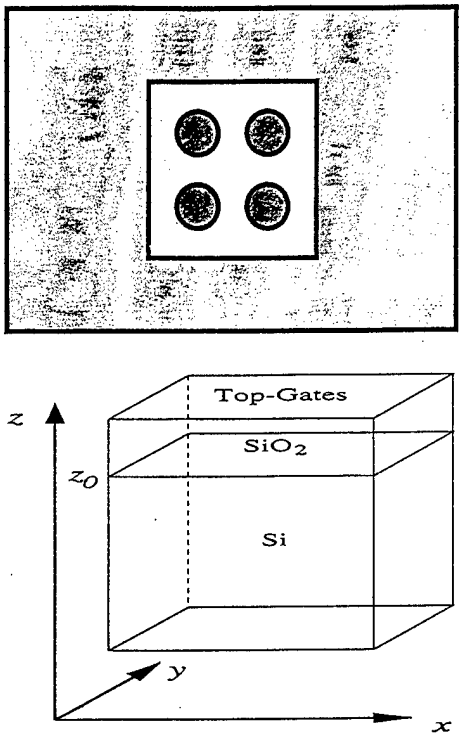

FIGURE 1 Schematics of possible gate-confined Si/SiO_2 quantum-dot cellular automata (QCA) The *lower panel* shows material composition: thin (5 nm) SiO_2 insulating layers grown on a Si block with an unintentional $p = 10^{15}\,cm^{-3}$ p-doping. Top gates define quantum dot system just below the hetero-interface at $z = z_0$. The *upper panel* illustrates potential QCA cell formation: group of four positive small attractor gates (shaded circles) from charge-coupled system of close quantum dots. The entire QCA cell is surrounded by negative depletion gate (also shaded) to enhance confinement.

here a possible realization of a Si/SiO_2 quantum-dot cellular automata.

The *upper panel* of Figure 1 shows schematics of the small but experimentally accessible top-gate geometry assumed for our model Si/SiO_2 QCA system. A negative depletion gates (shaded) surrounds a group of four positive attractor gates (shaded circles) with a $r = 10$ nm radius and mutual separation of 30 nm. The attractor gates are biased to about 1 V to ensure a single-electron equilibrium occupation in each of the four electrostatically confined quantum dots. For the top silicondioxide layer we assume a 5 nm thickness.

In our $T = 100$ K simulations, the confining potential is obtained from the Poisson equation within a self-consistent Thomas-Fermi charge model. The silicon is assumed to have a small unintended but fully ionized doping, $p = 10^{15}\,cm^{-3}$ and to ensure convergence we investigate a 1.5 nm thick bottom slab with in-plane extension of approximately 300 nm by 300 nm. The top metal depletion and attractor gates are described by Dirichlet boundary conditions. For the exposed SiO_2 surface we assume for simplicity a potential fixed at the mid-gap SiO_2 value, that is, again a Dirichlet boundary condition.

Our finite-element calculation uses a 129 by 129 nonuniform grid to allow a 1 nm resolution from the surface and well below the Si/SiO_2 interface, that is, around the quantum dot system. The *top panel* of Figure 2 shows how most nodal layers (at constant z) are connected in a mesh with alternating tetrahedron orientation to eliminate a geometrical bias. The *bottom panel* of Figure 2 illustrates the repeated thinning of our finite-element mesh undertaken deep below the interfaces where a high in-plane resolution is no longer needed. However, our numerical simulation still involves 6×10^5 nodal points for which we determine the electrostatic potential within the self-consistent Thomas Fermi screening model. Using the Newton-Ralphson procedure we solve in each iteration the resulting huge linear system using a quasi-minimal residual implementation [7].

Figure 3 shows our finite-element determination of the electron potential and charge distribution along the interface ($z = z_0$) for our possible QCA realization. The electron confinement potential (*top panel*) is calculated relative to the Fermi energy with negative values corresponding to a strongly enhanced electron concentration n_{el} (*bottom panel*). Note how the thin silicon-dioxide top layer allows a very well-defined set of quantum dots with a finite inter-dot potential barriers. The total equilibrium occupation is set to exactly four electrons and the strong Coulomb blockade effect will prevent multiple occupation of the individual quantum dots.

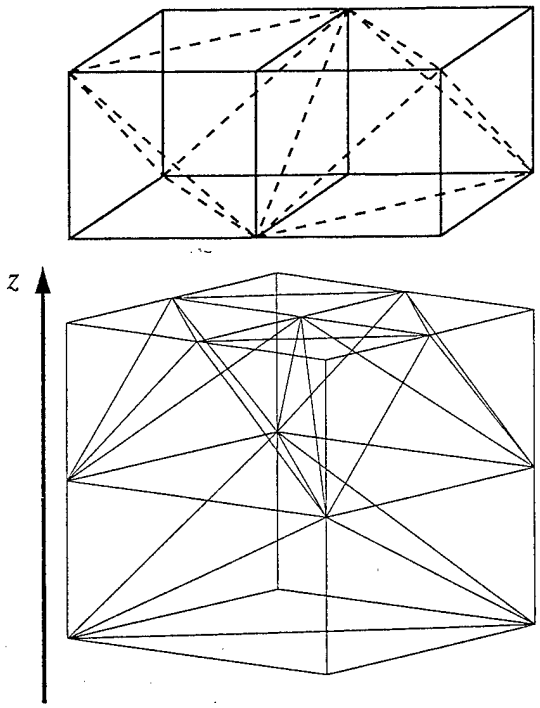

FIGURE 2 Three-dimensional finite-element modeling of gated Si/SiO_2 quantum-dot systems. The *upper panel* shows tetrahedron-based mesh with alternating cell orientation used in most in-plane layers (i.e., with constant z) to eliminate geometric bias. The *lower panel* illustrate repeated mesh thinning at layers deep below the interface ($z \ll z_0$) used to obtain a factor-of-two reduction in numerical complexity.

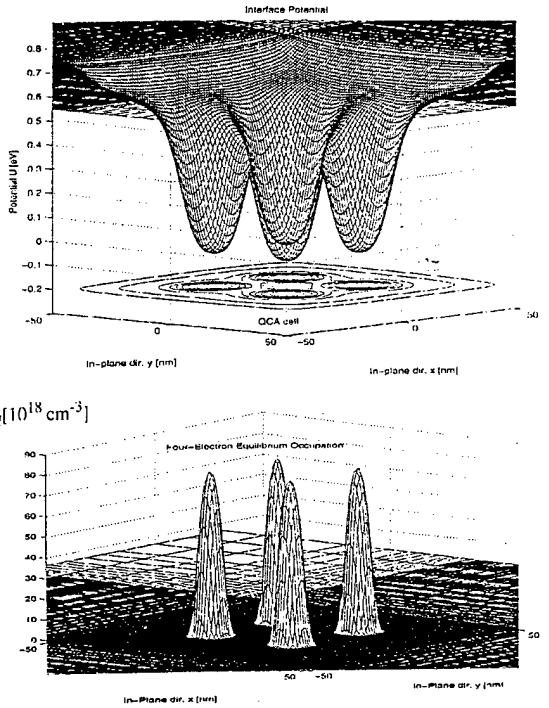

FIGURE 3 Electron potential and charge distribution of possible QCA cell at the heterostructure interface ($z = z_0$). Potential is calculated for an experimentally accessible gate geometry: four attractor gate of radius $r = 10$ nm with mutual 30 nm separation. The *upper panel* shows potential dips (measured relative to Fermi energy) with corresponding contour plot and illustrates the crisp gate control allowed by the thin SiO_2 top layer. The electron potential confines in equilibrium exactly four electrons with very well-defined charge distribution n_{el} (*lower panel*).

Figure 4 shows our modeling results for the simpler double-quantum-dot system in which we are preparing to investigate the *mutual* charge coupling between the quantum dots. We assume again $r = 10$ nm attractor gates with a mutual separation of 30 nm and adjust the positive bias to achieve a single-electron equilibrium occupation of each of the quantum dots. The *upper panel* shows the variation of the confinement potential both along the axes (x) connecting the two quantum dots and in the growth direction (z). The heterostructure-cut panel illustrates the excellent top-gate control of the electrostatic potential into the Si/SiO_2 slab well below the heterostructure interface, $z = z_0$.

The *lower panel* of Figure 4 shows the corresponding equilibrium charge distribution, n_{el}. Note that this electron distribution, i.e., the equilibrium quantum dot, is confined within 1 nm of the interface and about 5 nm of the attractor-gate center. Future modeling will investigate the charge coupling of such quantum-dot disks in the presence of the attractor and depletion gates.

In summary, we have presented three-dimensional finite-element calculations for gate-confined few-electron Si/SiO_2 quantum-dot systems. We have documented the feasibility of crisp electrostatic gate control for also few-electron quantum-dot systems and have investigated the detailed charge distribution and confinement potentials. Our modeling tool allows future investigations of charge coupling in few-electron quantum-dot cellular automata structures.

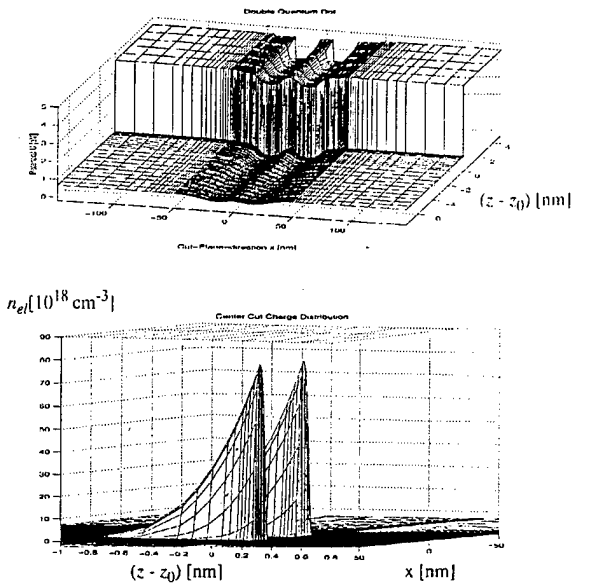

FIGURE 4 Growth direction (z) variation of confinement potential (*upper panel*) and corresponding (equilibrium) charge distribution (*lower panel*) in simpler double-dot model system. This system is defined by two $r = 10$ nm attractor dots also with a mutual separation of 30 nm. All z-positions are given relative to the interface $z = z_0$. Note that the equilibrium electron distribution n_{el} is confined within 1 nm of the interface and about 5 nm of the attractor-gate center.

Acknowledgements

This work has been supported by the Advanced Research Projects Agency through the Office of Naval Research.

References

[1] Lent, C. S., Tougaw, P. D., Porod, W. and Bernstein, G. H. (1993). "Quantum cellular automata", *Nanotechnology*, **4**, 49; Lent, C. S., Tougaw, P. D. and Porod, W. (1993). "Bistable saturation in coupled quantum dots for quantum cellular automata", *Appl. Phys. Lett.*, **62**, 714; Tougaw, P. D., Lent, C. S. and Porod, W. (1993). "Bistable saturation in coupled quantum-dot cells", *J. Appl. Phys.*, **74**, 3558.

[2] Matsuoka, H., Ichiguchi, T., Yoshimura, T. and Takeda, E. (1994). "Coulomb blockade in the inversion layer of a Si metal-oxide-semiconductor field-effect transistor with a dual-gate structure", *Appl. Phys. Lett.*, **64**, 586; and Matsuoka, H., Ichiguchi, T., Yoshimura, T. and Takeda, E. (1994). "Mesoscopic transport in Si metal-oxide-semiconductor field-effect transistor with a dual-gate structure", *J. Appl. Phys.*, **76**, 5561.

[3] Yano, K., Ishii, T., Hashimoto, T., Kobayashi, T., Murai, F. and Seki, K. (1994). "Room-Temperature Single-Electron Memory", *IEEE Trans. Electron Dev.*, **41**, 1628.

[4] Chen, M., Porod, W. and Kirkner, D. J. (1994). "Coupled finite element/boundary element method for semiconductor quantum devices with exposed surfaces", *J. Appl. Phys.*, **75**, 2545; Chen, M. and Porod, W. (1995). "Design of gate-confined quantum-dot structures in the few-electron regime", *J. Appl. Phys.*, **78**, 1050.

[5] Chen, M. and Porod, W., "Simulation of Quantum-Dot Structures in Si/SiO_2", *VLSI Design*, in press.

[6] Udipi, S., Vasileska, D. and Ferry, D. K. (1996). "Numerical Modeling of Silicon Quantum Dots", *Superlat. and Microstruct*, **20**, 343.

[7] Freund, R. W. and Nachtigal, N. M. (1991). "QMR: a Quasi-Minimal Residual Method for Non-Hermitian Linear System", *Numerische Mathematik*, **60**, 315; Lanczos, C. (1952). "Solution of Systems of Linear Equations by Minimized Iterations", *J. Research Nat. Bur. of Standards*, **49**, 33; see also C. Lanczos (1950). "An Iteration Method for the Solution of the Eigenvalue Problem of Linear Differential and Integral Operators", *J. Research Nat. Bur. of Standards*, **45**, 255.

Authors' Biographies

Per Hyldgaard is a postdoctoral research associate in the Department of Electrical Engineering at the University of Notre Dame. His research interests include computational and theoretical modeling of Coulomb blockade systems. He is a member of the APS and of the Danish and European Physical Societies.

Henry K. Harbury is Director of the computation facilities of the College of Science at the University of Notre Dame. His interests are computational modeling of solid state electronic devices.

Wolfgang Porod is Professor of Engineering at the University of Notre Dame. His research interests include computational solid state electronics and the physics of computation. He is a member of the APS and a senior member of the IEEE.

Correlated electron transport in coupled metal double dots

Alexei O. Orlov,[a] Islamshah Amlani, Geza Toth, Craig S. Lent, Gary H. Bernstein, and Gregory L. Snider
Department of Electrical Engineering, University of Notre Dame, 275 Fitzpatrick, Notre Dame, Indiana 46556

(Received 2 June 1998; accepted for publication 12 September 1998)

The electrostatic interaction between two capacitively coupled, series-connected metal double dots is studied at low temperatures. Experiment shows that when the Coulomb blockade is lifted, by applying appropriate gate biases, in both double dots simultaneously, the conductance through each double dot becomes significantly lower than when only one double dot is conducting a current. The conductance lowering seen in interacting double dots is compared to that caused by an external ac modulation applied to the double-dot gates. The results suggest that the conductance lowering in each double dot is caused by a single-electron tunneling in the other double dot. Here, each double dot responds to the instantaneous, rather than average, potentials on the other double dot. This leads to correlated electron motion within the system, where the position of single electron in one double dot controls the tunneling rate through the other double dot. © *1998 American Institute of Physics.* [S0003-6951(98)04445-3]

In the last few years, much attention has been given to coupled Coulomb blockade systems; series and parallel connected metal and semiconductor systems were studied in various aspects.[1] Correlated transport in capacitively coupled Coulomb blockade systems was studied recently both theoretically[2] and experimentally,[3] but the discussion was limited to the second-order (cotunneling) transport processes. Another example of a system utilizing correlated tunneling processes in coupled quantum dots is the basic cell of quantum-dot cellular automata (QCA).[4] The basic cell of QCA consists of four dots situated at the corners of a rectangle, and charged with two excess electrons. Due to the Coulomb repulsion, the electrons stay in the two possible diagonal positions, which can be switched by applied input signal. A functional QCA cell was first demonstrated in Ref. 5. More recently, the cell consisting of the two identical capacitively coupled double dots (DDs), was studied.[6] In addition to the possible applications, a QCA cell is an interesting model system allowing us to study interaction and correlation effects of single electrons. In this letter, we report an experimental study of correlated electron transport in a QCA cell described by Amlani *et al.*[6]

In contrast to previous work,[2,3] which studied cotunneling in a similar system, in this letter, we study the interaction between DDs in the regime when single-electron tunneling occurs in both DDs simultaneously. This is accomplished by applying appropriate biases to the gates controlling the charge state of the system, so that both of the DDs are in the transitional state. We define a transitional state for a DD as a charge state where, if no source-drain bias is applied, an excess electron bounces between dots, spending half of its time on each of the dots. At finite temperature conductance through the DD in this state is nonzero due to a contribution to the conductance through excited states. We found that if both DDs are in the transitional state the conductance through each DD becomes significantly lower than when only one DD is in its transitional state, with the other DD electrons "locked" by Coulomb blockade. To study the origin of this conductance reduction, we compare the conductance lowering observed for both DDs in the transitional state to that caused by an external *ac* modulation applied to the gates of one DD in the transitional state. The result supports the model that the conductance lowering for the DD in the transitional state is caused by the single-electron tunneling in the other DD. For noninteracting DDs, the conductance is limited by the tunneling rate of electrons through the DD, while in coupled DDs the tunneling rate is modified by the additional requirement that the excess electron on the other DD must be in the proper position before tunneling can take place. Thus, tunneling events in both DDs are strongly correlated and position of a single electron in one DD controls the tunneling rate in the other DD. The most interesting fact is that the conductance in one DD responds to the instantaneous potential changes on the other DD. The frequency of that process is determined by the single-electron tunneling rate, and is greater than 20 MHz even at millikelvin temperatures. On the contrary, the average potential cannot affect the tunneling in the other DD, since it is zero at the transitional state.[7] This shows that coupled quantum dots can respond to rapidly changing input voltages, which suggests that the operating frequency of devices such as QCA can be very high.

Figure 1(a) shows the scanning electron microscopy (SEM) micrograph of the device; schematic diagram of the device and experimental setup is shown in Fig. 1(b). The device under study consists of two pairs of metal (Al) islands (dots)—D_1D_2 and D_3D_4 connected in series by tunnel junctions. The DDs are electrostatically coupled to each other by capacitors C_c. Al/AlOx/Al tunnel junctions are fabricated on an oxidized Si substrate using electron beam lithography and shadow evaporation.[8] The area of the junctions is about 50 $\times$ 50 nm^2. Measurements were performed in a dilution refrigerator with a base temperature of 10 mK.

Conductances of each DD were measured simulta-

[a]Electronic mail: orlov.1@nd.edu

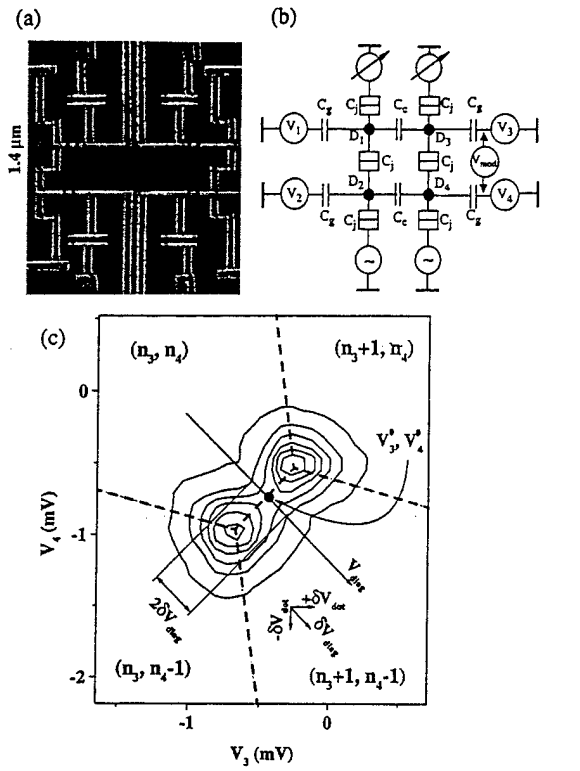

FIG. 1. (a) SEM micrograph of the device. (b) Schematic diagram of the device and experiment. (c) Contour plot of conductance through a double dot D_3D_4 as a function of gate voltages V_3 and V_4; (n_3,n_4) is the number of excess electrons on dots D_3 and D_4.

neously using standard *ac* lock-in technique with 5 μV excitation, and a magnetic field of 1 T applied to suppress the superconductivity of Al. Capacitances of the circuit ($C_j \approx 1.44e$/mV, $C_c \approx 0.9e$/mV, $C_g \approx 0.45e$/mV) were determined from periods of Coulomb blockade oscillations and $I-V$ measurements.[9] To suppress the effect of parasite crosstalk capacitances between dots and nonadjacent gates, we used a charge cancellation technique described elsewhere.[10]

To understand the experiment, we need to look at the charging processes for one DD. By measuring the conductance through a DD as a function of the voltages applied to the DD gates V_3 and V_4 (we will consider DD D_3D_4, but D_1D_2 is similar), we can determine the electron charge configuration within the DD. A contour plot of the conductance through D_3D_4 as a function of gate voltages V_3 and V_4 is shown in Fig. 1(c). At low temperatures ($kT \ll E_c$, where $E_c \sim 100$ μV is the charging energy of D_3D_4) current flows through a DD only at the settings of the gate voltages where the Coulomb blockade is lifted. Due to capacitive coupling between dots each conductance peak splits in two.[11] Dashed lines in Fig. 1(c) delineate the regions where a particular configuration (n_3,n_4) is the ground state, with n_3 and n_4 representing the number of excess electrons on dots D_3 and D_4, respectively.[11] An exchange of an electron between the two dots occurs along diagonal direction V_{diag}, while total charge on D_3D_4 remains constant along this direction.

As mentioned above, the conductance remains nonzero in the middle of the split peak at 50 mK (which we believe is the actual electron temperature in our experiment) due to a contribution to the conductance through excited states.

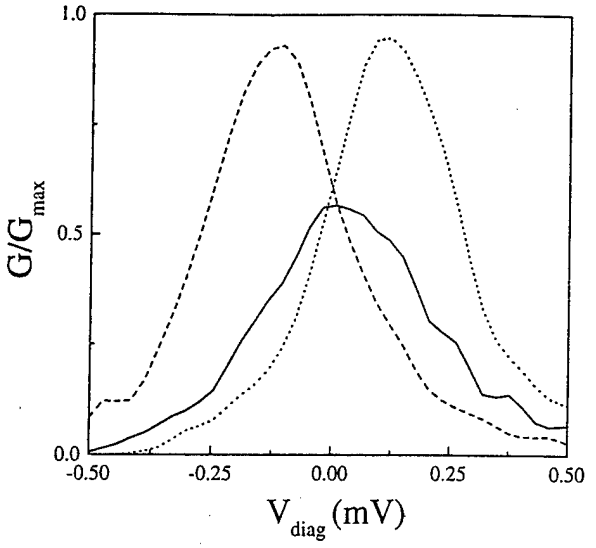

FIG. 2. Conductance through the D_3D_4 along V_{diag} for different charge states of D_1D_2: dashed line—(n_1,n_2); dotted line—(n_1+1, n_2-1); solid line—transitional state.

Therefore, the region between each split peak forms a saddle point in $G-V_3-V_4$ space, which shows up as a conductance peak along V_{diag} on Fig. 1(c). We use this peak as a marker, which corresponds to a border between states with different electron configurations. We will concentrate on the transition region between the two charge configurations (n_3,n_4) and (n_3+1, n_4-1). To set a DD in the transitional state, the working point $[V_3^0, V_4^0$ in Fig. 1(c)] must be at the saddle point of a split peak, on the border between two charge configurations (n_i,n_j) and (n_i+1, n_j-1), where $i,j=1,2$ and 3,4.

Each time an electron hops from one island of a DD to the other, the electrostatic potential on the island losing the electron becomes more positive and the potential on the island gaining that electron becomes more negative with re-

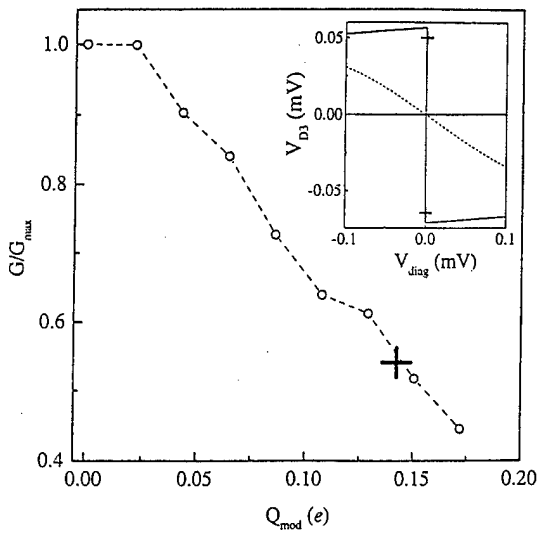

FIG. 3. Conductance peak height as a function of charge variation for DD D_3D_4 at $V_{\text{diag}}=0$, $T=10$ mK, $f_{\text{mod}}=335$ Hz. V_1, V_2 are set to lock electrons on D_1D_2 in the Coulomb blockade. Charge coordinate of the cross is the theoretically calculated charge variation produced by a single electron tunneling from dot D_1 to D_2. **Insert:** Potential on D_3 vs V_{diag}: solid line—theory for 0 K, dashed line—theory for 50 mK, crosses show potential difference extracted from the external modulation experiment.

spect to ground. On average at the saddle point of a split peak, the theoretically calculated excess occupation of each dot is 50% with a voltage phase difference of 180° between them.[7] In the transitional state, the potential on each dot as a function of time can be viewed as a series of voltage "pulses" with amplitude δV_D, corresponding to the presence or absence of an electron. The "duty cycle" of these pulses depends on V_{diag}. For $V_{\text{diag}}=0$, the duty cycle is 50%, since an electron has an equal probability to be at either dot of DD. The frequency of the pulses is defined by single-electron tunneling rate $\Gamma=kT/e^2R_j$ (where $R_j\approx 1\,\text{M}\Omega$ is the resistance of a tunnel junction) and for $T=50$ mK is about 20 MHz.

Therefore, this situation can be viewed as if the potentials on one DD act as a time varying effective gate voltages for the other DD. On the charging diagram in Fig. 1(c), the effect of such switching potential on the adjacent DD corresponds to the two settings of effective diagonal gate bias $\delta V_{\text{diag}}=\pm[(+\delta V_{\text{dot}})^2+(-\delta V_{\text{dot}})^2]^{1/2}$, where $+\delta V_{\text{dot}}$ is a change of the electrostatic potential on the dot losing and $-\delta V_{\text{dot}}$ on the dot gaining the electron (we define $V_{\text{diag}}=0$ for $V_3=V_3^0$, $V_4=V_4^0$). In response to the instantaneous change of the potentials $\pm\delta V_{\text{diag}}$ on D_1D_2, the electron tunneling rate in D_3D_4 reduces as evidenced by the reduction of conductance in Fig. 1(c). In effect, a negative potential on dot D_1, due to the presence of an electron, prevents another electron from tunneling onto D_3 until the first electron moves to D_2. As a result conductance of D_3D_4 drops compared to the case when charge on D_1D_2 is locked and potentials on D_1 and D_2 are fixed, as seen in Fig. 2. At the same time, if conductance through one DD were affected by only the average potential on the other DD, no conductance reduction is expected. Thus, according to the experiment of Fig. 2, transport of electrons through the system when both DDs are in the transitional state becomes strongly correlated, with the probability for an electron to tunnel through one DD dependent on the position of the excess electron on the other DD. The effect of conductance reduction is observed in all samples under study (a total of three samples). The correlation strength and conductance reduction depend on temperature and disappear at $kT\sim E_c$.[7]

At $V_{\text{diag}}=0$, we can model the conductance modulation caused by a single-electron switching in D_1D_2 by applying a square-wave modulation with a 50% duty cycle to the gates V_3 and V_4. The applied signals must be out of phase by 180° to imitate the electron hop from D_1 to D_2. The potential difference produced by D_1D_2 is $\delta V=V_{D_1}-V_{D_2}$, and the charge which affects the D_3D_4 is therefore $\delta Q=\delta VC_c$. To mimic the same amount of charge variation, $\delta Q=\delta V_gC_g=\delta VC_c$, a signal of $\delta V_g=\delta VC_c/C_g$ must be applied to the gates. Gate voltages on D_1D_2 are set to lock electrons there in Coulomb blockade to prevent any effects in D_3D_4 caused by single-electron tunneling in D_1D_2.

We apply a square-wave differential modulation signal between the gates V_3 and V_4 with a frequency of 100–10000 Hz, much lower than a single-electron tunneling rate. The result of this gate modulation experiment is shown on the Fig. 3 where the conductance of the D_3D_4 measured at $V_{\text{diag}}=0$ is plotted versus the amplitude of applied charge modulation. The cross in Fig. 3 marks the conductance lowering observed in the experiment of Fig. 2. The observed conductance lowering was frequency independent up to 10 kHz (cutoff frequency of our experimental setup). The position of the cross confirms that the conductance lowering occurs due to the instantaneous potential variation caused by electrons tunneling through the other DD. The insert in Fig. 3 shows the theoretically calculated dot potential versus V_{diag} at 0 K. The theoretical results are obtained by minimizing the classical electrostatic energy for the array of islands and voltage leads. Finite temperature smears the transition region, but for $V_{\text{diag}}=0$, the instantaneous values of potential remain the same, jumping between "high" and "low" levels, while the average potential is zero. The crosses in the insert of Fig. 3 mark the amplitude of the normalized external modulation at which the conductance peak height matches that observed in Fig. 2 and shows good agreement with theory. Therefore, the external modulation experiment can be used to measure the potential difference between the dots, and provides further evidence that the conductance reduction is due to instantaneous potential variations.

In summary, we report the observation of correlated transport in the Coulomb coupled double dots. We found that when single-electron tunneling takes place in both DDs simultaneously the conductance through each of the interacting DDs drops. We explain this conductance lowering by electrostatic interactions between DDs, where the conductance through each of the DDs is affected by instantaneous changes of electrostatic potentials created by electrons tunneling through the dots in the other DD. We confirm this by an experiment where square-wave modulation was applied between the gates of DD to simulate potential changes caused by single-electron tunneling in the other DD, and find a good agreement with theoretical calculations. Our results suggest that coupled DD can respond to rapid changes of input voltages, implying very high operating frequencies of devices based on quantum dots, such as QCA.

This research was supported in part by DARPA, ONR (Grant No. N00014-95-1-1166) and NSF. The authors are grateful to W. Porod and J. Merz for stimulating discussions.

[1] L. P. Kouwenhoven *et al.*, in *Proceedings of the Advanced Study Institute on Mesoscopic Electron Transport*, edited by L. L. Sohn, L. P. Kouwenhoven, and G. Schon (Kluwer, Dordrecht, 1997).
[2] D. V. Averin, A. N. Korotkov, and Yu. V. Nazarov, Phys. Rev. Lett. **66**, 2818 (1991).
[3] P. Delsing, D. B. Haviland, and P. Davidsson, Czech. J. Phys. **46**, 2359 (1996).
[4] C. S. Lent, P. D. Tougaw, W. Porod, and G. H. Bernstein, Nanotechnology **4**, 49 (1993).
[5] A. O. Orlov, I. Amlani, G. H. Bernstein, C. S. Lent, and G. L. Snider, Science **277**, 928 (1997).
[6] I. Amlani, A. O. Orlov, G. L. Snider, C. S. Lent, and G. H. Bernstein, Appl. Phys. Lett. **72**, 2179 (1998).
[7] G. Toth and C. S. Lent (unpublished).
[8] T. A. Fulton and G. H. Dolan, Phys. Rev. Lett. **58**, 109 (1987).
[9] C. Livermore, C. H. Crouch, R. M. Westervelt, K. L. Campman, and A. C. Gossard, Science **20**, 1332 (1996).
[10] G. L. Snider, A. O. Orlov, I. Amlani, G. H. Bernstein, C. S. Lent, J. L. Merz, and W. Porod, Solid-State Electron. **42**, 1355 (1998).
[11] H. Pothier, P. Lafarge, P. F. Orfila, C. Urbina, D. Esteve, and M. H. Devoret, Physica B **169**, 573 (1991).

Digital Logic Gate Using Quantum-Dot Cellular Automata

Islamshah Amlani,[1]* Alexei O. Orlov,[1]
Geza Toth,[1,2] Gary H. Bernstein,[1] Craig S. Lent,[1]
Gregory L. Snider[1]

A functioning logic gate based on quantum-dot cellular automata is presented, where digital data are encoded in the positions of only two electrons. The logic gate consists of a cell, composed of four dots connected in a ring by tunnel junctions, and two single-dot electrometers. The device is operated by applying inputs to the gates of the cell. The logic AND and OR operations are verified using the electrometer outputs. Theoretical simulations of the logic gate output characteristics are in excellent agreement with experiment.

Field-effect transistors (FETs) are the foundation of present digital logic technologies such as complementary metal oxide semiconductors. Despite vast improvements in integrated circuit fabrication technology over the past three decades, the role played by the FET has remained that of a current switch, much like the mechanical relays used by Konrad Zuse in the 1930s. By adhering to strict scaling rules, FETs have maintained acceptable performance despite tremendous reductions in size, permitting the microelectronics industries to make phenomenal increases in device density and computational power. As device feature sizes approach quantum limits, fundamental effects will make further scaling difficult, requiring a departure from the FET-based paradigm and necessitating revolutionary approaches to computing. The approach must be compatible with the inherent properties of nanostructures, as it should exploit the effects that accompany small sizes. An alternate paradigm is that of quantum-dot cellular automata (QCA) (*1–3*), which uses the arrangements of individual electrons, instead of currents and voltages, to encode binary information.

QCA is a nanostructure-compatible computation paradigm that uses arrays of quantum-dot cells to implement digital logic functions. A key element of this paradigm is a QCA cell, which consists of four dots located at the vertices of a square (Fig. 1A); such a cell was experimentally demonstrated (*4*). When the cell is charged with two excess electrons, they occupy diagonal sites as a result of mutual electrostatic repulsion. The two diagonal polarizations are energetically equivalent ground states of the cell, and are used to represent logic 0 and logic 1. A polarization change in a QCA cell is induced by causing an electron to switch positions in one set of dots, thus inducing an opposite electron switch in an adjacent set of dots, resulting in a change of the electron arrangement from one diagonal to the other.

The fundamental QCA logic device is a three-input majority logic gate (Fig. 1B) consisting of an arrangement of five standard cells: a central logic cell, three inputs labeled *A*, *B*, and *C*, and an output cell. The polarization states of inputs *A*, *B*, and *C* determine that of the logic cell, which can assume either polarization, while the output polarization follows that of the logic cell. In operation, the polarization of the logic cell becomes that of the majority of the three input cells. QCA logic gates can be cascaded, so that in a more complex QCA circuit, the three inputs would be driven by the outputs of previous gates. Similarly, the output of the majority gate can be connected to drive a subsequent stage of logic gates (*5*).

A majority gate can be programmed to act as an OR gate or an AND gate by fixing any one of the three inputs as a program line. If the programming input is a 0, the AND operation is performed on the remaining two inputs. If the programming input is a 1, the OR operation is performed on the other two inputs (Fig. 1C).

Although QCA architecture can be implemented in many systems, we choose the metal tunnel junction implementation described by Lent and Tougaw (*3*). In our QCA system (Fig. 1D), the cell consists of four small Al islands ("dots"), D_1 to D_4, connected in a ring by AlO_x tunnel junctions. In initial biasing of the cell, two excess electrons enter the cell through tunnel junctions, which for simplicity are not shown. A complete schematic for a related experiment has been published (*4*). Junction capacitances C_J are sufficiently small to ensure charge quantization on each dot at cryogenic temperatures (*6*). Each dot is also capacitively coupled to a gate, via capacitance C_G, that influences the charge state of its respective dot. To determine the cell polarization, we measure electrostatic potentials on islands D_3 and D_4 using capacitively coupled single dots, E_1 and E_2, as noninvasive electrometers (*7, 8*).

Nanometer-scale $Al/AlO_x/Al$ tunnel junctions are fabricated using the standard Dolan-bridge technique (*9*). Aluminum islands and leads are defined by electron beam lithography and subsequent shadow evaporation processes with an intermediate in situ oxidation step. The experiment is performed in a dilution refrigerator with an ambient magnetic field of 1 T to suppress the superconductivity of Al metal. All relevant capacitances are extracted from measurements of Coulomb blockade oscillations (*4*), and are used in theoretical simulations of the device characteristics using classical Coulomb blockade theory. The effects of unintentional cross-talk capacitances between each gate and all nonadjacent dots are compensated using feedback circuitry (*10*).

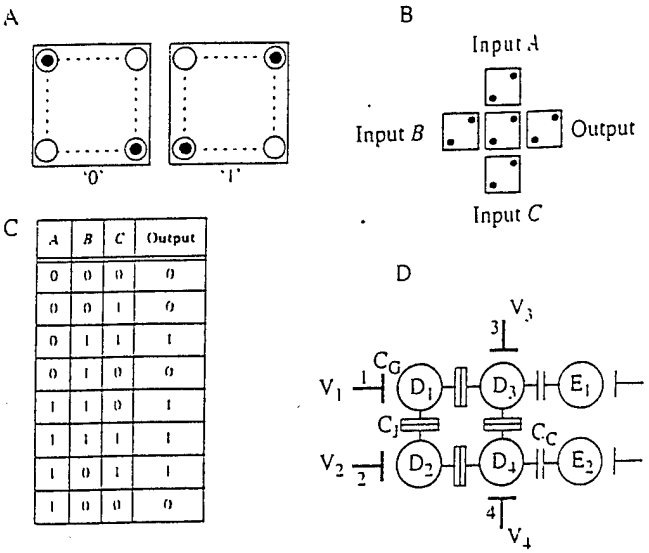

A	B	C	Output
0	0	0	0
0	0	1	0
0	1	1	1
0	1	0	0
1	1	0	1
1	1	1	1
1	0	1	1
1	0	0	0

Fig. 1. (A) QCA cell showing two possible polarizations. (B) QCA majority gate, the fundamental logic element of the QCA paradigm. (C) Truth table containing all possible input combinations in Gray code, and majority gate outputs. (D) Schematic of our QCA system. The cell is defined by dots D_1 to D_4 connected in a ring by tunnel junctions. Dots D_3 and D_4 are capacitively coupled to electrometer dots E_1 and E_2, respectively. External leads and tunnel junctions for the cell and the electrometers are not shown.

[1]Department of Electrical Engineering, University of Notre Dame, Notre Dame, IN 46556, USA. [2]Neuromorphic Information Technology Graduate Center, Budapest, Kende-u.13, H-1111, Hungary.

*To whom correspondence should be addressed. E-mail: islamshah.amlani.1@nd.edu

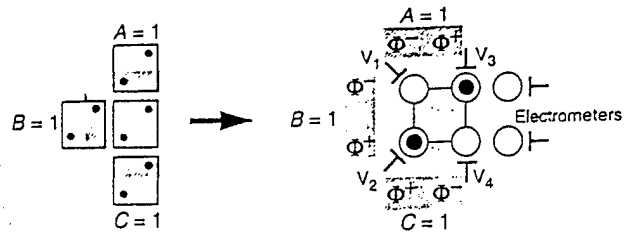

Fig. 2. Experimental setup for majority gate demonstration. Inputs *A*, *B*, and *C* (shaded at left) are replaced by potential shifts on the gates (shaded at right) that are equivalent to polarization states of the input cells.

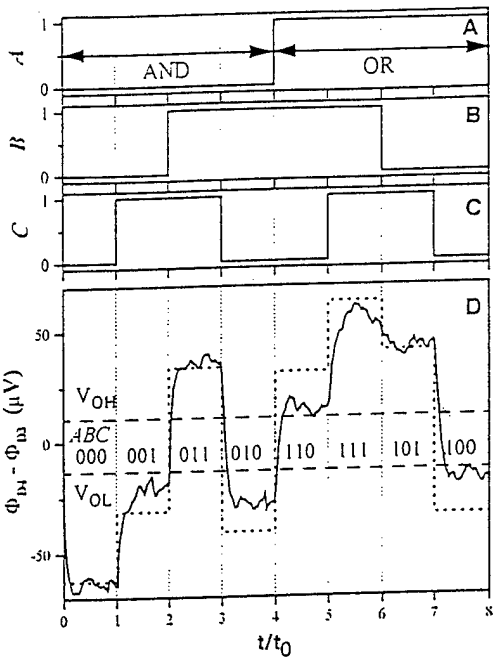

Fig. 3. Demonstration of majority gate operation. (A to C) Inputs in Gray code. The first four and last four inputs illustrate AND and OR operations, respectively. (D) Output characteristic of majority gate where t_0 = 20 s is the input switching period. The dashed line shows the theory for 70 mK; the solid line represents the measured data. Output high (V_{OH}) and output low (V_{OL}) levels are marked by dashed lines.

First, the logic cell is biased using gates 1 to 4 in an unpolarized state where logic 1 and 0 are equally probable (*4*), and the electrometer outputs are set to 0 V for this condition. This procedure also cancels the effect of the substrate background charge. Figure 2 shows the correspondence between the representation on the left and the configuration of our majority gate experiment on the right. Differential signals *A* (between gates 1 and 3), *B* (between gates 1 and 2), and *C* (between gates 2 and 4) constitute the inputs to the central cell. The negative (positive) bias on a gate, Φ^- (Φ^+), mimics the presence (absence) of an electron in the input dots, as shown by the shaded regions in Fig. 2. The amplitudes of Φ^- and Φ^+ are carefully chosen to mimic the potentials due to the polarization of an input cell while they remain small enough not to change the number of excess electrons in the cell.

Differential signals *A*, *B*, and *C* are converted into logic levels 1 and 0 on the basis of the convention used in Fig. 1A. As dots D_1 and D_2 are coupled to only one gate electrode each, voltages corresponding to inputs *A* and *B* on gate 1, and inputs *B* and *C* on gate 2, are added in order to mimic the effect of two input dots. For instance, the input configuration shown in Fig. 2 (*ABC* = 111) is achieved by setting $V_1 = 2\Phi^-$, $V_2 = 2\Phi^+$, $V_3 = \Phi^+$, and $V_4 = \Phi^-$.

With inputs *A*, *B*, and *C* traced as a function of time (Fig. 3, A to C) according to the truth table in Fig. 1C, the differential potential between dots D_4 and D_3, $\Phi_{D4} - \Phi_{D3}$, is measured using the electrometers E_2 and E_1 (Fig. 3D). (The transient characteristics are determined by the time constant of our electrometer circuitry.)

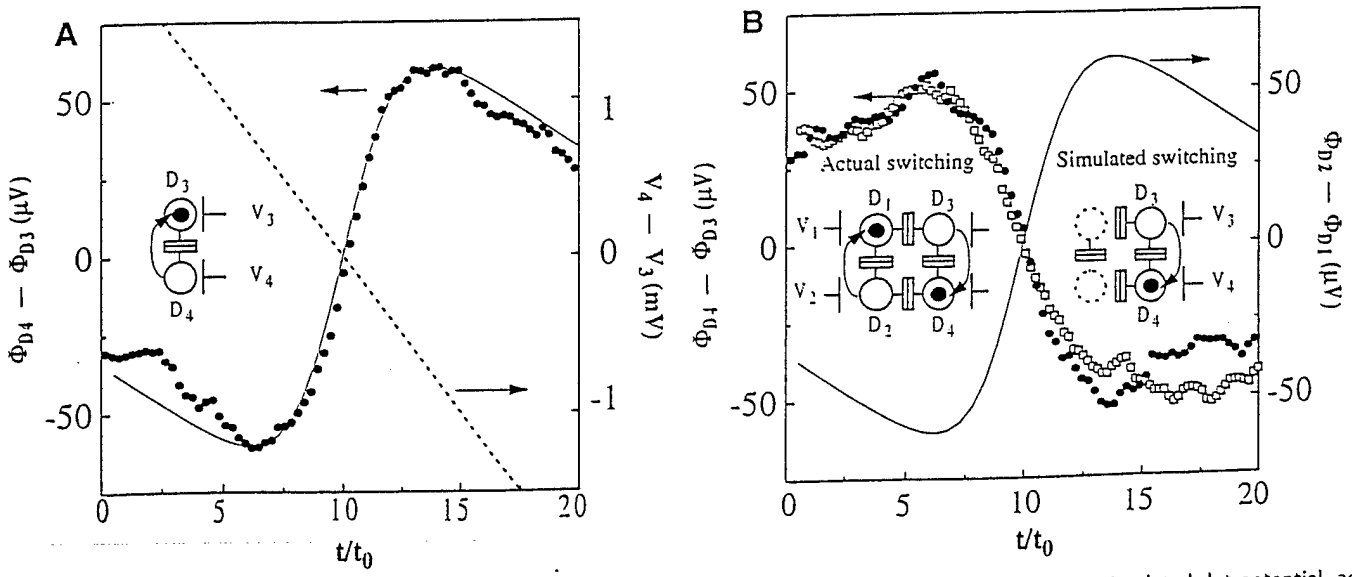

Fig. 4. (A) Differential potential change on the dots as an electron switches from D_4 to D_3. The dashed line represents the differential input voltage applied to gates 3 and 4 as a function of time. Solid circles show the measured data and the solid line represents the theoretical prediction for 70 mK; t_0 = 15 s. (B) Switching induced in D_3D_4 by two mechanisms. Solid circles show the measured differential potential change of D_3D_4 caused by the simulated dot potential, as depicted by inset at right. The solid line shows the differential potential applied between gates 4 and 3 (scaled by C_J/C_G). Open squares show the measured differential potential change of D_3D_4 caused by an electron switching in D_1D_2, as depicted by inset at left; t_0 = 15 s.

The theoretical results (dashed line in Fig. 3D) are calculated for the electron temperature in the experiment (70 mK), as determined from the temperature dependence of Coulomb blockade oscillations (*11*). Although no adjustable parameters are used in the theory, the agreement between the experimental and theoretical results is excellent. The output high (V_{OH}) and output low (V_{OL}) show a clear separation, as required for digital logic. The first and last four input steps are grouped separately, with A as the programming input, to illustrate AND and OR operations. The AND operation is carried out for $A = 0$, for which we see that the output is high only when the remaining two inputs are also high. The OR operation is performed when $A = 1$, for which the output is high when either of the other two inputs is high. These data confirm majority gate operation and thus demonstrate a logic gate that requires only two electrons to function.

The gap between V_{OH} and V_{OL} would be larger for either lower temperatures or smaller capacitances. Thermal smearing of the charge states of the dots results in a less than complete polarization of the cell. Therefore, the performance of the gate could be improved by lowering the temperature. However, a better way is to reduce the dot capacitance (by reducing the size of the dots), which will raise the energy of the excited states. When all capacitances are reduced by a factor of 10, the calculated output characteristic shows increased separation between V_{OH} and V_{OL} and negligible output deviations for all input combinations. QCA logic gates using a molecular implementation will not only yield greater performance, but will also operate at room temperature (*12*).

Some key issues must be addressed to determine the response of the majority gate when it is integrated in a real QCA circuit. In QCA arrays, each cell responds to the polarizations of neighboring cells. Therefore, we must justify that the voltages applied to the central cell gates in our majority gate experiment produce the same effects as electrons switching in neighboring cells.

We performed two experiments to demonstrate that our input voltages have the same effect as that of actual electron switching in input cells *A*, *B*, and *C*. First, we found the potential swing due to an electron switching from one dot to another. We applied a differential voltage between gates 3 and 4 ($V_3 = -V_4$) to induce electron switching in D_3D_4 (inset, Fig. 4A). As an electron moves from D_4 to D_3, the potential of the bottom dot undergoes a positive shift due to removal of an electron, while the potential of the top dot undergoes a negative shift due to addition of an electron. The differential potential swing ($\Phi_{D4} - \Phi_{D3}$) for this switching is positive (Fig. 4A), with theory closely matching the measured data [the calculated differential potential swing ($\Phi_{D2} - \Phi_{D1}$) is the same when the bias is applied between gates 1 and 2]. The input signals applied to the gates in the majority gate demonstration (Fig. 3) have the same amplitudes as that shown in Fig. 4A, scaled by C_J/C_G to compensate for differences in capacitance.

Next, to demonstrate that the application of "simulated" dot potentials to the gates of the cell mimics an electron switching in a neighboring cell, we applied the differential potential extracted in the previous experiment directly to gates 3 and 4 (with the weighting factor C_J/C_G) and measured the differential potentials between D_3 and D_4. This result is compared to that due to an actual electron switching in nearby dots D_1D_2. Figure 4B shows the change in differential potential of D_3D_4 caused by the two mechanisms as a function of time (insets, Fig. 4B), with the data confirming that the response of D_3D_4 is similar when switched by either the simulated potential or a real electron. This is as expected because charge modulations induced on D_3D_4 by the two mechanisms are the same; that is, $V_3C_G = \Phi_{D1}C_J$ and $V_4C_G = \Phi_{D2}C_J$. These results confirm that using the simulated dot potentials for the inputs in our majority gate experiment is indeed a reliable indicator of how a majority gate would respond when integrated in a QCA circuit.

References and Notes

1. C. S. Lent and P. D. Tougaw, *Proc. IEEE* 85, 541 (1997).
2. ———, W. Porod, *Appl. Phys. Lett.* 62, 714 (1993).
3. C. S. Lent and P. D. Tougaw, *J. Appl. Phys.* 75, 4077 (1994).
4. A. O. Orlov, I. Amlani, G. H. Bernstein, C. S. Lent, G. L. Snider, *Science* 277, 928 (1997); I. Amlani, A. O. Orlov, G. L. Snider, C. S. Lent, G. H. Bernstein, *Appl. Phys. Lett.* 72, 2179 (1998).
5. In an integrated QCA circuit, a clocking scheme is used to control the direction of information flow. See (*1*).
6. K. K. Likharev, *IBM J. Res. Dev.* 42, 144 (1988).
7. P. Lafarge *et al.*, *Z. Phys. B* 85, 327 (1991); I. Amlani, A. O. Orlov, C. S. Lent, G. L. Snider, G. H. Bernstein, *Appl. Phys. Lett.* 71, 1730 (1997).
8. G. L. Snider *et al.*, unpublished data; G. H. Bernstein, I. Amlani, A. O. Orlov, C. S. Lent, G. L. Snider, unpublished data.
9. T. A. Fulton and G. H. Dolan, *Phys. Rev. Lett.* 58, 109 (1987).
10. G. L. Snider *et al.*, *Solid State Electron.* 42, 1355 (1998).
11. H. Grabert and M. H. Devoret, Eds., *Single Electron Tunneling* (Plenum, New York, 1992), p. 181.
12. C. S. Lent, P. D. Tougaw, W. Porod, *Proceedings of Workshop on Physics and Computation* (IEEE Computer Press, Los Alamitos, CA, 1994), vol. 5.

13. Supported in part by the Defense Advanced Research Projects Agency, the Office of Naval Research (grant N0014-95-1-1166), and NSF. We thank W. Porod and J. Merz for helpful discussions.

24 November 1998; accepted 19 February 1999

Quantum-dot cellular automata: Review and recent experiments (invited)

G. L. Snider, A. O. Orlov, I. Amlani, X. Zuo, G. H. Bernstein, C. S. Lent, J. L. Merz, and W. Porod
Department of Electrical Engineering, University of Notre Dame, Notre Dame, Indiana 46556

An introduction to the operation of quantum-dot cellular automata is presented, along with recent experimental results. Quantum-dot cellular automata (QCA) is a transistorless computation paradigm that addresses the issues of device density and interconnection. The basic building blocks of the QCA architecture, such as AND, OR, and NOT are presented. The experimental device is a four-dot QCA cell with two electrometers. The dots are metal islands, which are coupled by capacitors and tunnel junctions. An improved design of the cell is presented in which all four dots of the cell are coupled by tunnel junctions. The operation of this basic cell is confirmed by the externally controlled polarization change of the cell. © *1999 American Institute of Physics.* [S0021-8979(99)26608-X]

I. INTRODUCTION

For more than 30 years, the microelectronics industry has enjoyed dramatic improvements in the speed and size of electronic devices. This trend has long obeyed Moore's law, which predicts that the number of devices integrated on a chip will double every 18 months. Adherence to this exponential growth curve has been a monumental task requiring rapid improvements in all aspects of integrated circuit (IC) fabrication, to permit manufacturers to both shrink the size of devices and increase chip size while maintaining acceptable yields. Since the early 1970s the device of choice for high levels of integration has been the field effect transistor (FET), and while the FET of today is a vast improvement over that of 1970, it is still used as a current switch much like the mechanical relays used by Konrad Zuse in the 1930s. At gate lengths below 0.1 μm FETs will begin to encounter fundamental effects that make further scaling difficult. A possible way for the microelectronics industry to maintain growth in device density is to change from the FET-based paradigm to one based on nanostructures. Here, instead of fighting the effects that come with feature size reduction, these effects are used to advantage. One nanostructure paradigm, proposed by Lent *et al.*,[1,2] is quantum-dot cellular automata (QCA), which employs arrays of coupled quantum dots to implement Boolean logic functions.[3,4] The advantage of QCA lies in the extremely high packing densities possible due to the small size of the dots, the simplified interconnection, and the extremely low power-delay product. Using QCA cells with dots of 20 nm diameter, an entire full adder can be placed within 1 μm^2.

A basic QCA cell consists of four quantum dots in a square array coupled by tunnel barriers. Electrons are able to tunnel between the dots, but cannot leave the cell. If two excess electrons are placed in the cell, Coulomb repulsion will force the electrons to dots on opposite corners. There are thus two energetically equivalent ground state polarizations, as shown in Fig. 1, which can be labeled logic "0" and "1." Coulombic interactions between the electrons cause the cell to exhibit highly bistable switching between these two polarizations. The simplest QCA array is a line of cells, shown in Fig. 2(a). Since the cells are capacitively coupled to their neighbors, the ground state of the line is for all cells to have the same polarization. In this state, the electrons are as widely separated as possible, giving the lowest possible energy. To use the line, an input is applied at the left end of the line, breaking the degeneracy of the ground state of the first cell and forcing it to one polarization. Since the first and second cell are now of opposite polarization, with two electrons close together, the line is in a higher energy state and all subsequent cells in the line must flip their polarization to reach the new ground state. No metastable state (where only a few cells flip) is possible in a line of cells.[2] A tremendous advantage of QCA devices is the simplified interconnect made possible by this paradigm. Since the cells communicate only with their nearest neighbors, there is no need for long interconnect lines. The inputs are applied to the cells at the edge of the system and the computation proceeds until the output appears at cells at the edge of the QCA array.

Computing in the QCA paradigm can be viewed as computing with the ground state of the system. A computational problem is mapped onto an array of cells by the placement of the cells, where the goal is to make the ground state configuration of electrons represent the solution to the posed problem. Then computation becomes a task of applying a set of inputs that put the system into an excited state, and then letting it relax into a new ground state. For each set of inputs a unique system ground state exists that represents the solution for those inputs. The mapping of a combinational logic problem onto a QCA system can be accomplished by finding arrangements of QCA cells that implement the basic logic functions AND, OR, and NOT. An inverter, or NOT, is shown in Fig. 2(b). In this inverter, the input is first split into

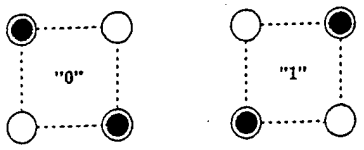

FIG. 1. Basic four-dot QCA cell showing the two possible ground-state polarizations.

0021-8979/99/85(8)/4283/3/$15.00

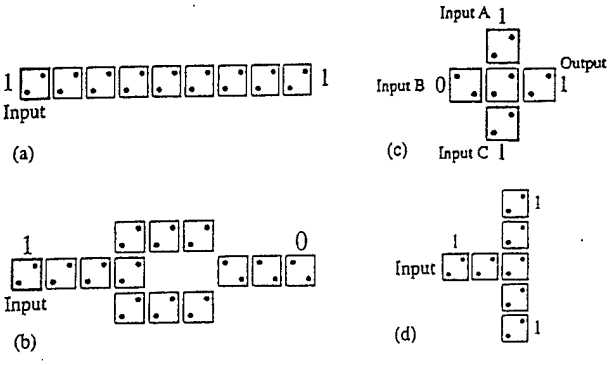

FIG. 2. (a) Line of QCA cells. (b) QCA inverter. (c) QCA majority gate. (d) Fanout.

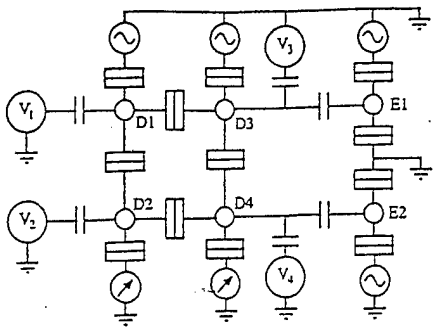

FIG. 3. Simplified schematic of the four-dot QCA cell and electrometers.

two lines of cells then brought back together at a cell that is displaced by 45° from the two lines, as shown. The 45° placement of the cell produces a polarization that is opposite to that in the two lines, as required in an inverter. AND and OR gates are implemented using the topology shown in Fig. 2(c), called a majority gate. In this gate the three inputs "vote" on the polarization of the central cell, and the majority wins. The polarization of the central cell is then propagated as the output. One of the inputs can be used as a programming input to select the AND or OR function. If the programming input is a logic 1 then the gate is an OR, but if a 0 then the gate is an AND. Thus, with majority gates and inverters it is possible to implement all combinational logic functions. Memory can also be implemented using QCA cells,[5] making general purpose computing possible.

Some additional explanation is necessary for the fan-out structure shown in Fig. 2(d), which was also employed in the inverter. When the input of one of these structures is flipped, the new ground state of the system is achieved when all of the cells in both branches flip. The problem is that the energy put into the system by flipping the input cell is not sufficient to flip cells in both branches, leading to a metastable state where not all of the cells have flipped. This is not the ground state of the system, but can be a very long-lived state, leading to erroneous solutions in a calculation. Avoiding these metastable states is simply a matter of switching the cells using a quasi-adiabatic approach, which keeps the system in its instantaneous ground state during switching, thus avoiding any metastable states. Details of quasiadiabatic switching have been published previously.[2,6] Quasiadiabatic switching can be implemented in both semiconductor and metallic QCA systems.

II. EXPERIMENT

The experimental work presented is based on a QCA cell using aluminum islands and aluminum-oxide tunnel junctions, fabricated on an oxidized silicon wafer. The fabrications uses standard electron beam lithography and dual shadow evaporations to form the islands and tunnel junctions.[7] The area of the tunnel junctions is an important quantity since this dominates island capacitance, determining the charging energy of the island and hence the operating temperature of the device. For our devices the area is approximately 60 by 60 nm, giving a junction capacitance of 400 aF. These metal islands stretch the definition of a quantum dot, but we will refer to them as such because the electron population of the island is quantized and can be changed only by tunneling of electrons.

We recently demonstrated the first step in the development of QCA systems i.e., a functional QCA cell where we can switch the polarization of a cell. This confirms that the switching of a single electron between coupled quantum dots can control the position of a single electron in another set of dots.[8,9] A simplified schematic diagram of our latest QCA system is shown in Fig. 3. The four-dot QCA cell is formed by dots D1–D4, which are coupled in a ring by tunnel junctions. A tunnel junction source or drain is connected to each dot in the cell. This implementation is an improvement over earlier designs in that the tunnel junctions coupling D1–D3 and D2–D4 provide a capacitance more than twice as large as the lithographically defined capacitance used previously. A larger capacitance is expected to improve the bistability of the cell. The two individual dots E1 and E2 are used as electrometers. The device is mounted on the cold finger of a dilution refrigerator that has a base temperature of 10 mK, and characterized by measuring the conductance through various branches of the circuit using standard ac lock-in techniques. A magnetic field of 1 T was applied to suppress the superconductivity of the aluminum metal. Full details of the experimental measurements are described elsewhere.[8–11]

Since the operation of a QCA cell depends on the position of a single electron, it is necessary to track the position of electrons within the cell. This can be done by two different methods. One is to measure the conductance through each pair of dots within the cell. A peak in the conductance as the gate voltages are changed indicates that the Coulomb blockade has been lifted for both dots simultaneously, and a change in the dot population has occurred. The other way to detect the change of an electron position within the cell is using the electrometers E1 and E2,[11] which are capacitively coupled to the cell dots D3 and D4. A small potential change in the dot being measured causes a change in the conductance of the electrometer. A decrease in the conductance of the electrometer indicates a lower potential on the measured dot, meaning that an electron has entered the measured dot.

QCA operation is demonstrated by first biasing the cell, using the gate voltages, so that an excess electron is on the point of switching between dots D1 and D2, and a second

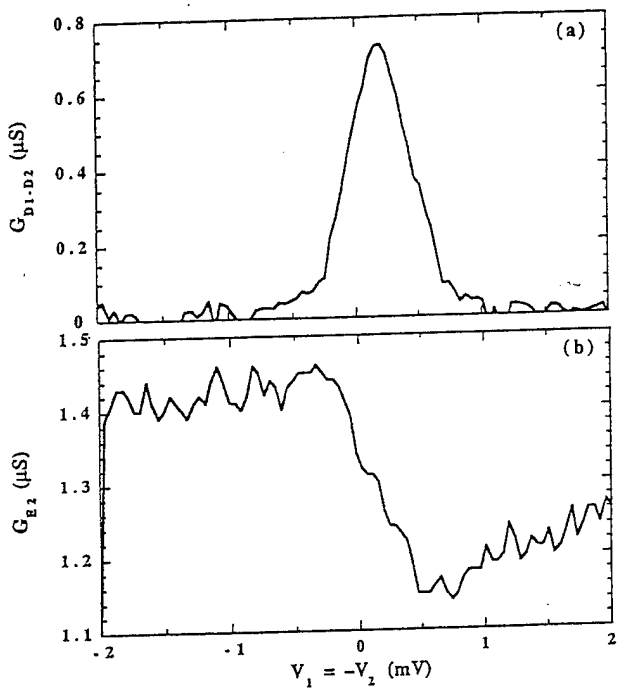

FIG. 4. (a) Conductance through dots D1 and D2. The peak occurs when the electron moves from D2 to D1. (b) and (c) Electrometer conductance. A drop in conductance occurs when an electron moves on to D4.

electron is on the point of switching between D3 and D4. A differential voltage is then applied to the input gates V_1 and V_2 ($V_1 = -V_2$), while all other gate voltages are kept constant. As the differential input voltage is swept from negative to positive, the electron starts on D2, then moves from D2 to D1, as indicated by the peak in the conductance through D1–D2 seen in Fig. 4(a). This forces the other electron to move from D3 to D4. Figure 4(b) shows the response of electrometer E2, which is coupled to dot D4. When the electron switches from D2 to D1 there is a drop in the conductance of E2, indicating that an electron has moved from D3 to D4. This confirms the polarization change in the cell, and demonstrates QCA operation.

III. SUMMARY

A device paradigm based on QCA cells offers the opportunity to break away from FET based logic, and to exploit the quantum effects that come with small size. In this new paradigm, the basic logic element is no longer a current switch but a small array of quantum dots, and the logic state is encoded as the position of electrons within a quantum dot cell. We have demonstrated the operation of a QCA cell fabricated in aluminum islands with aluminum oxide tunnel where the polarization of the cell can be switched by applied bias voltages. QCA cells are scalable to molecular dimensions, and since the performance improves as the size shrinks, a molecular QCA cell should operate at room temperature. While the device demonstrated here operates using single electrons, an implementation of QCA using magnetic domains should also be possible.

ACKNOWLEDGMENTS

This work was supported in part by the Defense Advanced Research Projects Agency, Office of Naval Research, and the National Science Foundation.

[1] C. S. Lent, P. D. Tougaw, W. Porod, and G. H. Bernstein, Nanotechnology 4, 49 (1993).
[2] C. S. Lent and P. D. Tougaw, Proc. IEEE 85, 541 (1997).
[3] C. S. Lent and P. D. Tougaw, J. Appl. Phys. 74, 6227 (1993).
[4] P. D. Tougaw and C. S. Lent, J. Appl. Phys. 75, 1818 (1994).
[5] T. J. Fountain and C. S. Lent (unpublished).
[6] P. D. Tougaw and C. S. Lent, J. Appl. Phys. 80, 4722 (1996).
[7] T. A. Fulton and G. H. Dolan, Phys. Rev. Lett. 59, 109 (1987).
[8] A. O. Orlov, I. Amlani, G. H. Bernstein, C. S. Lent, and G. L. Snider, Science 277, 928 (1997).
[9] I. Amlani, A. O. Orlov, G. L. Snider, C. S. Lent, and G. H. Bernstein, Appl. Phys. Lett. 72, 2179 (1998).
[10] G. L. Snider, A. O. Orlov, I. Amlani, G. H. Bernstein, C. S. Lent, J. L. Merz, and W. Porod, Semicond. Sci. Technol. 13, A130 (1998).
[11] I. Amlani, A. O. Orlov, G. L. Snider, C. S. Lent, and G. H. Bernstein, Appl. Phys. Lett. 71, 1730 (1997).

Experimental demonstration of a leadless quantum-dot cellular automata cell

Islamshah Amlani,[a] Alexei O. Orlov, Ravi K. Kummamuru,[b] Gary H. Bernstein, Craig S. Lent, and Gregory L. Snider
Department of Electrical Engineering, University of Notre Dame, Notre Dame, Indiana 46556

(Received 7 April 2000; accepted for publication 31 May 2000)

We present the experimental characterization of a leadless (floating) double-dot system and a leadless quantum-dot cellular automata cell, where aluminum metal islands are connected to the environment only by capacitors. Here, single electron charge transfer can be accomplished only by the exchange of an electron between the dots. The charge state of the dots is monitored using metal islands configured as electrometers. We show improvements in the cell performance relative to leaded dots, and discuss possible implications of our leadless design to the quantum-dot cellular automata logic implementation. © *2000 American Institute of Physics.* [S0003-6951(00)00731-2]

Recently, quantum-dot cellular automata (QCA) has received significant attention. In this transistorless approach to computation, logic levels are represented by the configurations of single electrons in coupled quantum-dot systems.[1–3] The simplest structure in this paradigm, a cell, consists of four dots located at the vertices of a square sharing two electrons between them. Due to electrostatic repulsion, the two electrons in each cell are forced to the opposite corners along one of the two diagonals. These diagonally aligned charge states are the ground states of the four-dot system, and are used to encode logic values "0" and "1." Since the dot sizes can ultimately be as small as single molecules, the QCA architecture offers ultrahigh device density that is predicted to be both faster and more energy efficient than conventional complementary metal–oxide–semiconductor technology.

In the last few years, significant progress has been made toward the realization of basic QCA elements. So far, a fully functional QCA cell[4,5] and a small chain of cells forming a binary wire[6] have been demonstrated. A QCA-based digital logic gate that performs Boolean AND and OR operations was also demonstrated.[7] Both theory and experiments suggest that these cells can achieve high operating frequencies.[8]

A common feature of all QCA implementations reported thus far is that the dots forming the cell were connected to source and drain leads that act as electron reservoirs. This was useful for the initial demonstration of QCA principles as it allowed tracing of single electron motion between dots and leads by monitoring the current through the source and drain. In this paper, we present a different implementation of QCA in which the dots are not connected to source and drain leads. Excluding these leads not only greatly simplifies device design, fabrication, and measurement, but also simplifies the interfacing of QCA arrays. These experiments demonstrate single electron transfer in a system completely galvanically decoupled from the environment.

The major difference between leaded and leadless dot systems is that in leaded dots, electrons can be added or removed from the source and drain leads while in leadless dots, electrons can move only from one dot to another. This basic difference is evident in their charging diagrams, which identify stable charge regimes as a function of gate biases. In a leaded system, the charging diagram can be obtained simply by measuring conductance through the coupled dot system as a function of the two gate biases.[9] In a leadless system, the subject of this paper, charge state of the dots can be determined only by using external electrometers.

We present two different devices to show (a) the externally measured charging diagram of a leadless double-dot system, and (b) QCA operation in a leadless cell. Both devices are realized on an oxidized Si surface using standard Al/AlO_x tunnel junction technology pioneered by Dolan.[10] Aluminum islands and leads are patterned using electron beam lithography with a subsequent shadow evaporation process and an intermediate oxidation step. The islands in QCA measurements act as dots, and in this paper we will use these names interchangeably. The area of the fabricated tunnel junctions is typically $60\times60\,nm^2$.

All measurements were carried out in a dilution refrigerator. The electron temperature of the device is 70 mK.[6] The experiment was performed in a magnetic field of 1 T in order to suppress the superconductivity of aluminum at millikelvin temperatures. Standard ac lock-in techniques were used for all measurements. The typical capacitance of our tunnel junctions, extracted from the Coulomb gap of the electrometers, is approximately 320 aF.[11] Other lithographic and parasitic capacitances are obtained from the Coulomb blockade oscillations of electrometers as a function of various gate biases.

Our first device consists of two small isolated metal islands connected by a tunnel junction forming a double dot [Fig. 1(a)]. No electrons can be added to or removed from the double dot. However, electrons may be transferred from one dot to the other by applying biases to the gate electrodes. Each dot (labeled D_1 and D_2) is also capacitively coupled to an electrometer.[12] Figure 1(b) shows a measured charging diagram of the floating double dot. The grayscale map represents the experimentally observed potential profile of dot

[a]Present address: Islamshah Amlani, Motorola Labs, 2100 East Elliot Road, MD EL508, Tempe, AZ 85284.
[b]Electronic mail: ravi.k.kummamuru.1@nd.edu

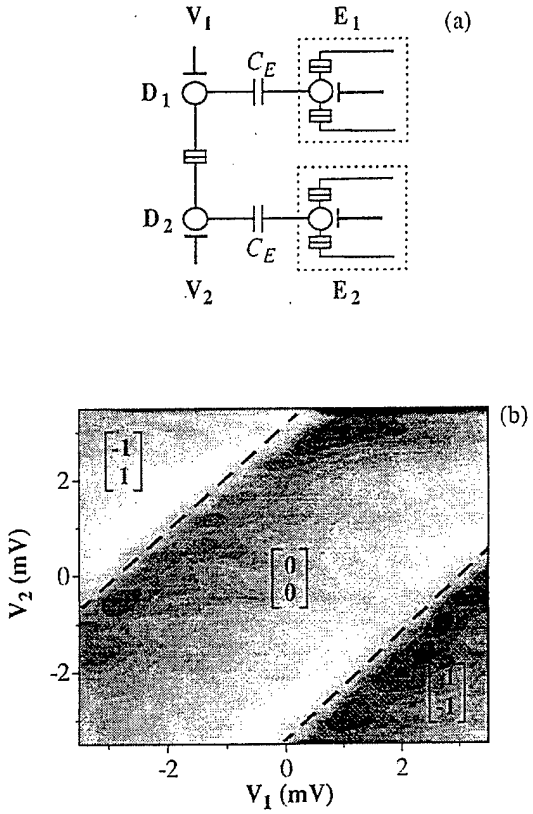

FIG. 1. (a) Schematic diagram of a leadless double-dot system. D_1 and D_2 are the two dots; E_1 and E_2 are the corresponding electrometers. (b) Charging diagram of a leadless double dot. The lighter shades represent higher dot potential. The numbers in the parentheses represent the charge configuration of the double dot.

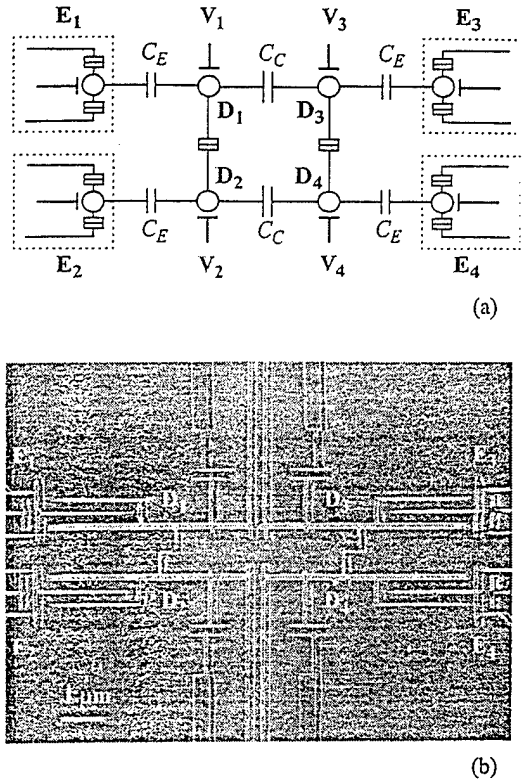

FIG. 2. (a) Schematic diagram of a leadless QCA cell. D_1–D_4 are the four dots, and E_1–E_4 are the corresponding electrometers. (b) SEM micrograph of the leadless QCA cell.

D_1.[13] The potential of the other dot D_2 is similar but has the opposite phase. The dotted lines in Fig. 1(b) define the theoretically calculated borders between different charge states. Since the only possible source of electrons for one of the floating dots is the other dot, the only transitions possible are those when one dot loses an electron and the other acquires it.

We define the state with no applied bias as the neutral state with charge configuration (0,0) where there are no excess electrons on either of the dots (the charge configuration of the double dot represents the number of excess electrons in dots D_1 and D_2, respectively). Let us consider transitions along the $V_1=-V_2$ diagonal, which represents application of a differential bias to the dots D_1 and D_2. As the differential bias is made sufficiently high to overcome Coulomb blockade in the double dot, one electron tunnels from D_2 to D_1 thus changing the charge configuration to $(1,-1)$. If we further raise the bias applied to D_1, one more electron will be lured onto D_1 from D_2, changing the charge configuration to $(2,-2)$ and so on.

Next, we consider our leadless QCA cell [Fig. 2(a)]. The cell consists of two capacitively coupled leadless (floating) double dots. The charge state of each of the four dots is monitored separately by the electrometers E_1–E_4. Figure 2(b) shows a scanning electron microscopy micrograph of a leadless QCA cell. Due to the symmetry of the structure, either of the double dots could be used as input or output, but for clarity, we will refer to the double dot on the left-hand side as the input double dot and the double dot on the right-hand side as the output double dot. In the leadless implementation, QCA operation consists of causing an electron to switch in the input double dot D_1D_2, which induces an electron to switch in the opposite direction in the output double dot D_3D_4. The charge configuration of D_1D_2 changes from $(0,0)\rightarrow(1,-1)$, which induces a change from $(0,0)\rightarrow(-1,1)$ in D_3D_4. This is actuated by applying a differential bias (with opposite polarities $V_1=-V_2$) to the input double dot. Under the influence of the input bias, the potential of D_1 increases (the potential of D_2 decreases), until an electron tunnels from D_2 to D_1 producing an abrupt potential swing in the opposite direction. If the output double dot is biased anywhere on the boundary between two charge states [the dashed line in Fig. 1(a)], the potential perturbation produced by an electron exchange in the input double dot will cause an electron exchange in the opposite direction in the output double dot. This is markedly different from the case of QCA cell with leads, where many electron transitions are allowed and the desirable transition occurs when the bias point is set within a very small range of bias voltages.[5]

The results of the experiment are presented in Fig 3. The solid line in Fig. 3(a) shows the potential variation of D_1 (the change in potential of D_2 is similar but opposite in phase). The signal varies in a sawtooth manner, with the sharp transition corresponding to the transfer of a single electron in the input double dot from D_2 to D_1. This transition causes the transfer of an electron in the opposite direction in the output double dot (from D_3 to D_4,) as indicated by the solid line in Fig. 3(b). Thus, the data shown in Fig. 3 demonstrate QCA operation. The dashed lines in Figs. 3(a) and 3(b) show the

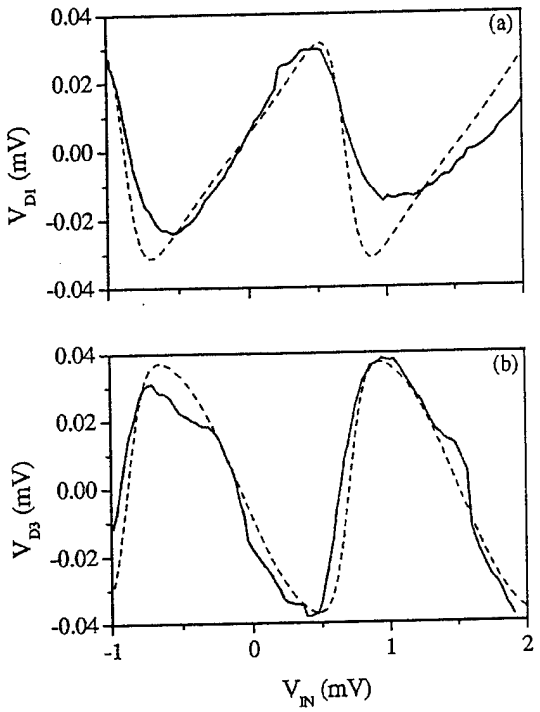

FIG. 3. QCA operation in a leadless cell. Measured (solid line) and calculated (dashed line) potential of (a) dot D_1, (b) dot D_3, with applied differential bias ($V_{in}=V_1=-V_2$).

simulated dot potentials for the two dots for a device temperature of 70 mK.

In Fig. 3 we notice that the potential swing in the output dot D_3 has a larger magnitude than that in the input dot D_1. This effect arises due to thermal smearing. At 0 K the potential of the input dots, resulting from a linearly varying input bias, has a sawtooth shape. However, the potential on the output dots is affected only by the potential on the input dots and hence has a quasisquare wave shape[4] with the same potential swing. At low temperature [$0<kT\ll E_{kink}$ Ref. 14] thermal smearing causes a greater reduction in the potential swing in the input double dot than in the output double dot due to the difference in the shapes of the two wave forms. This results in larger amplitude of potential in the output dots than in the input dots. This effect was not observed in our previous experiments on QCA cells with leads.[4–8] In the previous experiments, dots forming the cell were connected to source and drain leads by tunnel junctions, resulting in larger dot capacitances due to the extra junctions and correspondingly smaller kink energy compared to the current device. Due to the smaller kink energy, the potential swing in the output dots was smaller than that in the input dots. The observation of larger amplitude in the output dot in the current device, in agreement with theory, confirms a more complete polarization change in the output dots than observed in previous experiments.

In conclusion, we have presented externally measured charging diagram of a leadless double dot and QCA operation in a leadless QCA cell. We have shown that the leadless dot design is simpler than the previous devices with leads and it can greatly simplify the fabrication of large QCA arrays. We have also shown that the leadless design results in better QCA performance in terms of output polarization change.

This research was supported in part by DARPA, ONR, and NSF. The authors are grateful to W. Porod and J. Merz for helpful discussions.

[1] C. S. Lent and P. D. Tougaw, Proc. IEEE **85**, 541 (1997).
[2] C. S. Lent, P. D. Tougaw, and W. Porod, Appl. Phys. Lett. **62**, 714 (1993).
[3] C. S. Lent and P. D. Tougaw, J. Appl. Phys. **75**, 4077 (1994).
[4] A. O. Orlov, I. Amlani, G. H. Bernstein, C. S. Lent, and G. L. Snider, Science **277**, 928 (1997).
[5] I. Amlani, A. O. Orlov, G. L. Snider, C. S. Lent, and G. H. Bernstein, Appl. Phys. Lett. **72**, 2179 (1998).
[6] A. O. Orlov, I. Amlani, G. Toth, C. S. Lent, G. H. Bernstein, and G. L. Snider, Appl. Phys. Lett. **74**, 2875 (1999).
[7] I. Amlani, A. O. Orlov, G. Toth, G. H. Bernstein, C. S. Lent, and G. L. Snider, Science **284**, 289 (1999).
[8] A. O. Orlov, I. Amlani, G. Toth, C. S. Lent, G. H. Bernstein, and G. L. Snider, Appl. Phys. Lett. **73**, 2787 (1998).
[9] I. Amlani, A. O. Orlov, G. L. Snider, C. S. Lent, and G. H. Bernstein, Appl. Phys. Lett. **71**, 1730 (1997).
[10] T. A. Fulton and G. J. Dolan, Phys. Rev. Lett. **59**, 109 (1987).
[11] *Single Charge Tunneling*, edited by H. Grabert and M. H. Devoret (Plenum, New York, 1992), Chaps. 1 and 2.
[12] G. L. Snider, A. O. Orlov, I. Amlani, X. Zuo, G. H. Bernstein, C. S. Lent, J. L. Merz, and W. Porod, J. Vac. Sci. Technol. A **17**, 1394 (1999).
[13] The technique we use to compensate for the effect of parasitic cross capacitances in the device also compensates for the monotonic change in potential on the dots. Therefore only the sawtooth pattern associated with the single-electron switching is seen.
[14] E_{kink} is the characteristic kink energy of the device. We define the kink energy as the energy required to change the polarization of a cell from one binary state to the opposite. This energy, which depends on the coupling capacitance C_c and the dot capacitances, must be much greater than the thermal energy in order to observe a complete polarization change.